UiT The Arctic University of Norway

Faculty of Science and Technology

Department of Geosciences

Nature of the continental lithosphere beneath NW Spitsbergen: A petrological and geochemical study mantle-derived peridotite xenoliths

Anniken Wiig Helland-Hansen

Master's thesis in Geology (Geo-3900), December 2024

Abstract

The youngest volcanic event known from Svalbard is represented by the Bockfjorden Volcanic Complex, located northwest on Spitsbergen at the passive continental margin. Mantle-derived xenoliths from Bockfjorden Volcanic Complex provide petrological insight to the mantle conditions beneath Svalbard, the northwestern extremity of the Eurasian lithospheric plate. New methods are available for pressure and temperature estimates of mantle rocks. These methods provide the possibility of revising the constructed lithosphere-asthenosphere boundary for northwestern Svalbard. Earlier studies have revealed evidence for metasomatic events, reflecting the lithospheric evolution and causing heterogeneity within the lithospheric mantle. The discovered pyroxenites are poorly studied and questions regarding their nature and origin remain unanswered. This integrated study is based on a new collection of mantle-derived xenoliths from Bockfjorden Volcanic Complex. Geochemical data is used for new pressure and temperature estimates and investigating the nature of mantle heterogeneity.

A large collection of mantle-derived xenoliths was obtained from all volcanic centers of the Bockfjorden Volcanic Complex during fieldwork in relation to this thesis. The samples have been petrographically investigated revealing the presence of spinel bearing lherzolites and harzburgites with crosscutting spinel bearing olivine websterite. Major and trace element abundances were obtained for Al-in-olivine geothermometry, Ca-in -spinel geobarometry and an additional two-pyroxene geothermometry. The pressure and temperature estimates by this study indicates heat flow conditions of 65 ± 5 mW/m^2 and a petrological lithosphere-asthenosphere boundary at 80 ± 10 km depth. The findings are compared to the existing geophysical lithosphere-asthenosphere boundary which is slightly (20 km) shallower. All studies of the lithosphere-asthenosphere boundary and heat flow condition for northwestern Svalbard reflects a relatively thin lithosphere, comparable to a continental rift tectonic setting.

Whole rock highly siderophile elements systematics, including Re-Os isochron and Re-depletion ages, define Paleoproterozoic to Mesoproterozoic ages for both peridotites and pyroxenites. The websteritic veins are likely formed in relation to the initial melt depletion and separation of the lithospheric mantle from the convecting mantle. There is a difference in Re-depletion ages from the volcanic center of Sverrefjellet (2.2 Ga) to the volcanic centers of Halvdanpiggen and Sigurdfjellet (1.2 Ga). These are situated on either side of the Breibogen Fault Zone which may represent a boundary between two different blocks of lithospheric

mantle. Osmium concentrations reveal that the lithospheric mantle below Svalbard is different than below the Greenlandic craton, Lena Trough and Gakkel Ridge.

Acknowledgements

This thesis marks the end of several years of my geology studies at UiT in Tromsø. This chapter has been wonderful in many ways both within and outside of the department. These years have most definitely expanded my interest and excitement for the geoscience field. I want to express my gratitude to the people who have impacted the completion of this thesis.

First, I would like to thank you Prof. Sebastian Tappe who has been my supervisor through most of this process. Thank you for providing a very interesting project and all the possibilities that followed. Your excellent guidance, excitement and dedication for the project is something I am beyond grateful for.

A large amount of the analytical work was performed in Japan at Tokyo Institute of Technology (now Institute of Science) Department of Earth and Planetary Sciences. I want to thank you Prof. Akira Ishikawa for involving me in your laboratory. The thesis would not be possible without the guidance though the preparations and analysis from you and the other Ishikawa laboratory members. Also, thank you to the GeoInternInternational project for making the internship in Tokyo possible.

I owe a special thank you to Dr. Jasper Berndt-Gerdes, Beate Schmitte and Joachim Krause for your generous support with the analytical work at University of Münster.

Thank you to Alexander Minakov and Prof. Kim Senger for sharing your knowledge and providing an integrated and wider geological insight to the project.

This thesis would not be possible without the fieldwork, and I am grateful towards the Research Council of Norway for the funding through Arctic Field Grant. Also, a large thank you to the Woodfjorden expedition team and the crew of MV Ulla Rinman for the most enjoyable and unforgettable field experience!

Finally, I would like to thank you Prof. Sten-Andreas Grundvåg for taking over the supervision and to Maria Telmon and Prof. Kim Senger for help of completing this thesis.

Table of Contents

1 Introduction

1.1 The continental lithospheric mantle

Understanding Earth's mantle, its heterogeneity and dynamics is important for many aspects of the geosciences, for instance isostasy studies such as recent uplift in Svalbard (Minakov, 2018). In addition, processes in the mantle may be more crucial for natural resource exploration than previously thought. Melting events beneath the deep continental roots are known to be important for the generation and location of diamond bearing kimberlite volcanism. New views on the continental lithospheric mantle suggests that it also plays a significant role in magmatic ore formation (Griffin et al., 2013), where metals may be picked up from the mantle by ascending melts.

The lithosphere is the ridged outer layer of the Earth comprising the crust and uppermost mantle. With increasing depth, the lithospheric mantle becomes more ductile leading to the asthenosphere (*Figure 1*), also known as the convective mantle. This transition is referred to as the lithosphere-asthenosphere boundary (LAB) (Artemieva, 2011; Tappe et al., 2021). Oceanic lithosphere has a thickness of 50-110 km, thinnest at the spreading centers and thickening outwards. The oceanic crust is mafic, dense and not older than 200 Ma because of subduction and recycling of the lithospheric material into the deeper convecting mantle (Cloos, 1993; Kearey et al., 2009). The continental lithosphere, however, can reach thicknesses of 250 km (Aulbach, 2012; Tappe et al., 2021), is more differentiated with a crust consisting of more felsic components making it more buoyant. This part of the lithosphere is not so easily recycled, and rocks of up to 4 Ga are still preserved (Bowring & Williams, 1999; Hawkesworth et al., 2017; Reimink et al., 2016).

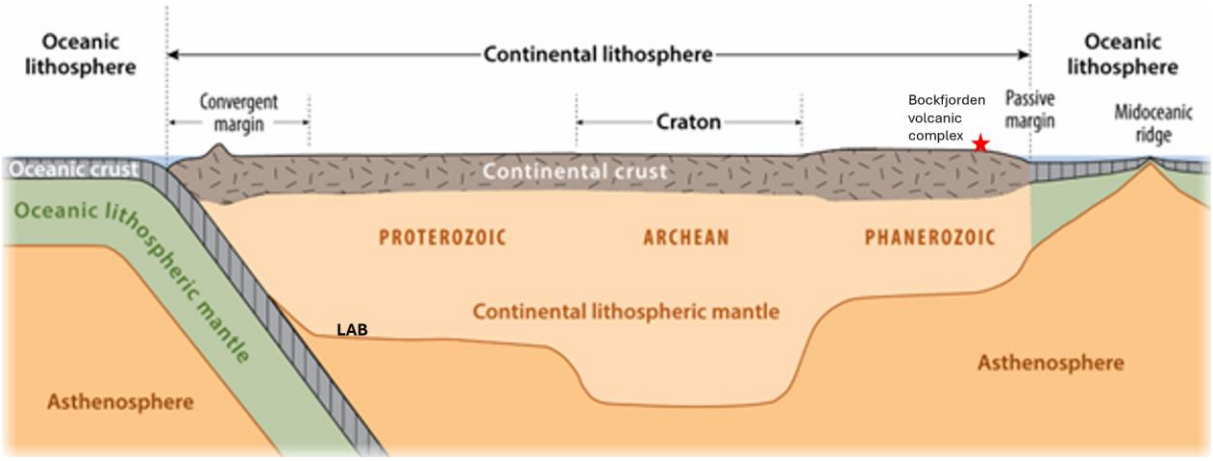

Figure 1: Cartoon of continental and oceanic lithosphere. The study area of this thesis, Bockfjorden volcanic complex, is marked at the edge of the continental lithosphere by the passive margin. Modified after Cawood et al. (2013); Hawkesworth et al. (2017).

The formation of continental lithosphere is the product of differentiation from the convecting mantle. During partial melting, basaltic melt is extracted from the fertile mantle leaving behind a more refractory lithospheric mantle. Partial melting of the mantle occurs either in areas with a high geothermal gradient, such as hotspots related to mantle plumes, or in rift-zones where divergent plate movement causes upwelling of the mantle. In addition, partial melting also occurs in subduction zones where the additional volatiles from the subducting slab shift the solidus and cause partial melting. Another important factor is collision and accretion of smaller continental blocks and arcs during orogenic processes, forming larger and thicker continents (Hawkesworth et al., 2017; McKenzie & Priestley, 2008).

Ancient, stable terranes known as cratons make up the cores of Earth's continents (*Figure 1*). Different definitions of cratons exist, some only include the Archean lithosphere (Hawkesworth et al., 2017) while others include the Proterozoic lithosphere (Lee et al., 2011). An important feature of cratons is the presence of the deepest lithospheric mantle. Cratons make up 60-70% of the continental landmass (Griffin et al., 2004; Griffin et al., 2009; Hawkesworth et al., 2017; Pearson et al., 2021). Archean and Proterozoic mantle are preserved in these large and stable lithospheric roots, though the origin is debated (Griffin et al., 2009; Lee et al., 2011; Pearson & Wittig, 2014; Pearson et al., 2021). This part of the lithosphere was likely produced by the earliest plate tectonics, which probably operated differently from modern plate tectonics (Hawkesworth et al., 2017). Surrounding the cratons are Phanerozoic terranes and orogenic belts (Lee et al., 2011). The continental lithospheric mantle of these regions is generally thinner

and younger compared to the cratonic regions, although some areas bear mantle lithosphere of Proterozoic age (Pearson & Nowell, 2002).

The continental lithospheric mantle is mainly composed of melt-depleted peridotites consisting of olivine, orthopyroxene and clinopyroxene. Additionally, an aluminous phase exists as garnet at high pressures and spinel at lower pressures, with the transition occurring at 1.8-2.0 GPa (~60 km depth) at 1200 °C and 2.6-2.7 GPa (~85 km depth) at 1500 °C (Klemme & O'Neill, 2000). At shallower depths and pressures of <1 GPa (~30 km depth), plagioclase becomes the stable phase (Borghini et al., 2010). The continental lithospheric mantle displays compositional variations, ranging from highly melt-depleted dunites and harzburgites, common for the Archean cratons, to more fertile lherzolites (Griffin et al., 2009; Lee et al., 2011). Such differences affect the buoyancy and rigidity and therefore also the role in plate tectonics, which may explain the survival of ancient cratons.

Compositional differences and heterogeneity are caused by the degree of melt depletion but also refertilization processes such as mantle metasomatism (Griffin et al., 2009; Harte et al., 1975; Menzies, 1983; Pearson & Wittig, 2014) occurring in the continental lithospheric mantle long after its formation. Metasomatism is best described as compositional changes of rocks and minerals due to interaction with fluids or melts (Griffin et al., 2013). Addition of material can happen through both diffusion and pervasive infiltration, producing enriched zones or veins. Such processes in the mantle are likely to modify and weaken the depleted continental lithosphere (Tappe et al., 2007; Wang et al., 2015). Major, minor and trace element compositions can be changed through metasomatism, and there is evidence that clinopyroxene, orthopyroxene, garnet and even olivine may have been added via secondary metasomatic processes to different mantle peridotites (Pearson & Wittig, 2014). Pyroxenites are common metasomatic expressions in the lithospheric mantle and are thought to represent crystallized asthenosphere-derived mafic silicate melts (Irving, 1980; Saunders et al., 2016). Major contributions to continental lithospheric mantle modification may occur during large-scale magmatic events, which, according to Griffin et al. (2005), can change the lithospheric mantle composition several hundred kilometers away from the main eruption center. Because of their prolonged and diverse tectonic and geodynamic evolution, each craton has a distinctly different mantle composition (Artemieva, 2011; Aulbach, 2012).

For direct sampling of the continental lithospheric mantle, there are only two possibilities. One is through orogenic peridotite massifs (Bodinier & Godard, 2003; Menzies & Dupuy, 1991),

which are tectonically exposed parts of the upper mantle. These occur at former plate boundaries and can be hundreds of km^2 in aerial extent. These peridotite massifs are, however, often affected by metamorphic processes during tectonic emplacement and in some cases overprinted by later tectono-magmatic events.

The second possibility for sampling of the continental mantle is as xenoliths brought to the surface through volcanic eruptions. Xenolith is Greek for "foreign rock" because xenoliths represent rock fragments broken off magmatic conduit walls during melt ascent. Therefore, xenoliths represent snapshots of the lithospheric mantle at the time of magma eruption. Xenolithic nodules from Earth's mantle are typically fist sized or smaller but can be up to a meter in diameter. Unfortunately, mantle-derived xenoliths lack field relationships, but they are often the only way of directly investigating the deep lithosphere of stable continents, with some samples originating from the lithosphere-asthenosphere boundary (Tappe et al., 2021). Another drawback of mantle xenolith studies is their restriction to certain tectonic settings where volcanism has occurred, leaving us with a biased record (Artemieva, 2011; Pearson & Nowell, 2002).

Apart from direct sampling, our knowledge about the physical properties of the mantle is based on various geophysical data. Deep seismic refraction surveys (Christensen & Mooney, 1995; Ritzmann & Jokat, 2003; Ritzmann et al., 2004) can, for instance, investigate the geometry and velocity structure of the crust and upper mantle down to 30-40 km depth. Deeper parts of the mantle can be survey using the earthquake sourced method of seismic tomography (Thurber & Ritsema, 2007). Electrical resistivity, temperature and viscosity can be derived from long-period magnetotelluric data (Selway et al., 2020).

1.2 The mantle beneath Svalbard

Svalbard is a Norwegian High Arctic archipelago comprising all islands between 71-81 °N and 15-35 °E. Geologically, Svalbard represents an uplifted portion of the Barents Shelf at the northwestern extremity of the Eurasian tectonic plate. The largest island, Spitsbergen, is situated very close to the active mid-ocean ridge spreading system of the northern most Atlantic and the Arctic Ocean (i.e., Knipovich and Gakkel ridges, respectively).

Petrographical insights to the lithosphere below Svalbard are obtained from xenoliths occurring in the Quaternary basaltic eruptions of the Bockfjorden Volcanic Complex. The first study of the volcanic feature was performed by Hoel & Holtedahl (1911). They described the presence

of volcanic rocks, mantle and lower crustal derived xenoliths from the area of Bockfjorden. Later, the presence of lherzolites, wherlites, pyroxenites and granulites were documented and the first geochemistry and petrology studies preformed (Amundsen et al., 1987; Furnes et al., 1986). Furnes et al. (1986) analyzed major and trace element composition of spinel peridotites showing a variation and enrichment in highly incompatible elements linked to veining or metasomatism by alkali basalt. Amundsen et al. (1987) performed the first thermobarometry on the mantle xenoliths discovering their original pressure and temperature conditions prior to volcanic eruption. From the P-T estimates a geotherm of the area was constructed suggesting a rift associated, thinned lithosphere with lithosphere-asthenosphere boundary at 50 km depth. Already the initial studies of the Bockfjorden Volcanic Complex (Amundsen et al., 1987) proposed that the Quaternary volcanism may be related to the spreading ridge and transform fault zones 150 km further west. This is yet not confirmed, and the origin of the volcanic eruptions remains puzzling.

Both petrological (Amundsen et al., 1987; Vagnes & Amundsen, 1993) and geophysical data (Klitzke et al., 2015; Minakov, 2018; Ritzmann et al., 2007; Selway et al., 2020; Senger et al., 2024) indicate that the Svalbard lithosphere is locally thin (50-80 km) representing a transition from oceanic to stable continental lithosphere. The upper mantle shows low resistivities, similar to young oceanic regions, with partial melt present in the upper asthenosphere (Selway et al., 2020). The lithospheric mantle below Svalbard is about 40-100 °C warmer than the mantle below the central Barents Sea (Minakov, 2018). A mantle xenolith derived geothermal gradient for northwestern Spitsbergen is very high and comparable with rift-tectonic settings (Amundsen et al., 1987) where the heat flow is calculated to be $\sim$130mW/m^2 (Vagnes & Amundsen, 1993).

Pressure and temperature estimates on the mantle xenoliths have been performed (Glebovitskii et al., 2011; Goncharov et al., 2015; Kopylova et al., 1996), and a variation of mineral assemblages have been reported, for instance spinel, garnet and amphibole bearing websterites and clinopyroxenites in addition to spinel lherzolites. Goncharov et al. (2015) highlighted the difference between the peridotites and pyroxenites where peridotites show lower pressure and temperature values (730-1180 °C, 13-27 kbar) than pyroxenites (1100-1310 °C, 22-33 kbar), indicating that the pyroxenites originate from greater depths than the peridotites, 80-100 km and 50-100 km respectively.

The presence of minor amounts of carbonate within the Bockfjorden Volcanic Complex peridotite has drawn considerable attention (Ashikhmin et al., 2018; Ionov, 1998; Ionov et al.,

2002; Ionov et al., 1993; Ionov et al., 1996; Kim et al., 2016). The carbonate is manifested in interstitial fine-grained pockets and veins, which are the products of metasomatism by carbonate-rich alkaline silicate melts enriched in highly incompatible elements. (Kim et al., 2016) performed highly siderophile element systematics on the carbonate pocket-bearing samples and established that this metasomatic event does not overprint the ancient melt-depletion signatures on whole rock scale. Another metasomatic event was revealed by Grégoire et al. (2010) who focused on the composite xenoliths of lherzolite with cross-cutting webseritic veins, both spinel bearing. They found similar major and trace elements compositions for the two rock types and REE-depleted pattern for clinopyroxene which points towards a sub-alkaline (tholeiitic) metasomatic proses.

Isotope studies and dating of the xenoliths have been attempted by several authors (Choi et al., 2010; Griffin et al., 2012; Kim et al., 2016; Nikitina et al., 2022) and the results group into Neoarchean to Paleo- and Mesoproterozoic ages in addition to Ordovician and Silurian. Choi et al. (2010) used Lu-Hf and Re-Os isotopic systems on spinel lherzolites and harzburgites where Paleoproterozoic/Neoarchean ages (T_{RD} ages: 2.22, 2.24 and 2.7 Ga) represent the mantle differentiation. Similar Re-Os ages of whole rock peridotites and sulfide grains (2.7–2.8, 1.2 Ga) are reported from Kim et al. (2016), who also linked PGE abundance systematics to carbonate melt metasomatism. Crust-mantle relationships where studied by dating detrital zircons from the upper crust, granulite xenoliths from the lower crust and sulfides in mantle peridotites (Griffin et al., 2012). The upper crust shows photolith ages of about 1.8 Ga with later reworking (800-1000 Ma and Caledonian) while the lower crust reports as Neoarchean to Paleoproterozoic with some zircons and/or Hf model ages of >3.2 Ga. Griffin et al. (2012) also focused on the differences on either side of the Breibogen Fault Zone where Re-Os data from sulfides in peridotite xenoliths show variation across the fault boundary. West of the fault zone Re depletion model ages group into 3.3 Ga, 2.4-2.6 Ga, 1.6-1.8 Ga and 1.2-1.3 Ga. East of the fault younger ages of 900-1100 Ma and 400-500 Ma are reported. Griffin et al. (2012) suggests that the lithosphere on either side of the fault evolved separately and was brought together by transcurrent displacement during the Caledonian Orogeny. Model ages from the western side have comparable ages to peridotites from the Gakkel Ridge (Liu et al., 2008). Caledonian ages were also reported as the Re-Os (457.0 ± 3.5 Ma) and Rb-Sr (446 ± 78 Ma) isochron ages in addition to U-Pb dating of zircon (458.0 ± 3.5 Ma) from garnet-bearing websterites (Nikitina et al., 2022), though based on limited samples. Nikitina et al. (2022) focused on garnet-spinel

transition concluding on a lithospheric uplift event including partial melting and mineral replacements occurring following the Caledonian Orogeny.

Despite numerous studies on the mantle xenoliths from Bockfjorden Volcanic Complex, there are clear knowledge gaps. Firstly, the study area is remote, and thus rarely visited by researchers. Therefore, the observations of xenolith occurrence and distribution as well as the total sample collection is limited. The reported mineral assemblages and rock types varies, and which mantle rocks are representative for the Bockfjorden Volcanic Complex is little discussed. Secondly, the previous pressure and temperature estimates show variation and the existing petrological lithosphere-asthenosphere boundary at 50 km is uncertain. The estimates are mostly based on garnet pyroxenites with varying mineral assemblages, but new methods are now available for spinel peridotites (D'Souza et al., 2020). In addition, the evolution of the Svalbard mantle shows several stages of formation and metasomatic overprint creating a heterogenous mantle where the timing of metasomatic events is not known.

1.3 Aims and Objectives

This MSc thesis focuses on an integrated analysis of mantle-derived peridotite xenoliths from the Bockfjorden Volcanic Complex to decipher the origin and nature of lithospheric mantle heterogeneity beneath northwestern Spitsbergen. It also attempts to establish a new petrological lithosphere-asthenosphere boundary for the area.

The working hypothesis is that compositional differences in the mantle-derived xenoliths represent metasomatic modifications of the mantle below northwestern Spitsbergen with formation of websteritic veins due to known regional volcanic activity, either the High Arctic Large Igneous Province or Miocene flood basalts. The constructed petrological lithosphere-asthenosphere boundary will be more accurate than previous attempts and reflect similar values as the geophysical lithosphere-asthenosphere boundary.

The following research questions are asked:

1. What is the representative petrography and composition of mantle-derived xenoliths from Bockfjorden Volcanic Complex?
2. At which depth is the lithosphere-asthenosphere boundary beneath northwestern Spitsbergen and from which depths do the xenoliths originate?
3. Did the pyroxene-rich veins form from passing basaltic melts, and can this hidden basaltic magmatic activity be related to any of the known igneous activity at surface?

4. How does the Svalbard lithospheric mantle compare to the North Atlantic and Arctic regions?

The specific objectives are to:

- Document the occurrence of xenoliths in the Bockfjorden Volcanic Complex and describe these from the field to micro-scale.
- Analyze the petrography of and classify the mantle-derived xenoliths obtained from the Bockfjorden Volcanic Complex.
- Establish at which pressures and temperatures (PT) they were in equilibrium using new improved thermobarometry methods. Do the new xenoliths PT data confirm or change the position of the lithosphere-asthenosphere boundary at 1 Ma?
- Compare the petrographical lithosphere-asthenosphere boundary to existing geophysical lithosphere-asthenosphere boundary.
- Apply highly siderophile element systematics to constrain the nature and origin of the mantle heterogeneity e.g. websteritic veins. Can whole rock Re-Os isotopes reveal the timing of mantle evolutional events?

2 The study area

2.1 The tectono-magmatic evolution of Svalbard

The crustal basement of Svalbard is defined as the pre-Devonian metamorphic rocks represented by three major geological domains: the southwestern, northwestern and northeastern basement provinces (Dallmann, 2015; Smelror et al., 2025). These are interpreted to have been juxtaposed during the Caledonian Orogeny (480-400 Ma). The earliest evidence of crustal rocks are zircon grains of Archean age from a monzonite and metasediments in the two northern basement provinces, dated to 2710 Ma (Hellman et al., 2001) and 2500-2800 Ma (Gee & Hellman, 1996), respectively. A more continuous stratigraphic record is preserved from the Proterozoic onwards.

During the Proterozoic, the basement of Svalbard experienced granitic intrusions dated to 1750 Ma (Johansson & Gee, 1999), followed by sedimentary deposition, preserved as granitic gneisses and metasedimentary rocks, including a well-preserved Neoproterozoic to early

Cambrian sedimentary succession (Smelror et al., 2025). Another period of felsic magmatism occurred at 960 Ma, present in the northwestern and northeastern basement provinces. This phase of granitic magmatism is thought to be part of the late stage of the Grenvillian Orogeny (Johansson et al., 1999; Ohta & Larionov, 1998; Pettersson et al., 2009). Subsequently, the lithosphere experienced rifting and basin formation with development of a continental margin continuing into the early Paleozoic.

The Caledonian Orogeny, a major mountain building event occurring from Ordovician to early Devonian times, affected eastern North America, eastern and northern Greenland, and northwestern Europe up to Svalbard. The orogenic event caused continental thickening and high-grade metamorphism. Eclogites and blueschists are present on Svalbard, indicating old subduction zones related to the Caledonian Orogeny (Hirajima et al., 1988). Mildly deformed Ordovician carbonate platform strata occur in NE Svalbard (Smelror et al., 2025), whereas thick Devonian sedimentary strata mark the collapse, extension and erosion of the mountain chain (McClay et al., 1986). From the Devonian through the late Paleozoic and the Mesozoic, Svalbard accumulated a thick sequence of sedimentary rocks deposited in different environments and recording the dynamic interplay between fluctuating eustatic sea level, regional tectonics, climatic forcing and the continuous northward drift of Svalbard and the Eurasian plate (Dallmann, 2015; Olaussen et al., 2025). This period forms most of the typical sedimentary bedrock exposed on Svalbard.

The formation of the northernmost North Atlantic Ocean began during the Cretaceous, associated with regional-scale mantle sourced igneous activity in the High Arctic. The High Arctic Large Igneous Province (Maher, 2001), known also from Arctic Canada (Buchan et al., 2006; Dockman et al., 2018; Ernst & Bleeker, 2010) and Frans Josef Land, forming hundreds of meters thick lava flows, is represented on Svalbard as many mafic sills and dykes collectively grouped as the Diabasodden Suite (Dallmann, 1999). These are mostly dolerites intruded into Permian to Jurassic sedimentary rock units (Senger et al., 2014), with subordinate remnants of lava flows on Kong Karls Land (Olaussen et al., 2018). The magmatic activity also caused regional uplift, tilting the bedrock creating a regional dip towards the south and exposing it for erosion (Maher, 2001).

During the early Cenozoic, Svalbard experienced the Eurekan deformation, a complex compressional regime (Piepjohn et al., 2016). The event caused formation of the West Spitsbergen Fold and Thrust Belt promoting folding, and the development of compressional

and transform faults and thrusts (Bergh et al., 1997; Braathen & Bergh, 1995). Eventually, Svalbard and Greenland separated, opening up the Fram Strait (Engen et al., 2008). The divergent plate boundaries comprises large scale shear zones (Harland 1669) and ultra slow sea floor spreading like Lena Trough (Ehlers & Jokat, 2009) and is continuing to the present-day with Svalbard representing a passive continental margin.

The youngest magmatic rocks on Svalbard are formed by two stages of volcanism manifested mainly in northwestern Spitsbergen. The oldest pulse are Miocene lavas of the Seidfjellet Formation (Dallmann, 1999; Prestvik, 1977) forming up to 400 meters thick sequences of lava flows erupted onto Devonian sediments over an area of 4000 km^2. The eruption age is poorly constrained but apparently at ca. 10 Ma (Cromwell et al., 2013; Prestvik, 1977), a time when Svalbard had been eroded into a large peneplain. These Miocene lavas are interpreted to be flood basalts filling paleo-river-valleys (Prestvik, 1977). Later, the area has been uplifted and today the Miocene lavas form mountaintops at about 1000 m elevation.

The second recent episode of volcanic activity took place during the Quaternary in the time of the last glacial maximum, creating at least three volcanic centers known as the Bockfjorden Volcanic Complex, the focus of this thesis. The northernmost center, the eroded volcano Sverrefjellet, is dated to 1.05±0.07 Ma (Treiman, 2012), or even as young as 100-250 ka (Skjelkvale et al., 1989). Lavas have primitive alkali basaltic compositions, typical for intraplate continental rifting, but the origin of the volcanism remains poorly constrained. Large amounts of mantle-derived xenoliths have been brought up to the surface during these volcanic eruptions, providing insights into the upper mantle beneath northwestern Spitsbergen (Amundsen et al., 1987; Choi et al., 2010; Furnes et al., 1986; Grégoire et al., 2010; Griffin et al., 2012; Ionov et al., 2002).

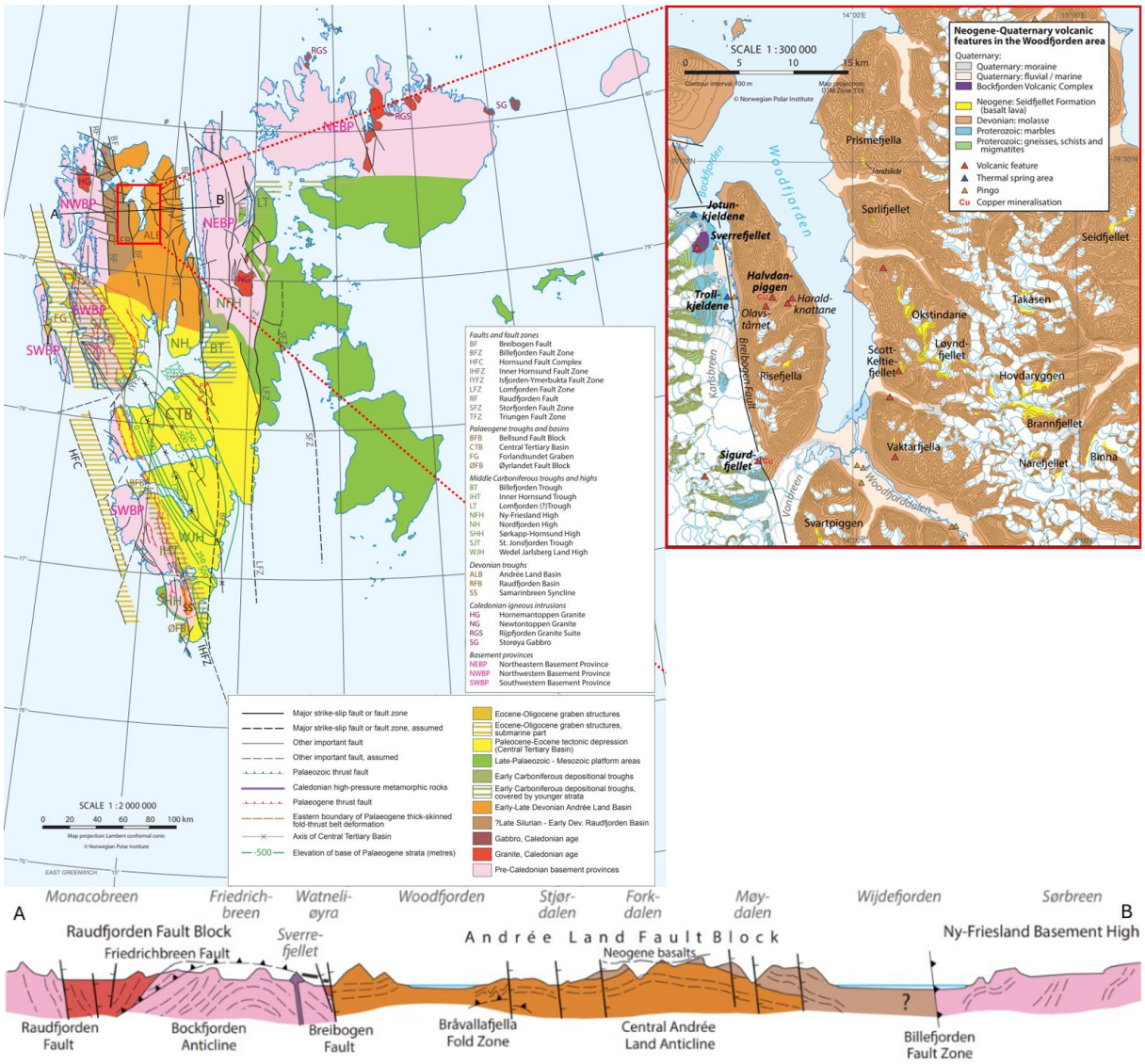

Figure 2: Geological map of Svalbard. The study area is marked by the red square and the cross section (A-B) runs through. The regional map shows the major geological domains highlighting the basement provinces, Phanerozoic sedimentary depositions and structural elements. The Breibogen Fault runs through the study area separating Proterozoic basement and Devonian sedimentary rocks. Bockfjorden Volcanic Complex, comprising Sverrefjellet, Halvdanpiggen and Sigurdfjellet volcanic centers, is situated along the Breibogen Fault. Thermal springs (Jotun- and Trollkjeldene) and Miocene lava flows (Seidfjellet formation) are also present in the study area. Maps are modified after Dallmann (2015).

2.2 Geology of the Bockfjorden-Woodfjorden study area

The mantle-derived peridotite xenoliths investigated in this study were collected in July 2023 from the three main eruption centers of the Bockfjorden Volcanic Complex: Sverrefjellet, Halvdanpiggen and Sigurdfjellet. These are located in northwest Spitsbergen, the largest island of Svalbard, along the north-south trending Breibogen Fault Zone, which separates Proterozoic basement rocks in the west from Devonian sandstone-dominated units in the east (*Figure 2*).

The Proterozoic basement consists of felsic gneisses, migmatites, amphibolites and metasedimentary rocks including marbles, and they were strongly deformed during the

Caledonian Orogeny (Birkenmajer, 1975; Ohta et al., 1989). East of the basement lies a succession of Devonian sedimentary rocks, known as the 'Old Red Sandstone' succession, forming mountains reaching above 1000 m elevation.

The Breibogen Fault Zone (*Figure 2*), part of the Raudfjorden-Breibogen Fault Complex, strikes NNW-SSE showing strike-slip motion with both transtensional and later transpressional movement during the late Silurian to early Devonian. The faulting contributed to the formation of basins where the Devonian molasse-type sediments were deposited. No later reactivation has been recorded, though the fault zone shares similar orientation to other long-lived shear zones in Svalbard, such as the Billefjorden Fault Zone and the Hornsund Fault Complex. These have been reactivated several times with the latest documented activity in the Eocene and early Oligocene (McCann & Dallmann, 1996; Smyrak-Sikora et al., 2024). It is debated whether these long-lived fault zones may be older than Devonian, with large contribution in bringing the different basement provinces together during the Caledonian Orogeny (Gee et al., 1992; Koehl & Allaart, 2021). Griffin et al. (2012) argue that the Breibogen Fault Zone is at least 80 km deep and represents a terrane boundary where the eastern and western parts share the same Archean evolution preserved in the lower crust but show different deformation histories in post-Archean times.

The northernmost volcanic center of the Bockfjorden Volcanic Complex, Sverrefjellet, is an eroded stratovolcano (*Figure 3, panel B*) situated just west of the Breibogen Fault Zone in between Proterozoic marbles *(Figure 2).* The mountain is mostly covered by scree of basaltic composition, but there are several outcrops of dykes and cliffs of pillow lava, lava tubes and sheets. In addition, the upper parts consist of pillars, earlier interpreted as remnants of the volcanic neck (Skjelkvale et al., 1989). The abundance of mantle-derived xenoliths is generally high, though the concentration across a single outcrop can vary from none to areas of about 40% xenoliths, reaching sizes of up to 20 cm in diameter. Although peridotite xenoliths are most common, crustal ones also occur, especially in the pillars.

East of the Breibogen Fault Zone, Halvdanpiggen stands out as a large volcanic pillar within red sandstone mountains. Halvdanpiggen is interpreted as an extensively eroded diatreme (*Figure 3, panel A*) with areas of columnar jointing. Again, the abundance of xenoliths is high, with both mantle peridotites and shallower crustal plus sedimentary xenoliths being present. Several other (smaller) vents occur in the area near Halvdanpiggen, such as Haraldknattene on the opposite side of the valley and Olavstårnet farther up the ridge *(Figure 2).*

The third volcanic center, Sigurdfjellet, is situated directly on the Breibogen Fault Zone (*Figure 2*). It forms an elongated ridge of layered volcanic rocks surrounded by glaciers. In addition to the volcanic centers, the Bockfjorden Volcanic Complex also includes two active thermal springs, Jotun- and Trollkjeldene, which precipitate travertine over several sinter terraces (*Figure 3, panel C*) (Jamtveit et al., 2006). In July 2023, these springs held water temperatures of up to 24 °C (Senger et al., 2024).

Miocene lavas, formally classified as the Seidfjellet Formation (Dallmann 1999), are also present in the study area, mostly east of Woodfjorden (*Figure 2*). The Risefjella outcrops about 7 km south of Halvdanpiggen are the closest to the Bockfjorden Volcanic Complex. Mountaintops, like Lavatoppen (*Figure 3, panel D*), consist of sequences of up to 15 individual basaltic lava flows (Prestvik, 1977).

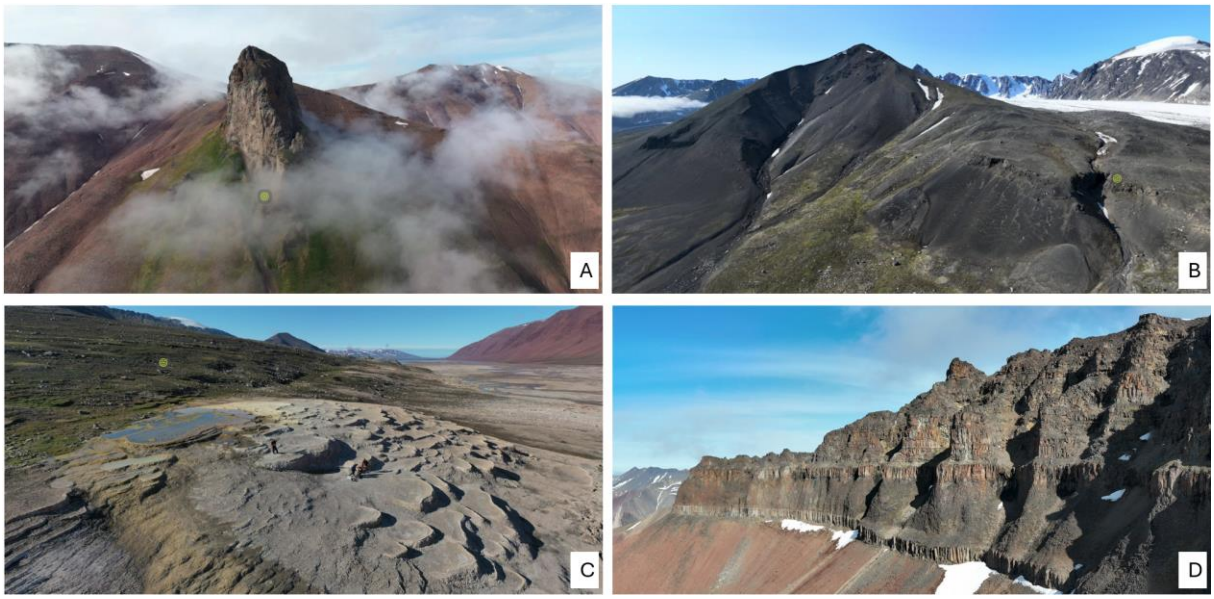

Figure 3: Images of volcanic features in Woodfjorden area. In the center of panel A is Halvdanpiggen, an eroded volcanic neck and one of three volcanic centers of Bockfjorden Volcanic Complex. The pillar is about 100 meters tall. Panel B shows the mountain Sverrefjellet (506 m.a.s.l.), an eroded volcano with outcropping cliff sections but mostly covered in scree. The thermal springs, Trollkjeldene, form travertine terraces shown in panel C. The thermal water holds temperatures up to 24 °C. Panel D shows the uppermost section of the mountain Lavatoppen (1037 m.a.s.l.) east of Woodfjorden, consisting of Miocene lava flows situated on top of Devonian sandstone. Images are screenshots of photospheres from https://vrsvalbard.com/, last accessed 11.12.2024.

3 Methods and data

The methods of this thesis are divers, combining fieldwork, petrographical investigations and different geochemical analysis. An overview is presented in *Table 1*.

Table 1: Summary of applied methods. All methods were performed by the author with professional guidance and assistance (see Acknowledgments).

Method (and text section)	Purpose	Location and time of analysis	Reference
3.1. Fieldwork and xenolith sampling	Field investigation of the study area and sample collection	Bockfjorden and Woodfjorden, Svalbard, July 2023	Senger et al. (2024)
3.2 Sample preparations	Sorting and preparing material for geochemical analysis	Tromsø, October 2023-March 2024	-
3.3 Petrography	Investigating mineral compositions, textures and rock classifications	Tromsø, June 2024	Harte (1977) Streckeisen (1976)
3.4 EPMA	Major element compositions of rock forming minerals.	Münster, Germany, October 2024	-
3.5 LA-ICP-MS	Trace element compositions of rock forming minerals. Al in olivine specifically important.	Münster, Germany, October 2024	-
3.6 Geobarometry and thermometry	Pressure and temperature estimates	Tromsø, November 2024	D'Souza et al. (2020) Coogan et al. (2014) Köhler and Brey (1990) Brey and Köhler (1990)
3.7.2 N-TIMS	Whole rock Os abundance	Tokyo, Japan, May 2024	Fujita et al. (2024)
3.7.3 ICP-MS/MS	Whole rock highly siderophile element abundances	Tokyo, Japan, May 2024	Fujita et al. (2024)

3.1 Fieldwork and xenolith sampling

The samples analyzed for this project were collected during fieldwork in the Woodfjorden and Bockfjorden area, NW Svalbard, in July 2023 as part of a multi-disciplinary geoscientific expedition (Senger et al., 2024). The aims for the expedition were investigations of the Cenozoic geological evolution of the area including Miocene and Quarternary volcanic features. In adition to rock sampling the expedition team collected gas, fluid and travertine from the thermal springs, mapped the Miocene basalts, Sverrefjellet and Halvdanpiggen volcanic centers, acquired magnetotelluric data and drone-based photographs for constructing digital outcrop models, photospheres and thematic virtual field trips.

Figure 4: Pictures from the fieldwork at the Bockfjorden Volcanic Complex. Panels A, B and C are from Sverrefjellet showing the scree slopes of the eroded volcano and cliff sections with outcrops. Panel C shows a very high abundance of mantle xenoliths in basaltic lava (Notebook of 19x12cm for scale). Panels D & E are from Halvdanpiggen showing the volcanic pillar (130m tall) with columnar jointing and xenoliths, the large light colored in Panel E being a crustal xenolith (hammer for scale). Panel F shows the slopes leading down from Sigurdfjellet towards the glacier Vonbreen, where samples were collected from one of the gullies. All photos taken by the author in July 2023.

In total, approximately 200 peridotite mantle xenoliths were collected from the three volcanic centers of the Bockfjorden Volcanic Complex (i.e. Sverrefjellet, Halvdanpiggen, and the slopes beneath Sigurdfjellet). Of the acquired material, 41 xenoliths were selected for detailed petrological investigations as part of this thesis (Figure 5).

Most of the collected samples come from the eroded volcano at Sverrefjellet. Many mantle xenoliths were found lying on the scree slopes that cover the mountain (*Figure 4*, panel A). These were easy to sample, and therefore a large amount was collected, estimated to be 100-150 individual nodules. Samples of this location belong to the northern, eastern and southern slopes of Sverrefjellet. In addition to the peridotite xenoliths, crustal xenoliths, a few amphibole megacrysts and basaltic lava were sampled.

At Halvdanpiggen, ten mantle-derived nodules were sampled from the base of the pilar (*Figure 4*, panel D and E), while about 50 additional mantle xenoliths were collected from the delta leading out of Halvdandalen. These xenoliths are most likely derived from Halvdanpiggen or Haraldknattene, both situated within Halvdandalen.

Sigurdfjellet is the most remote of the Quaternary volcanic centers. Due to weather conditions and difficult access conditions without helicopter support, the actual volcanic outcrops were not visited in 2023, but erosional material was collected from a gully leading from the mountain towards Vonbreen (*Figure 4*, panel F). The 10 peridotite xenoliths found at this site may have been transported with the nearby glacier from elsewhere, but they were situated all in proximity to each other and no other volcanic material was present along this moraine. Also, the Quaternary volcanic centers are the only rocks known to contain mantle-derived xenoliths and therefore samples collected in the gully below Sigurdfjellet most likely originated from Sigurdfjellet.

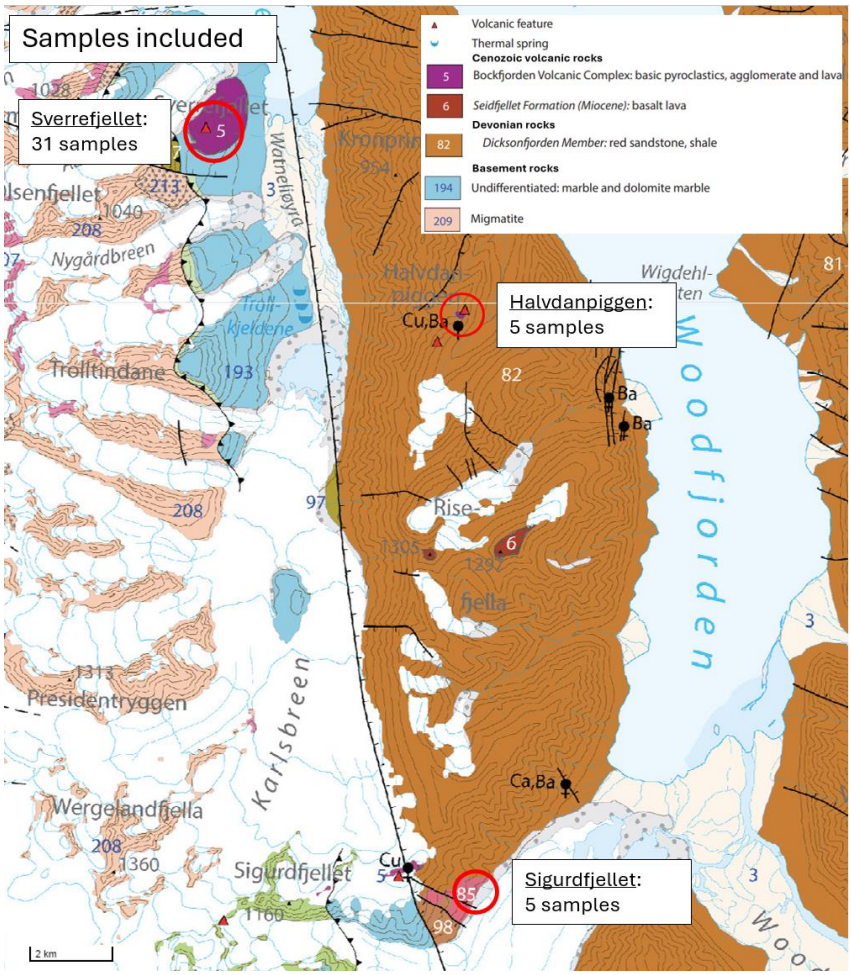

Figure 5: Geological map showing sample locations and the number of samples chosen for further analysis. The samples included from Sverrefjellet and Halvdanpiggen were sampled in situ while Sigurdfjellet was sampled from a gully below the outcrops. Map from https://geokart.npolar.no/geologi/GeoSvalbard/ last accessed 13.12.2024.

3.2 Sample preparation

The roughly 200 mantle peridotite xenoliths collected during the fieldwork in July 2023 were transported to Tromsø (UiT The Arctic University of Norway, Department of Geosciences) by boat in the same expedition vessel 'Ulla Rinman', which arrived in Tromsø by end-September 2023. At UiT, the samples were sorted, choosing only those of high quality for further analysis, but also ensuring to cover the observed textural and mineralogical range. Texture variations were described, ranging from coarse granular, regular peridotite to porphyroclastic and composite, which show more eye-catching green pyroxenes. Some of the composite xenoliths had a laminated structure with pyroxene-rich veins. This texture was identified more easily in the larger nodules. After sorting and screening, the collection consisted of 31 samples from Sverrefjellet, 7 of those showing composite laminated structures, and 5 samples from Halvdanpiggen and Sigurdfjellet each (*Table 2*).

The selected samples were then cut with a diamond coated saw, with 1 or 2 blocks cut out from each xenolith, which were sent to the University of Münster, Germany, for polished thin section preparation. Basaltic host material was coating and infiltrating many of the peridotite xenoliths, and this material was cut away before the xenoliths were carefully crushed with a hammer covered with plastic to avoid metal contamination. From the crushed rocks, mineral separates of spinel and olivine were handpicked under a binocular microscope. A portion of each crushed rock sample in addition to mineral separates were milled to fine powder using an agate hand mill.

Table 2: Overview of the samples selected for the different analysis, their sample locality, texture and classification. Green "y" means analyzed and red "n" is for left out. The coordinates for the sampling localities are as following: Sverrefjellet 79.43 °N 13.3 °E, Halvdanpiggen 79.38 °N 13.6 °E and Sigurdfjellet 79.25 °N 13.6 °E.

Sample ID	Locality	Texture	Classification	Thinsection	Whole rock N-TIMS	Whole rock ICP-MS	EPMA	LA-ICP-MS
BVC23X-01	Sverrefjellet	Coarse granular	Lherzolite	y	y	y	n	n
BVC23X-02	Sverrefjellet	Coarse granular	Lherzolite	y	y	y	y	y
BVC23X-03	Sverrefjellet	Porphyroclastic	Harzburgite	y	y	y	n	n
BVC23X-04	Sverrefjellet	Coarse granular	Lherzolite	y	y	y	n	n
BVC23X-05	Sverrefjellet	Coarse granular	Lherzolite	y	y	y	y	y
BVC23X-06	Sverrefjellet	Porphyroclastic	Lherzolite	y	y	y	y	y
BVC23X-07	Sverrefjellet	Coarse granular	Lherzolite	y	y	y	n	n
BVC23X-08	Sverrefjellet	Coarse granular	Lherzolite	y	y	y	n	n
BVC23X-09	Sverrefjellet	Porphyroclastic	Harzburgite	y	y	y	y	y
BVC23X-10	Sverrefjellet	Porphyroclastic	Lherzolite	y	y	y	n	n
BVC23X-11	Sverrefjellet	Coarse granular	Harzburgite	y	y	y	n	n
BVC23X-12	Sverrefjellet	Composite veined	Harzburgite	y	y	y	y	y
BVC23X-13	Sverrefjellet	Composite veined	Harzburgite	y	y	y	y	y
BVC23X-14	Sverrefjellet	Coarse granular	Harzburgite	y	y	y	y	y
BVC23X-15	Sverrefjellet	Coarse granular	Lherzolite	y	y	y	y	y
BVC23X-17	Sverrefjellet	Porpyroclastic	Lherzolite	y	y	y	n	n
BVC23X-19	Sverrefjellet	Porpyroclastic	Lherzolite	y	y	y	y	y
BVC23X-20	Sverrefjellet	Coarse granular	Lherzolite	y	y	y	n	n
BVC23X-21	Sverrefjellet	Porphyroclastic	Lherzolite	y	y	y	n	n
BVC23X-22	Sverrefjellet	Coarse granular	Harzburgite	y	y	y	n	n
BVC23X-23	Sverrefjellet	Granular	Lherzolite	y	y	y	y	y
BVC23X-24	Sverrefjellet	Porphyroclastic	Harzburgite	y	y	y	n	n
BVC23X-25	Sverrefjellet	Coarse granular	Harzburgite	y	n	n	n	n
BVC23X-26	Sverrefjellet	Coarse granular	Harzburgite	y	n	n	n	n
BVC23X-27	Sverrefjellet	Coarse granular	Harzburgite	y	n	n	n	n
BVC23X-28	Sverrefjellet	Coarse granular	Lherzolite	y	n	n	n	n
BVC23X-29	Sverrefjellet	Coarse granular	Lherzolite	y	n	n	n	n
BVC23X-30	Sverrefjellet	Coarse granular	Lherzolite	y	n	n	n	n
BVC23X-31	Halvdannpiggen	Coarse granular	Harzburgite	y	y	y	n	n
BVC23X-32	Halvdannpiggen	Porphyroclastic	Harzburgite	y	y	y	y	y
BVC23X-33	Halvdannpiggen	Coarse granular	Lherzolite	y	y	y	n	n
BVC23X-34	Halvdannpiggen	Coarse granular	Lherzolite	y	y	y	y	y
BVC23X-35	Halvdannpiggen	Coarse granular	Lherzolite	y	y	y	n	n
BVC23X-37	Sigurdfjellet			y	y	y	y	y
BVC23X-38	Sigurdfjellet	Coarse granular	Lherzolite	y	y	y	y	y
BVC23X-39	Sigurdfjellet	Coarse granular	Lherzolite	y	y	y	y	y
BVC23X-40	Sigurdfjellet	Porphyroclastic	Lherzolite	y	y	y	n	n
BVC23X-41	Sigurdfjellet	Coarse granular	Lherzolite	y	y	y	n	n
BVC23X-43	Sverrefjellet	Composite laminated	Lherzolite	y	y	y	y	y
BVC23X-44	Sverrefjellet	Composite laminated	Harzburgite	y	y	y	y	y
BVC23X-45	Sverrefjellet	Composite laminated	Harzburgite	y	y	y	y	y

3.3 Petrography

Mineralogy and petrographic properties of all samples were investigated through polished thin sections of 50-60 µm thickness, using a Leica DM 4500 P microscope, and images were taken with a Leica Microsystems camera type DMC4500 optimized with the software Leica Application suite X version 3.0.13.22215. Where the microscope was not sufficient to determine the mineralogy (e.g., spinel vs. garnet), a Hitachi HM3030 tabletop scanning electron microscope (SEM) was used for quality control. These back-scattered electron (BSE) images were carried out without using carbon coating. All thin sections were imaged by an Epson Perfection V750 PRO scanner and a selection of 5 composite veined samples were in addition scanned by Plustek Optic film 8200i to obtain higher resolution images. All petrographical analyses were performed at UiT.

Terminology for rock textures are based on Harte (1977) and modal mineral assemblages and abundances were estimated from visual inspections of the thin sections, and rock type classification followed the recommended IUGS nomenclature (Streckeisen, 1976).

3.4 Electron probe microanalysis – Major elements

Samples for electron probe microanalysis (EPMA) were chosen based on variation in sample texture and classification in addition to highly siderophile elements abundances. Neighboring olivine, orthopyroxene, clinopyroxene and spinel were selected from equilibrated areas with curvilinear grain boundaries that meet at 120 degrees angles. For composite samples, the EPMA analysis were performed for minerals inside the pyroxenitic vein and outside in the regular peridotite host.

Major elements concentrations of 18 carbon coated samples were measured by a JEOL JXA-8530F field emission electron probe microanalyzer (*Figure 8*, panel B) at University of Münster, Germany. For analysis, the acceleration voltage was set to 15kV and the beam current to 60nA, while BSE images and the calibration was done with beam current of 14nA. For reference material the natural olivine standard MongOl in addition to Ast-Cr-Diopside were measured before and after each run (each run consisting of three rock samples analysis). Elements were quantitatively analyzed with Na, Mg, Si and Fe measured with 5 seconds counting time, Ti, Mn, Cr, Co, Ni, P for 15 seconds while Al and Ca 25 seconds counting time. Halfway through the analysis one out of five measurement channels broke resulting in moving the Na and Ca measurements to another channel. This change in method is marked in the data *Table 4*.

Figure 6 shows the variation in SiO_2 measured values for the MongOl standard in relation to reported values from Batanova et al. (2019). Measurements are mostly accurate and within the reported margins (grey field on the diagram), though there is a tendency to plot among the higher values for the olivine standard. Datapoints from method 1 are also more precise than from method two. Therefor the data was divided into two methods when corrected against MongOl standard for SiO_2, MgO and FeO, shifting the values slightly lower.

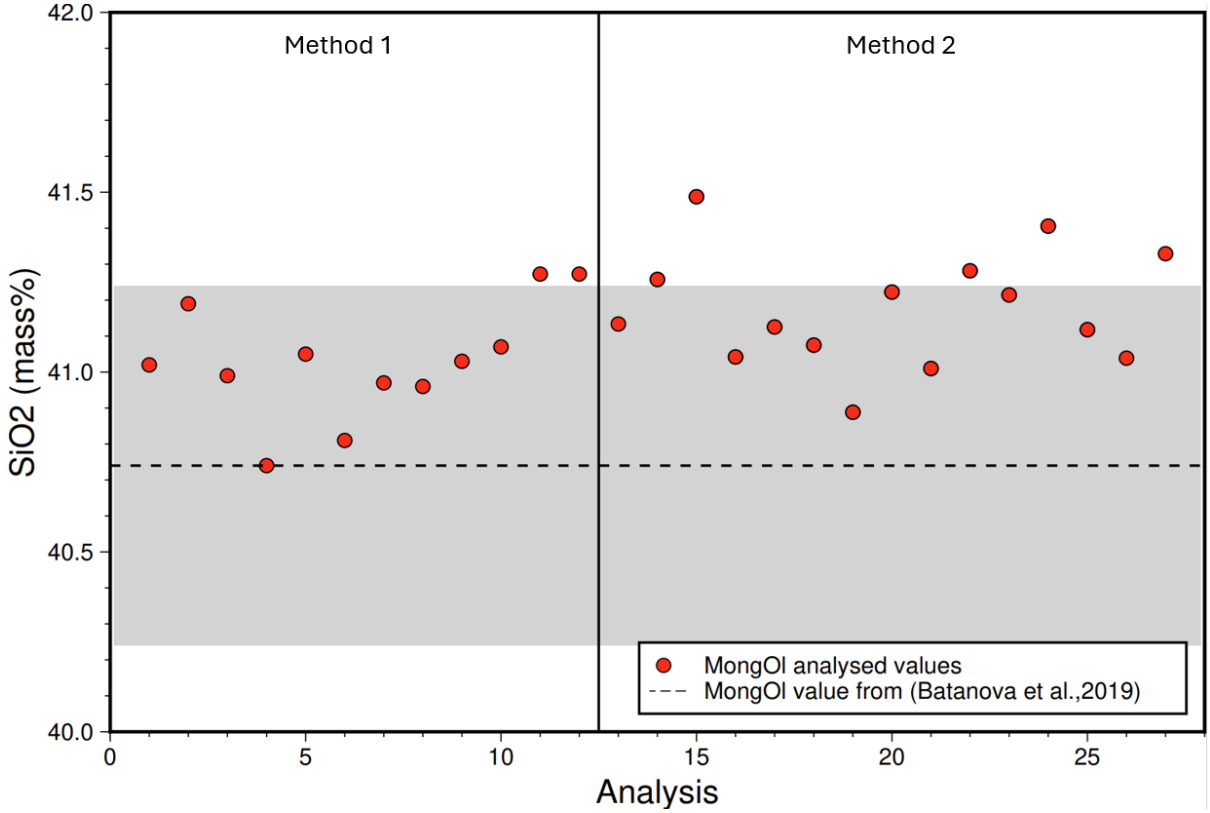

Figure 6: Silica content of olivine standard through EPMA analysis. MongOl standard was measured before and after each run and variation in summed up in this diagram compared to MongOl recommended value of 40.74 ± 0.5 mass% (2 standard deviation) (Batanova et al., 2019) marked as the dashed line ± the grey field. Due to breakdown of machine parts during analysis, the data is divided into method 1 and 2, where method 2 gave a larger spread in measurements of the standard material. Measured olivine from xenoliths samples were corrected against the MongOl standard before further calculations.

3.5 LA- ICP-MS – Trace elements

Trace element compositions of olivine and pyroxene from 18 samples were measured by laser ablation inductively coupled plasma mass spectrometer (LA-ICP-MS) on polished thin sections at the University of Münster, Germany. Spot ablation was performed by IRIDIA from Teledyne Photon Machines with a dimension of 80µm, 5Hz repetition rate and applied energy of 4J. The ablation took place in a mix of He and Ar gas and the sampled material was carried to the mass spectrometer ELEMENT XR from Thermo Fisher Scientific (*Figure 8*, panel A). The analysis

consisted of 20 second background count, 40 second signal and 20 second washout time. For LA-ICP-MS analyses, the samples were not separated into vein and host peridotite due to difficulties in distinguishing the different fields when setting the points for laser ablation.

The reference material used was the synthetic silicate glass NIST-612, the natural olivine standard MongOl in addition to glasses form natural basalts; BIR-1G, BHVO-2G and BCR-2G. A sequence of three NIST-612 and MongOl plus one of each basalts (BIR-1G was only included in the first sequence prior to the samples) was measured before the unknown samples, repeated for every 24th measurement and ending the analysis in reversed order.

Prior to analysis, the instruments were tuned by continuous line ablation of the synthetic NIST-612 glass. The placement of ablation spots was carefully operated avoiding any cracks and sticking to the middle of the grain, choosing pure olivine and pyroxene avoiding contamination of groundmass material. The distinction between minerals in the veins and host peridotite was difficult to perform, therefore this difference is not done for the LA-ICP-MS data. The following isotopic masses were measured: ^{7}Li, ^{9}Be, ^{11}B, ^{23}Na, ^{26}Mg, ^{27}Al, ^{29}Si, ^{43}Ca, ^{45}Sc, ^{47}Ti, ^{49}Ti, ^{51}V, ^{53}Cr, ^{55}Mn, ^{57}Fe, ^{59}Co, ^{60}Ni, ^{65}Cu, ^{66}Zn, ^{69}Ga, ^{85}Rb, ^{88}Sr, ^{89}Y, ^{90}Zr, ^{93}Nb, ^{95}Mo, ^{118}Sn, ^{133}Cs, ^{137}Ba, ^{139}La, ^{140}Ce, ^{141}Pr, ^{146}Nd, ^{147}Sm, ^{151}Eu, ^{157}Gd, ^{159}Tb, ^{163}Dy, ^{165}Ho, ^{166}Er, ^{169}Tm, ^{172}Yb, ^{175}Lu, ^{178}Hf, ^{181}Ta, ^{182}W, ^{208}Pb, ^{232}Th, ^{238}U.

The software GLITTER (http://www.glitter-gemoc.com/, last accessed 12.11.2024) was used for calculations of element concentrations including raw data import, signal selection, background subtraction, corrections of instrumental drift and calibration against the synthetic glass NIST-612. The SiO2 of the reference material content for internal standardization were taken from the website GeoRem (Jochum et al., 2005) and based on the EPMA data for the peridotite samples using the values 50.5 for olivine and 53.5 for pyroxenes.

In the same way as for the EPMA analysis, the olivine samples were corrected against the MongOl standard, following the different sessions of analysis (*Figure 7*).

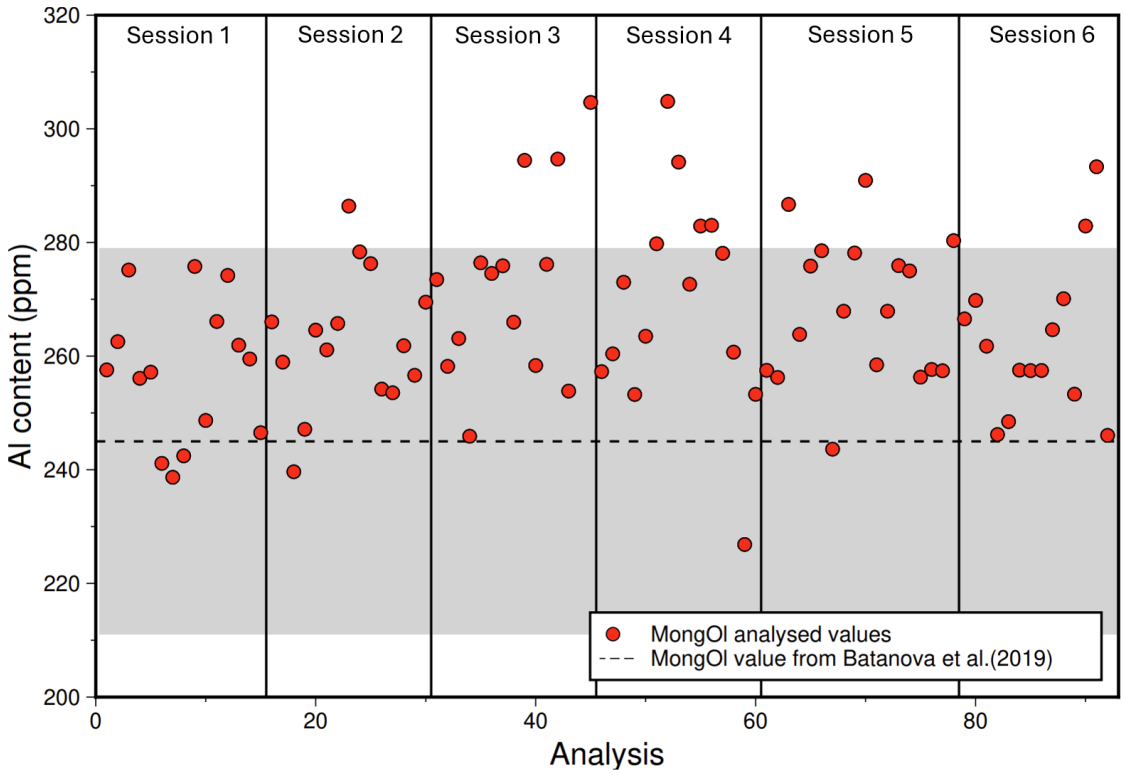

Figure 7: Aluminum content of olivine standard through LA-ICP-MS analysis. MongOl standard was measured before and after every run of unknown samples as well as repeated for every 24th measurement. The variation of MongOl measurements is summed up in this diagram and compared to MongOl recommended value of 245 ± 34 mass% (2 standard deviation) (Batanova et al., 2019), marked as the dashed line ± the grey field. The analysis consisted of six sessions with three samples for each session. An average of MongOl value was calculated for each session and used for correcting against the standard material.

Figure 8: Instruments used for major and trace element compositions at the University of Münster, October 2024. Panel A is the mass spectrometer of the LA-ICP-MS used for trace elements and panel B is the electron probe microanalyzer used for major element analysis. Photos taken by the author.

3.6 Geobarometry and thermometry

Two thermometers paired with one barometer following D'Souza et al. (2020) were calculated based on the element abundances from EPMA and LA-ICP-MS.

3.6.1 Al-in-olivine thermometer

The Al-in-olivine thermometer (Coogan et al., 2014) is based on the Al content in olivine related to spinel in addition to the Cr-number for spinel, using equation 1:

$$T_{Alol} = \frac{10000}{0.575+0.884*Cr\#-0.897*\ln(k_d)} \qquad \text{(equation 1a)}$$

Where

$$k_d = \frac{{Al_2O_3}^{ol}}{{Al_2O_3}^{spl}} \qquad \text{(equation 1b)}$$

Calculated temperatures have an error of ± 25 °C.

Temperatures were calculated twice, with Al_2O_3 content in olivine measured from both EPMA and LA-ICP-MS. When comparing the resulting temperatures from the two methods they give approximately the same values (plotting close to the 1:1 line on *Figure 9* and lie within the calculation error. The largest differences occur for some of the lower temperatures. Because the LA-ICP-MS is a more precise measurement, the following calculations were performed using the Al content in olivine from the LA-ICP-MS analysis.

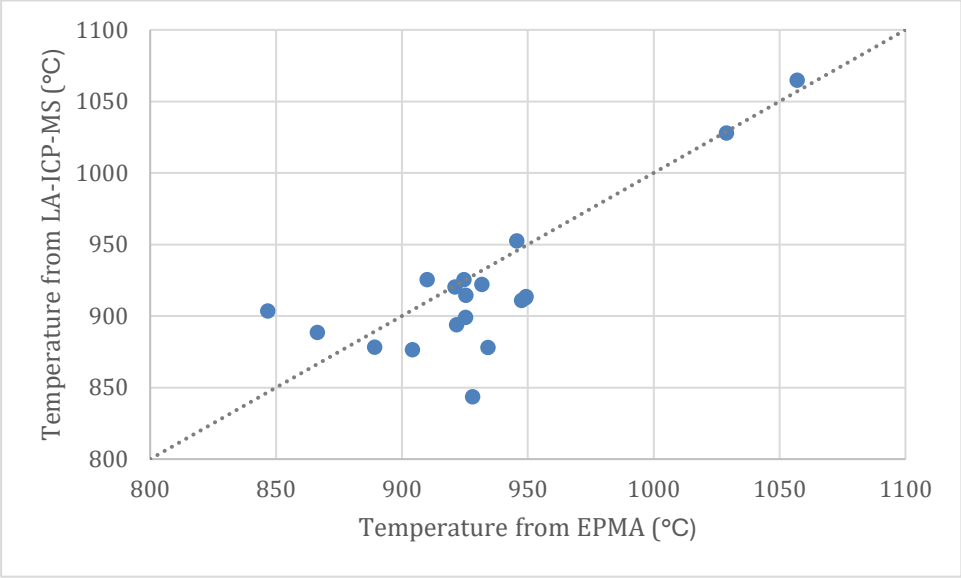

Figure 9: Comparison of temperature calculated by EPMA and LA-ICP-MS. The graph compares temperatures from the Al-in-olivine thermometer using Al_2O_3 content from EPMA and LA-ICP-MS. The dashed line is the 1:1 line.

3.6.2 Ca-in-olivine barometer

For the Ca-in-olivine barometer (Köhler & Brey, 1990) the pressure (P_{KB}) is calculated based on the Ca content in olivine and clinopyroxene as well as the already estimted temperature, folowing equation 2:

$$P_{KB} = (-T * \ln D_{Ca} - 5792 - 1.25 * T)/42.5 \qquad \text{(equaion 2a)}$$

where

$$D_{Ca} = Ca^{ol}/Ca^{cpx} \qquad \text{(equation 2b)}$$

Ca^{ol} and Ca^{cpx} are the calculated atomic proportions of Ca in structural formulae of olivine and clinopyroxene based on 4 and 6 oxygens, respectively. The temperature from Al-in-olivine thermometer was applied and the barometer has an error of ±1.7 kbar. The same equation was applied for all samples because all temperatures are below1100 °C. Pressures were converted to depth with the asumption that 1GPa lithostatic pressure ≈ 33km depth (Cammarano, 2013; Dziewonski & Anderson, 1981).

3.6.3 Two-pyroxene thermometer

An additional thermometer, the two-pyroxene thermometer from Brey and Köhler (1990) was also calculated. Temperatures are based on Ca, Na, Fe and Mg contents in coexisting clino- and orthopyroxenes and includes a predefined pressure as following:

$$T_{BKN} = \frac{23664+(24.9+126.3X_{Fe}^{cpx})P}{13.38+(lnK_D^*)^2+11.59X_{Fe}^{opx}} \qquad \text{(equation 3a)}$$

Where:

$$X_{Fe} = \frac{Fe}{Fe+Mg} \qquad \text{(equation 3b)}$$

$$K_D^* = \frac{(1-Ca^*)^{cpx}}{(1-Ca^*)^{opx}} \qquad \text{(equation 3c)}$$

$$Ca^* = \frac{Ca}{1-Na} \qquad \text{(equation 3d)}$$

Ca, Na, Fe and Mg contents where calculated stoichiometrically based on 6 oxygens and the pressures where given by the Ca-in-olivine barometer. Calculated temperatures have an error of ±15 °C.

Comparing the two thermometers (*Figure 10*) they tend to almost follow eachother (plotting close to the 1:1 line), where warm samples from one method also tuns out warm with the second method. Though, T_{BKN} generally gives warmer temperatures than T_{AlOl}. One sample differs from the trend where T_{AlOl} gives a higher temperature than T_{BKN}.

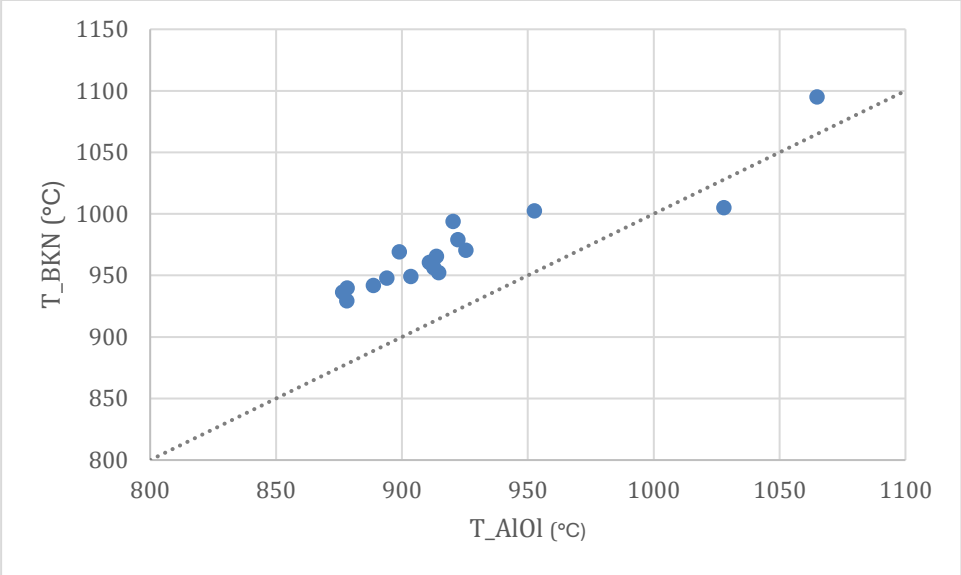

Figure 10: The graph compares given temperatures from the two independent thermometers. The dashed line is the 1:1 line and the samples tend to follow this, though slightly shifted towards T_{BKN}.

3.7 Highly siderophile element abundances

The highly siderophile element abundances of osmium (Os), iridium (Ir), ruthenium (Ru), platinum (Pt), palladium (Pd) and rhenium (Re) were analyzed at the Department of Earth and Planetary Sciences, Tokyo Institute of Technology, Japan. Whole rock powders of 35 samples were brought to the institute for chemistry preparations and mass spectrometer analysis by Negative thermal ionization mass spectrometry (N-TIMS) and Inductively coupled plasma – Tandem mass spectrometry (ICP-MS/MS).

3.7.1 Chemistry preparation

Sample preparations were performed using quartz tube digestion, following Fujita et al. (2024) and illustrated in the flowchart of *Figure 11*. 0.5 g whole rock powder from 35 samples (not including the 5 samples from Sigurdfjellet) was placed into the quartz-glass tube (*Figure 12*, panel D) in addition to two reference materials. Aferwards,1ml 9M HCl was added together with spike solutions for ^{99}Ru, ^{105}Pd, ^{185}Re, ^{190}Os, ^{191}Ir and ^{196}Pt. Spike solutions for ^{34}S, ^{77}Se, ^{126}Te, ^{73}Ge, ^{119}Sn and ^{121}Sb were also added but quantification of these elements was not performed. After adding 3 ml of purged HNO_3, precleaned by H_2O_2, each tube was cooled down in dry

ice, sealed with an oxygen-propane torch, and then placed in a steel jacket for heating in an oven at 240 °C for 72h. After digestion, the sample solution and residual solids in the quartz-glass tube were transferred to Teflon vails, rinsed out of the quartz tubes by 2ml Milli-Q water (resistivity of 18,2 MΩ).

Os was extracted by 2ml CCL_4 and separated from the rest of the sample. 0.750ml HBr was then added, extracting the Os, and CCL_4 removed from the solution. After heating up and evaporating most of the HBr, microdistillation was performed for further reducing the size and purify the Os solution. The sample was then diluted with 10 µl CrO_2 in H_2SO_4, and during heating, close space evaporation trapped Os in 20 µl 9M HBr solution. The sample in HBr was then loaded onto a filament of degassed platinum wire together with NaOH-$Ba(OH)_2$ activator, ready for N-TIMS analysis.

The rest of the sample solution, containing the other highly siderophile elements, was added 1ml milli-Q water, mixed and centrifuged before the liquid went through further purification steps including column chemistry with a resin filters (*Figure 12*, panel C); primarily for anion exchange using resin AG 1-X8 (Muromachi Chemicals), solvent extraction, and secondly for cation exchange using AG 50W-X8 (BioRad). For anion exchange the columns and resin were cleaned by 13.5 M HNO_3 and 6 M HCl before conditioned by 0.5 M HCl. The samples were filtered through the resin, cleaned by 1 M HCl-HF and 0.8 M HNO_3, collected and stored for potential future analysis. At the end of the process, another 10 ml 13.5 M HNO_3 was added to the column and the samples containing highly siderophile elements were collected. Samples dried up before dissolved in 0.75 ml 0.5 M HCl. 0.75ml $CHCl_3$ with N-Benzoyl-N-phenylhydroxylamine (BPHA) was used for solvent extraction before the final preparation step of cation exchange. The new resin was cleaned by 6 M HCl and conditioned by 0.5 M HCL. After BPHA solvent extraction, the sample solution was loaded into the column with 0.75 ml 0.5 M HCl, recovered and ready for analysis by ICP-MS/MS.

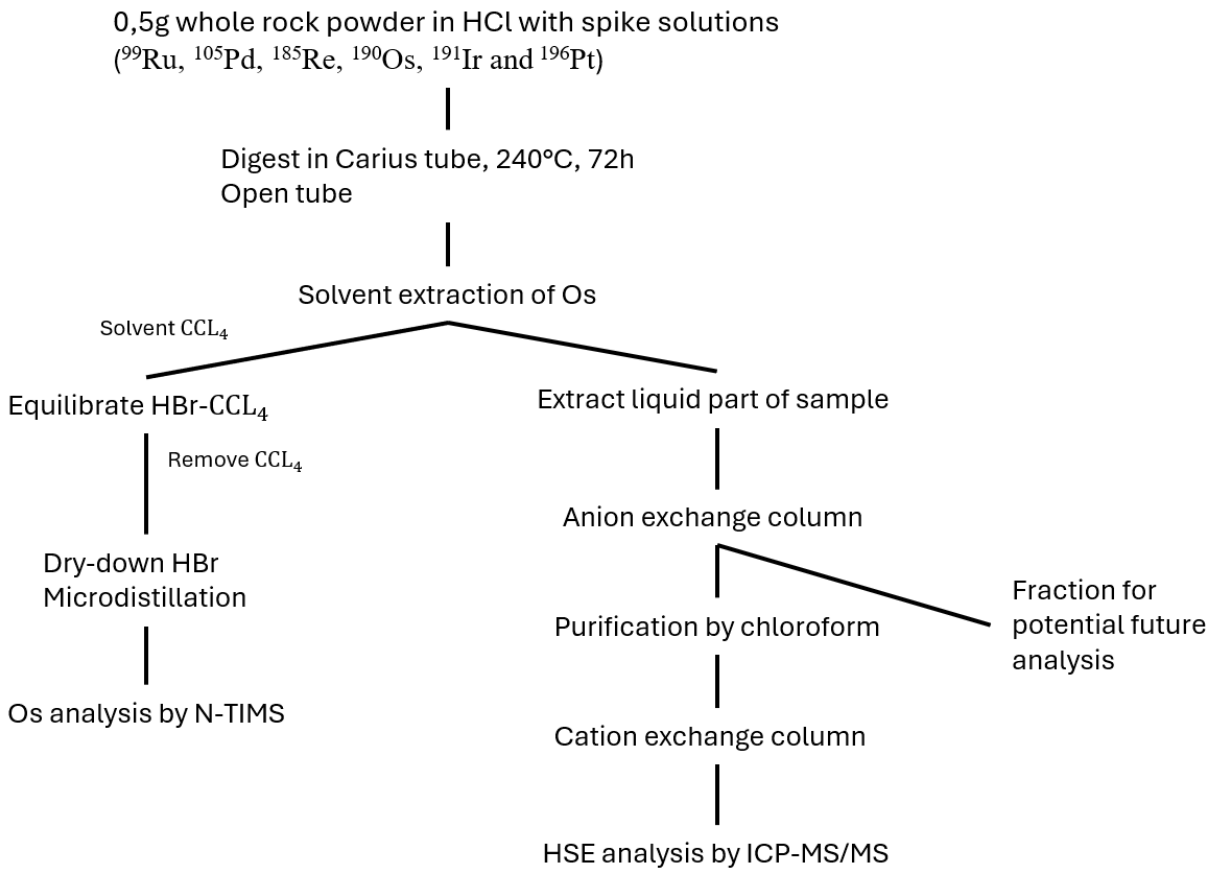

Figure 11: Flowchart showing the chemistry preparation steps prior analysis, modified after Fujita et al. (2024).

3.7.2 N-TIMS

Os isotope abundance was measured as OsO^{-3} ions by N-TIMS using a Triton Plus from Thermo Fisher Scientific (*Figure 12*, panel B). Seven masses of OsO^{-3} (m/e = 233, 234, 235, 236, 237, 238 and 240) were measured both in static mode using Faraday cup (FC) collectors and in peak jumping mode using a secondary electron multiplier (SEM) for all samples except blanks (only SEM). Raw data were corrected off-line for oxygen isotopic interferences (assumed to be $^{17}O/^{16}O$ = 0.0003708 and $^{18}O/^{16}O$ = 0.0020450; (Nier, 1937)), Os mass fractionation (assuming the exponential law with $^{192}Os/^{188}Os$ = 3.08271; (Luck & Allègre, 1983)), and spike unmixing. Os abundance was quantified by isotope dilution (ID) with $^{190}Os/^{188}Os$. Interferences from Re-oxide ions were not corrected because the monitored mass 233 of $^{185}ReO^{3-}$ has a negligible low signal, resulting in its effect on the $^{187}Os/^{188}Os$ ratio being less than 550 ppm. FC and SEM data for the same samples provide consistent values for Os abundances and $^{187}Os/^{188}Os$ ratios with varying precision depending on the ion beam size acquired. The average total procedural blank for Os was 0.14 ± 0.04 pg (n = 3, 1SD) with a $^{187}Os/^{188}Os$ ratio of 0.194 ± 0.005. Blank corrections were applied to all analyses. The

uncertainties for $^{187}Re/^{188}Os$ and $^{187}Os/^{188}Os$ were estimated by error propagation of the blank uncertainties. Blank contributions for the measured Os concentrations and $^{187}Os/^{188}Os$ ratios of the samples were insignificant: less than 0.1% and 0.05%, respectively.

3.7.3 ICP-MS/MS

Concentrations of highly siderophile elements excluding Os were measured by ID-IS-ICP-MS/MS using iCAP TQ from Thermo Fisher Scientific (*Figure 12*, panel A) with Helium Collision and Kinetic Energy Discrimination mode (He-KED mode). For sample introduction, a combination of 100 μ/min self-aspirating nebulizer and spray chamber cooled by Peltier was used during all measurements, and oxide level (HfO^+/Hf) was set to <1%. Sample and standard solutions were interspersed throughout the analytical sessions to monitor and correct for instrumental fractionation. The monitored masses of analyses and interferences are ^{89}Y, ^{90}Zr, ^{95}Mo, ^{97}Mo, ^{99}Ru, ^{100}Ru, ^{101}Ru, ^{105}Pd, ^{106}Pd, ^{108}Pd, ^{111}Cd, ^{178}Hf, ^{185}Re, ^{187}Re, ^{191}Ir, ^{193}Ir, ^{194}Pt, ^{195}Pt, ^{196}Pt, and ^{202}Hg. Although all raw signal intensities of samples were mathematically corrected for the measured isobaric oxide interferences, contributions of interferences to analyte signals are mostly insignificant (<0.1%). The average total procedural blanks for the analyzed elements are 1.4 ± 0.1 pg for Ir, 0.44 ± 0.44 pg for Ru, 32 ± 9 pg for Pt, 6.0 ± 4.7 pg for Pd, and 3.6 ± 1.7 pg for Re (n = 3, 1SD). As in the case of Os, all analyses were blank-corrected. Blank contributions to samples for Ir, Ru, Pt, Pd, and Re were <0.5%, <0.08%, <9.4%, and <2.4%, <20%, and <44%, respectively, except for low Pd sample BVC23X-32 (15 % for Pd) and low Re samples BVC23X-3 and BVC23X-41 (68 % and 60% for Re, respectively). The uncertainties on each sample were estimated by error propagation of the analytical uncertainties during ICP-MS measurement (2SE) and blank correction. The accuracy of the analytical methods was evaluated by measuring peridotite reference materials (GP13 and JP-1), which are in good agreements with data for larger powdered samples (~1 g; (Ishikawa et al., 2014; Pearson et al., 2004)).

Figure 12: Photos from the lab at Tokyo Institute of Technology during highly siderophile elements analysis April / Mai 2024. Panel A is the ID-IS-ICP-MS/MS used for obtaining the highly siderophile elements abundances except for Os. Panel B is the N-TIMS used for Os abundances. Panel C is taken during column chemistry and panel D shows sealed quartz tubes after digestion. All photos are taken by the author.

3.7.4 Depletion ages

The Re and Os isotope concentrations measured by N-TIMS and ICP-MS/MS are used for estimating mantle depletion ages. During partial melting Os behaves compatible and remains in the solid residue while Re behaving incompatible is removed by the melt and the timing of melt extraction can be calculated based on the Re-Os radiogenic system. The ^{187}Re isotope is radioactive unstable and decays to ^{187}Os by emission of a beta particle: $^{187}Re \rightarrow {}^{187}Os + \beta^-$. The decay constant is 1.666×10^{-11}/year (Smoliar et al., 1996) and the eruption age of Bockfjorden Volcanic Complex at 1Ma is therefore negligible.

If the Re/Os ratio of samples reflects their history within the mantle, the isochron model age (T_{MA}) is calculated based on how the samples plot in the $^{187}Re/^{188}Os$ vs. $^{187}Os/^{188}Os$ diagram (*Figure 18*). A regression line for the Sverrefjellet peridotite samples trending through the primitive upper mantle (PUM) is used for estimating the age of the mantle depletion following

equation 4: $T = \frac{1}{\lambda} * \ln(slope\ of\ regression\ line)$ (equation 4), where λ is the 187Re decay constant of $1.666*10^{-11}$/year (Shirey & Walker, 1998).

Re-depletion model ages (T_{RD}) are minimum estimates for melt depletion ages (Walker et al., 1989), intersecting with chondritic mantle evolution which assumes that all Re was removed during melt-depletion ending any growth in ^{187}Os. T_{RD} were calculated based on the sample with least radiogenic Os content by equation 5 (Shirey & Walker, 1998):

$$T_{RD} = \left(\frac{1}{\lambda}\right) * \ln\left(\frac{{}^{187Os}/_{188Os_{PUM}} - {}^{187Os}/_{188Os_{sample}}}{{}^{187Re}/_{188Os_{PUM}} + 1}\right) \qquad \text{(equation 5)}$$

3.8 Integration of geoscientific data

The geophysical model for topography, depth of the lithosphere asthenosphere boundary and profile through the study area (*Figure 21*) are based on existing integrated seismic and geological data (Klitzke et al., 2015; Ritzmann et al., 2007). Ritzmann et al. (2007) provided a 3D geophysical model (BARENTS50) of the crust in the Barents Sea area, based on seismic refraction and reflection data. The seismic velocities from BARENTS50 are used for creating the model in *Figure 21*. The lithosphere-asthenosphere boundary is based on Klitzke et al. (2015). They provided an integrated 3D model of the Barents Sea and Kara Sea area with combined seismic refraction, seismic reflection and seismological in addition to existing geological maps 3D models of the area. For visualizing the extracted geophysical model of Svalbard the software "Generic Mapping Tools version 6" (Wessel et al., 2019) was used. The script is available in the appendix.

Post-fieldwork characterization of the Bockfjorden Volcanic Complex was supported by digital geological methods, notably drone-based photography. These photographs were merged into both digital outcrop models (available openly through the Svalbox database; (Betlem et al., 2023)) and photospheres (visualized via the VR Svalbard platform; www.vrsvalbard.com/map last accessed 06.12.24; (Horota et al., 2024)).

4 Results

4.1 Field observations

The abundance of mantle derived xenoliths in the Bockfjorden Volcanic Complex is high and consistent in all outcrops of lava flows, dykes, vents and volcanogenic sediments from all volcanic centers. The xenolith density varies, also within outcrops, where some localities (like *Figure 4*, panel C) have strikingly high amounts and large sizes (up to ~20 cm in diameter) of peridotite nodules. At Sverrefjellet xenoliths are also present in high quantities in the eroded material which forms a cover of scree on all sides of the mountain. Both Sverrefjellet and Halvdanpiggen hold different types of xenoliths. Spinel peridotites are by far the most common in total, although some outcrops have higher abundance of crustal xenoliths (such as the pillars close to the top of Sverrefjellet). Composite rocks of peridotite and pyroxenite are present among the xenoliths collection of Sverrefjellet (*Figure 14*, panel A and B).

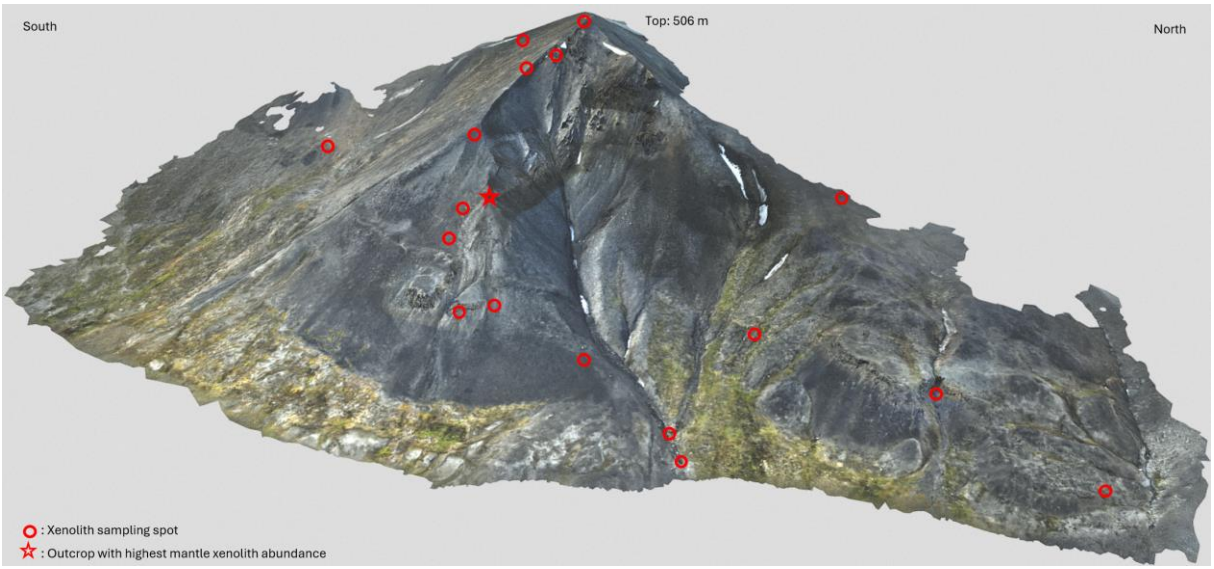

Figure 13: Digital outcrop model of Sverrefjellet with roughly located xenolith sampling spots. The mountain reaches from sea level up to 506m and xenoliths are present in the eroded material on all sides and at all outcrops. The star marks the outcrop with highest abundance of peridotite xenoliths (figure 4, panel C). The digital outcrop model can be accessed digitally via: Sverrefjellet - 3D model by svalbox (@svalbox) [0e4b556] (last accessed 06.12.24)(Betlem et al., 2023).

4.2 Petrography

All xenolith samples included in this study are mantle peridotites with mineral assemblage of olivine, orthopyroxene, clinopyroxene and spinel (confirmed by SEM analysis) with accessory sulfides. They are mostly coarse grained with granular to porphyroclastic texture and grain shapes vary from equant to more elongated and anhedral with curved linear to irregular grain

boundaries. Among the collection, five samples are composite with pyroxenitic veining. Textures and classifications for the samples included in this study are given in *Table 2*.

Figure 14: Photos of mantle xenoliths from Bockfjorden Volcanic Complex covered in host basalt. Rock A and B are both composite with pyroxenite veins (dark green). Rock C is porphyroclastic and has penetrating basaltic veins to such an extent that it was left out from geochemical analysis.

A common feature are interstadial areas and pockets of much finer grained aggregates of olivine and pyroxene (*Figure 17*, panel E). The spinel often occurs in relation to these areas and glass can be present as well. In addition, the peridotite is infiltrated by olivine rich basaltic cross cutting veins (*Figure 17*, panel F and *Figure 14*, panel C).

Porphyroclastic samples have large grains of olivine and orthopyroxene up to 1cm. These grains are strained and fractured with olivine showing distinct undulous extinction (*Figure 17*, panel B). The porphyroclasts commonly border smaller, less strained grains of olivine and pyroxene which in some areas show equilibrated textures of curve linear boundaries and 120° triple points while other areas have more irregular textures.

The peridotites show varying modal mineral assemblages that differ between the samples, but also within the same thin section (*Figure 16*). These compositional changes result in different classification, shown in *Figure15* and *Table 3*. The regular peridotites classify as lherzolites or harzburgites while five samples contain compositional variation forming veins of pyroxenite (*Figure 16*). Clinopyroxene content is especially increased in the veins bringing the classification towards olivine websterites. Veins have olivine content of 10-27%, orthopyroxene of 10-45% and clinopyroxene 35-75%. The peridotite hosting the veins has relatively high olivine and low clinopyroxene content compared to the regular samples with

olivine reaching from 50-80%, orthopyroxene 10-45% and clinopyroxene 5-9%. The regular, non-composite peridotites have olivine abundances of 45-80%, orthopyroxene 15-45% and clinopyroxene 5-15%. Spinel content varies from almost none to about 4% for the peridotites and up to 6% in the pyroxenitic veins. Scanned thin sections of all samples and their estimated modal mineral assemblages are shown in the appendix.

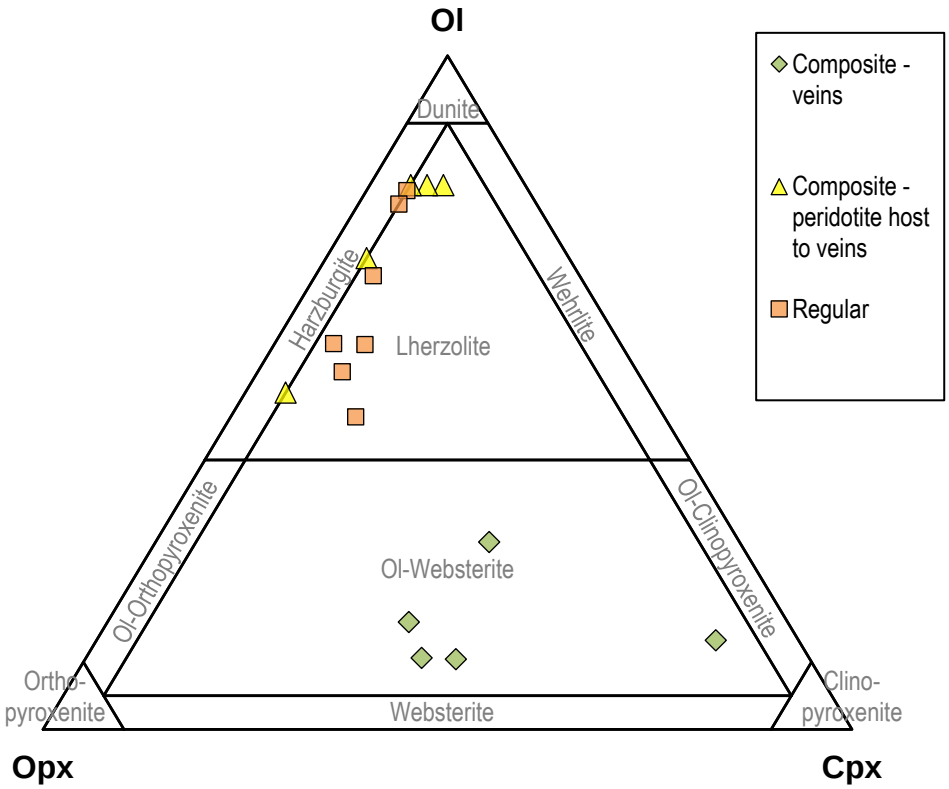

Figure 15: Ternary diagram for ultra mafic rocks following the IUGS nomenclature (Streckeisen, 1976). Plotted is a selection of representative regular peridotites covering the most to least olivine rich samples. Composite rocks are divided into veins (harzburgites and lherzolites) and host to veins (ol-websterites). The specific values are given in the table below.

Table 3: Listed values of estimated modal mineral assemblages which are plotted in the ternary diagram above.

Type	Sample	Ol (%)	Opx (%)	Cpx (%)	Spl (%)
Composite - veins	BVCX-12	15	44	35	6
	BVCX-13	27	30	40	3
	BVCX-43	13	10	75	2
	BVCX-44	10	42	44	4
	BVCX-45	10	45	39	6
Composite - peridotite host to veins	BVCX-12	49	45	5	1
	BVCX-13	70	25	4.5	0.5
	BVCX-43	80	10	9	1
	BVCX-44	80	12	7	1
	BVCX-45	80	14	5	1
Regular	BVCX-04	66	25	7	2
	BVCX-06	56	31	11	2
	BVCX-09	80	15	4.5	0.5
	BVCX-20	51	35	10	4
	BVCX-23	45	37	16	2
	BVCX-24	78	17	4.8	0.2
	BVCX-34	55	35	7	3

The pyroxene veins vary from ½ cm to several cm thickness. For sample BVC23X-12 almost the entire, fist sized rock sample was pyroxenitic (*Figure 14*, panel A). The boundaries between vein and host are sometimes distinct but can also be vague (*Figure 16*, BVC23X-43). There is no evidence of crosscutting, but rather the mineral composition clearly changes from one field to another. Another common feature for the veins is the absence of porphyroclastic olivine but rather neoblastic olivine crystals, smaller grain sized and less stained (*Figure 17*, panel D). Pyroxene on the other hand may occur as large, porphyroclastic grains. There is also a trend that the spinel abundance in the veins is higher than in their host peridotites, though only slightly higher compared to the regular peridotite samples.

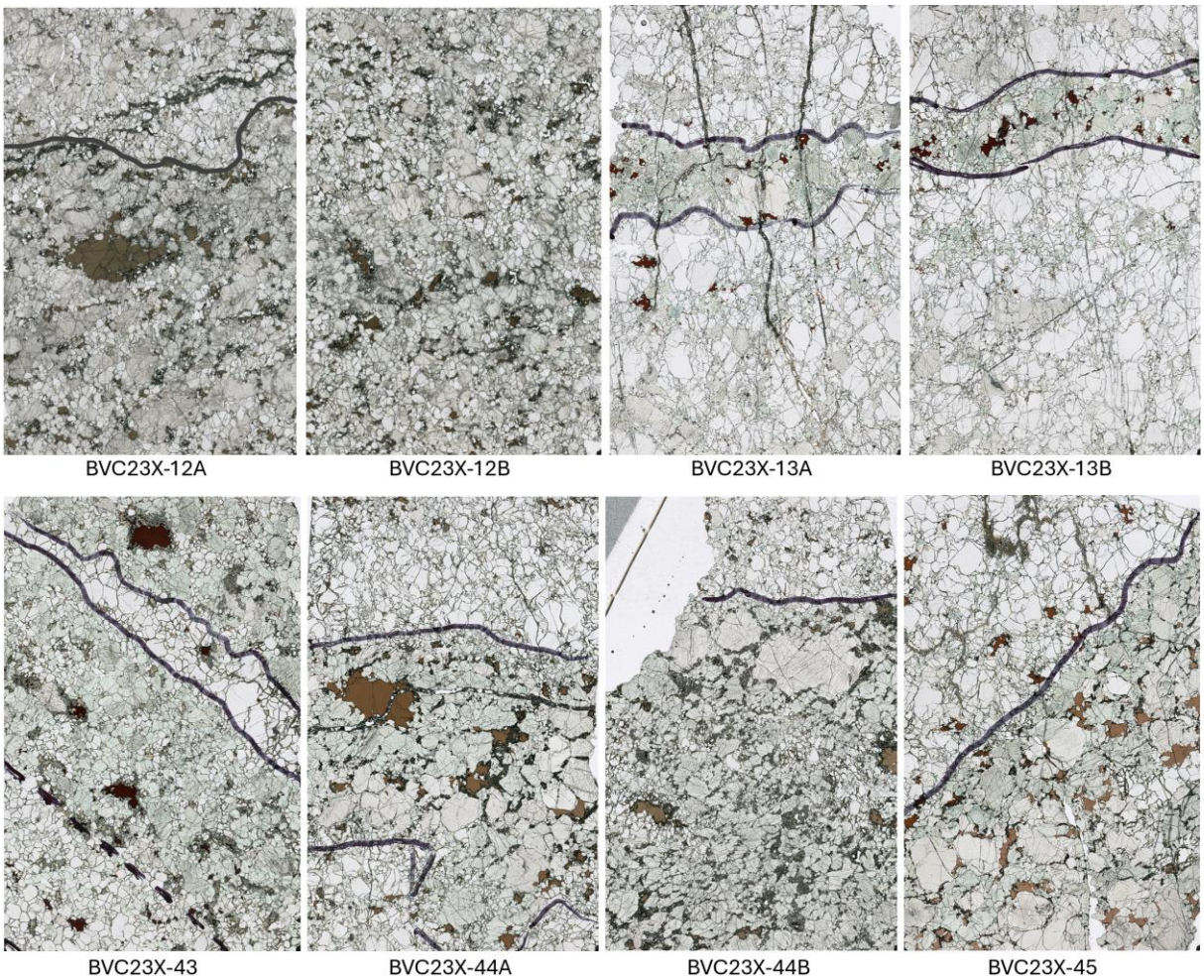

Figure 16: Scanned thin section images (~2x3cm) of the five veined peridotite samples, the drawn line marks the boundary. Olivine (white color) dominates in the host peridotite while orthopyroxene (pale yellow / brown / green) and clinopyroxene (green) dominate the pyroxene veins. Spinel is dark brown. BVC23X-12 consists mostly of pyroxenite, while BVC23X-13 has a small ½ cm thick vein running though. BVC23X-43 has several veins, though some boundaries are vague (dashed line). BVC23X-44 and 45 have porphyroclastic orthopyroxene. Appendix-xx holdes images of the rest of the samples.

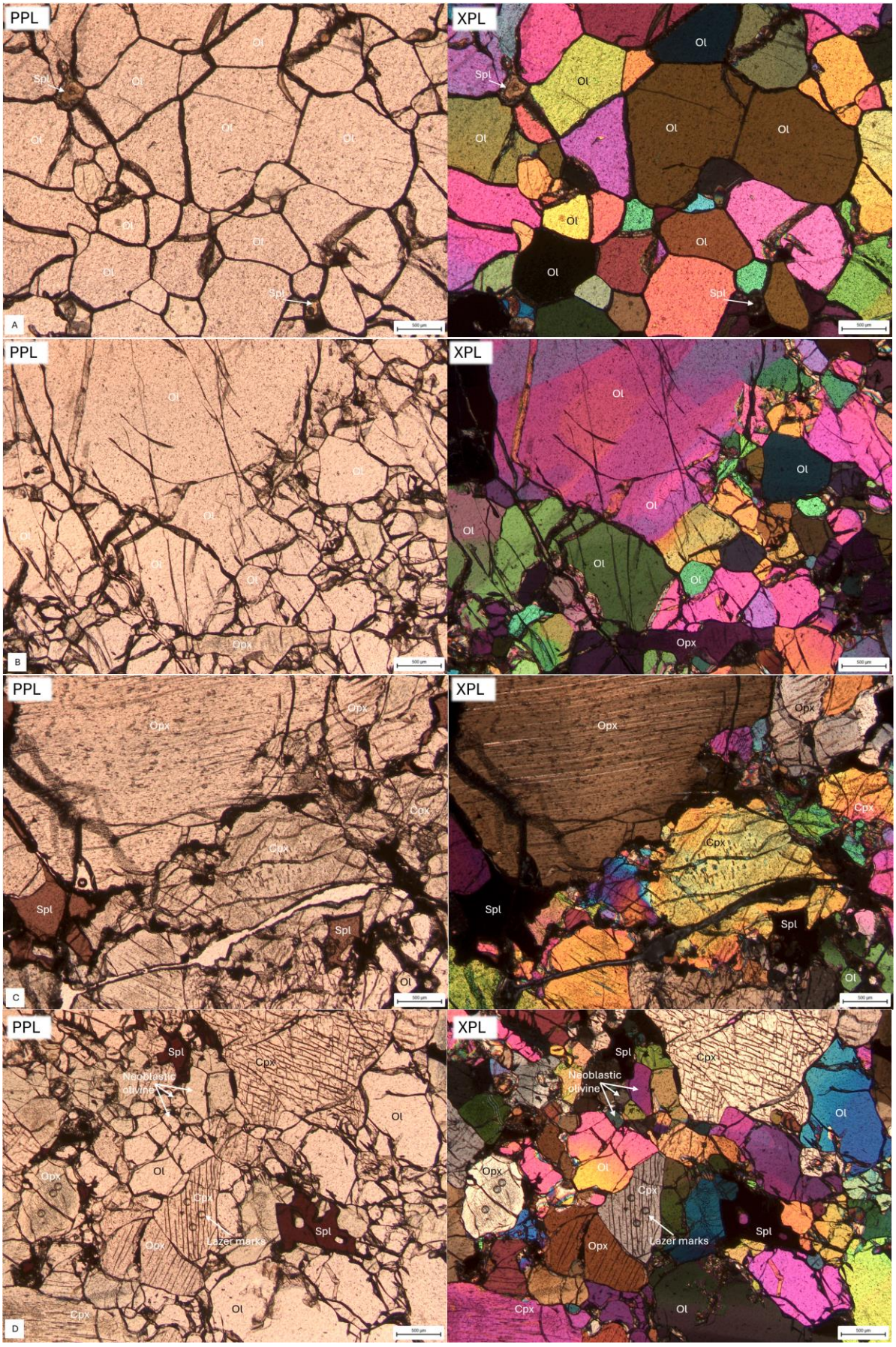
PPL
XPL
Ol
Spl
Opx
Cpx
Neoblastic olivine
Lazer marks
A
B
C
D

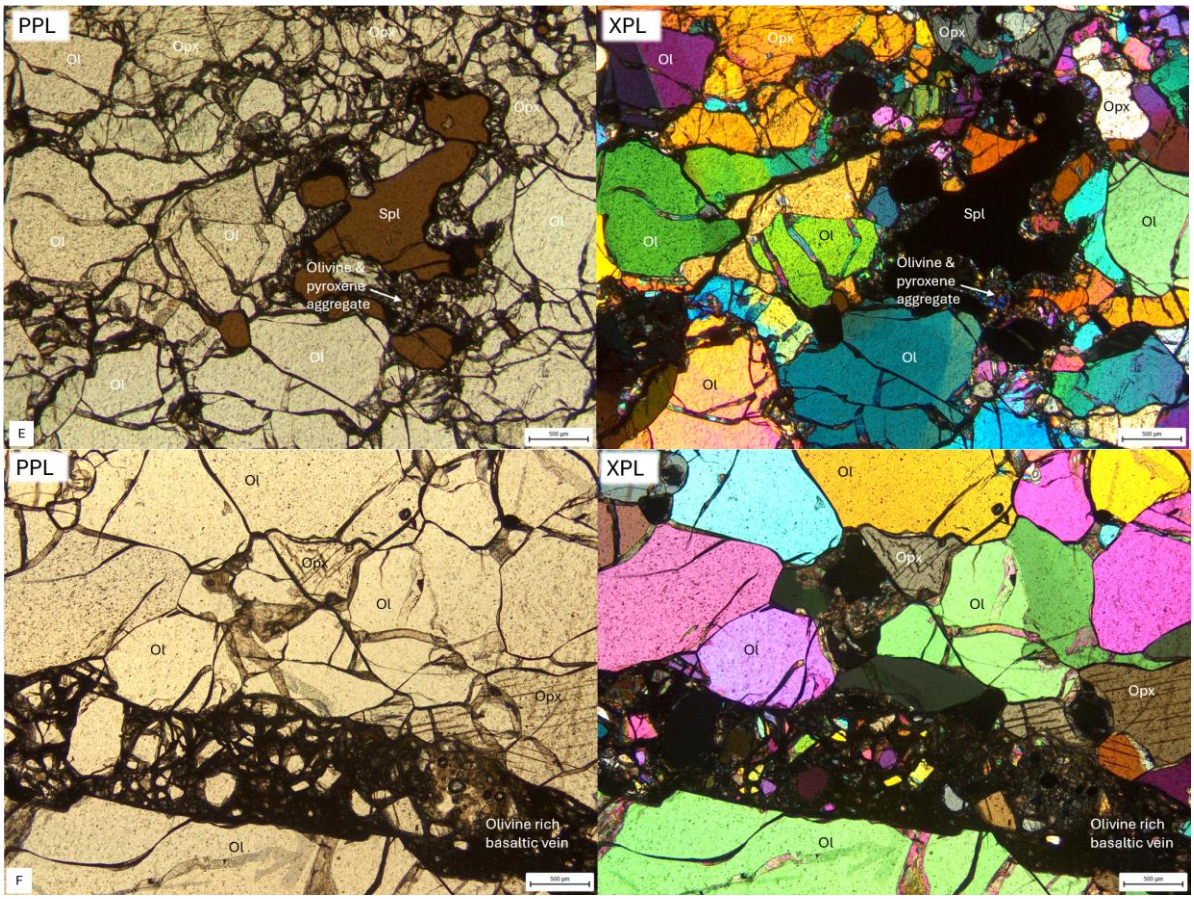

Figure 17: Microphotographs showing the variety texture, grainsize and mineral assemblage among the samples. The images are taken with a 2.5x/0.07 magnification lens in both plane polarized (PPL) and cross polarized (XPL) light and the scalebar is 500 µm. The thin sections are 50-60 µm thick, therefor the interference colors are higher than for regular thin sections. Panel A is dominated by olivine in a mosaic texture where grains are equigranular with straight to curvilinear boundaries often meeting in triple points. Grains are in equilibrium and shows no strain. Panel B is also dominated by olivine but has a large variation in grainsize where porpyroclastic olivine shows distinct undulose extinction and is fractured. Panel C shows a pyroxene dominate area within a pyroxenite vein. Orthopyroxene exists as porphyroclasts and grain boundaries are more irregular. Panel D is also from a pyroxenitic vein, though olivine is more present in between the larger pyroxene grains where some olivine are neoblasts. The circular marks on two pyroxene grains are marks after the laser ablation. Panel E shows how spinel can be related to fine grained olivine and pyroxene aggregates. The coarse mineral grains are also more irregular in shape and boundaries. Panel F has an olivine rich basaltic vein cutting through the peridotite.

4.3 Pressure and temperature estimates

The estimated pressures and temperatures for the mantle-derived xenoliths are given in the table below (*Table 4*). The major and trace element compositions for each sample from EPMA and LA-ICP-MS analysis used for the thermometry and barometry calculations are given in the appendix. Values are plotted in the temperature-depth diagram of *Figure 21*. Unfortunately, not all minerals were analyzed for every sample and therefor some are lacking PT calculations.

Table 4: Calculated temperatures, pressure and depth for selected BVC23 xenoliths. The Al-in-olivine thermometer is calculated based on Al_2O_3 from both EPMA and LA-ICP-MS but the laser data is used for the pressure estimates (P_KB). Samples types is divided into regular peridotite (R) and vein (V).

	Sample	Location	Type	T_AlOl_EPMA (°C)	T_AlOl_LAICPMS (°C)	P_KB (GPa)	depth (km)	T_BKN (°C)
EPMA Method 1	BVC23X-12A	Sverrefjellet	R	-	-	-	-	-
	BVC23X-12A	Sverrefjellet	V	1029	1028	0.33	10.9	1005
	BVC23X-13B	Sverrefjellet	V	934	878	1.28	42.1	929
	BVC23X-13B	Sverrefjellet	R	889	878	1.65	54.3	940
	BVC23X-43	Sverrefjellet	V	910	925	1.53	50.5	970
	BVC23X-43	Sverrefjellet	R	925	926	1.50	49.4	
	BVC23X-05	Sverrefjellet	R	949	913	1.35	44.5	956
	BVC23X-23	Sverrefjellet	R	925	899	1.40	46.1	969
	BVC23X-02	Sverrefjellet	R	904	876	1.13	37.3	936
	BVC23X-44A	Sverrefjellet	V	949	914	1.57	51.8	965
	BVC23X-44A	Sverrefjellet	R	925	915	1.49	49.1	952
	BVC23X-45	Sverrefjellet	V	-	839	-	-	-
	BVC23X-45	Sverrefjellet	R	928	844	-	-	-
	BVC23X-06	Sverrefjellet	R	-	-	-	-	-
EPMA Method 2	BVC23X-19	Sverrefjellet	R	921	920	1.44	47.4	994
	BVC23X-15	Sverrefjellet	R	932	922	1.40	46.2	979
	BVC23X-34	Sverrefjellet	R	946	953	1.33	43.9	1002
	BVC23X-14B	Sverrefjellet	R	948	911	1.00	33.1	960
	BVC23X-32	Halvdanpiggen	R	847	904	1.48	48.8	949
	BVC23X-39	Sigurdfjellet	R	866	889	1.45	47.8	942
	BVC23X-37	Sigurdfjellet	R	922	894	1.47	48.5	948
	BVC23X-38	Sigurdfjellet	R	1057	1065	1.25	41.1	1095
	BVC23X-09	Sverrefjellet	R	-	-	-	-	-

There is a slight difference between T_{AlOl} calculated based on EPMA and LA-ICP-MS data for the Al_2O_3 where the EPMA data generally gives higher temperatures. Because the laser ablation method is more precise the $T_{AlOl\_LAICPMS}$ values are considered the most accurate.

The calculated pressures (P_{KB}) from the Ca-in-olivine barometer (Köhler & Brey, 1990) fall in the range of 1.00 to 1.65 GPa, corresponding to depths of 33 to 54 km and most samples cluster at 1.28 to 1.57 GPa (42 to 52 km). An outlier (BVC23X-12) is calculated to crustal pressure at 0.33 GPa (10.9 km) due to a high amount of Ca in the olivine. The measurement is based on two analyses on one grain, which may not be sufficient to represent the entire xenolith. The selected olivine grain may not reflect conditions in equilibrium so that the barometry methodology is considered invalid. The analyzed grain might potentially be influenced by metasomatism increasing the Ca content and forming a second generation of olivine. The pressure for the outlying sample does not seem reasonable and is therefore excluded from the further discussion. The two samples BVC23X-14B and -02 have relative low pressure (1.00 and 1.13 GPa, respectively) compared with the cluster of datapoints. Both samples have several measurements based on a couple of grains and the low pressures seems to result from lower temperatures combined with slightly elevated Ca in olivine.

The pressure estimate is paired with two different thermometers, the alumina-in-olivine (T_{AlOl}) and two-pyroxene (T_{BKN}). For all samples except BVC23X-12, the T_{BKN} gives increased temperatures compared to T_{AlOl} with a difference of about 50 degrees. T_{AlOl} gives generally lower temperatures ranging from 839 to 1065 °C though most samples fall within 839 and 953 °C. T_{BKN} ranges from 929 to 1095 °C with most samples between 929 and 1005 °C. One outlying sample (BVC23X-38) stands out with the highest temperatures in both methods, caused by a relative high amount of Al in olivine for T_{AlOl} and Ca in orthopyroxene for the T_{BKN}. The numbers are based on many analyses of several different mineral grains and therefore should not be an artifact from poor measurements.

4.4 Highly siderophile element systematics

The whole rock abundances of Os, Ir, Ru, Pt, Pd and Re in addition to Os-Re isotope ratios obtained from N-TIMS and ICP-MS/MS are given in the table below (*Table 5*). An extended table is given in the appendix.

Table 5: Listed are measured highly siderophile elements values and isotope ratios for 35 mantle peridotite xenoliths.

Sample	Os (ng/g)	Ir (ng/g)	Ru (ng/g)	Pt (ng/g)	Pd (ng/g)	Re (ng/g)	$^{187}Re/^{188}Os$	error	$^{187}Os/^{188}Os$	error
BVC23X-01	2,33	2,06	4,13	4,25	2,28	0,07	0,153	0,009	0,118	0,00003
BVC23X-02	3,80	3,51	6,88	6,91	6,46	0,23	0,297	0,010	0,124	0,00002
BVC23X-03	0,97	1,12	2,29	1,66	0,69	0,00	0,018	0,018	0,119	0,00014
BVC23X-04	2,74	2,55	5,15	3,69	2,89	0,11	0,200	0,010	0,120	0,00002
BVC23X-05	2,51	2,26	4,62	5,37	5,39	0,28	0,533	0,031	0,137	0,00002
BVC23X-06	2,59	2,31	4,72	5,47	5,32	0,21	0,397	0,017	0,127	0,00002
BVC23X-07	2,99	2,89	6,50	4,31	3,08	0,05	0,073	0,007	0,117	0,00002
BVC23X-08	2,91	2,62	5,63	4,09	3,45	0,08	0,133	0,010	0,116	0,00003
BVC23X-09	3,34	3,24	6,24	4,07	3,17	0,01	0,014	0,006	0,113	0,00003
BVC23X-10	2,08	1,93	3,71	3,53	3,46	0,14	0,325	0,012	0,125	0,00002
BVC23X-11	2,68	2,35	5,03	3,50	2,76	0,10	0,171	0,010	0,121	0,00005
BVC23X-12	1,75	1,53	3,26	5,72	7,51	0,07	0,195	0,014	0,145	0,00001
BVC23X-13	2,28	2,27	4,40	2,78	2,47	0,07	0,143	0,009	0,119	0,00002
BVC23X-14	2,96	2,77	5,24	2,76	1,52	0,15	0,246	0,013	0,115	0,00003
BVC23X-15	2,02	2,59	4,25	1,83	0,49	0,00	0,001	0,016	0,114	0,00006
BVC23X-17	2,21	2,30	4,27	2,49	1,57	0,02	0,054	0,008	0,116	0,00004
BVC23X-19	3,34	2,58	5,30	2,57	0,52	0,01	0,016	0,005	0,113	0,00003
BVC23X-20	2,28	2,08	4,36	4,32	3,66	0,10	0,201	0,019	0,122	0,00003
BVC23X-21	2,58	2,53	4,98	3,32	2,38	0,03	0,049	0,007	0,116	0,00002
BVC23X-22	1,01	1,50	3,11	2,41	1,17	0,01	0,069	0,017	0,119	0,00007
BVC23X-23	3,35	3,08	6,20	5,50	4,75	0,14	0,201	0,010	0,125	0,00002
BVC23X-24	2,22	2,25	4,15	2,14	1,28	0,05	0,105	0,008	0,114	0,00002
BVC23X-31	1,88	2,21	4,58	2,84	1,96	0,08	0,193	0,034	0,123	0,00001
BVC23X-32	2,75	2,16	4,13	3,41	0,07	0,02	0,038	0,007	0,119	0,00003
BVC23X-33	0,70	2,50	4,81	4,42	3,03	0,02	0,169	0,027	0,126	0,00004
BVC23X-34	2,09	2,33	4,63	2,61	2,56	0,06	0,135	0,022	0,126	0,00004
BVC23X-35	0,83	2,14	4,43	4,29	2,87	0,02	0,113	0,022	0,127	0,00005
BVC23X-37	1,49	2,05	4,18	2,39	3,37	0,01	0,038	0,012	0,126	0,00007
BVC23X-38	1,20	1,83	4,23	2,61	2,23	0,01	0,048	0,014	0,120	0,00005
BVC23X-39	0,98	1,19	2,46	2,06	2,33	0,04	0,172	0,021	0,128	0,00007
BVC23X-40	1,34	1,64	3,37	1,93	2,02	0,02	0,062	0,013	0,124	0,00016
BVC23X-41	0,73	1,47	2,59	1,57	1,82	0,00	0,032	0,024	0,121	0,00005
BVC23X-43	2,37	2,11	5,35	17,10	24,90	0,17	0,345	0,016	0,137	0,00004
BVC23X-44	1,76	1,55	3,58	5,43	6,47	0,21	0,581	0,027	0,134	0,00002
BVC23X-45	1,50	1,41	2,69	3,36	3,63	0,27	0,869	0,056	0,144	0,00003

Os-Re isotope data is plotted in *Figure 18*, the data is divided into the three sampling localities and highlights the pyroxenitic samples. Peridotite samples tend to have lower ^{187}Re and radiogenic ^{187}Os than the primitive upper mantle while the samples including pyroxenitic veins have higher values. One veined sample (BVC23X-13) plots together with the regular peridotite. A likely explanation is that the pyroxenitic vein in this sample is thin and was not included into the powder that was analyzed for highly siderophile elements and therefore the result reflects the host peridotite only. On the other hand, one regular peridotite (BVC23X-05) plots above the primitive upper mantle, closely to the pyroxenitic veins. This sample has the most extensively basalt infiltration which may have contaminated the peridotite. Two of the samples with pyroxenitic veins have high $^{187}Os/^{188}Os$ but low $^{187}Re/^{188}Os$, plotting towards the upper left corner of the diagram, while the rest plots along the trend of Sverrefjellet peridotites. The samples from Halvdanpiggen and Sigurdfjellet also differs from the other peridotites by having higher radiogenic Os and plotting further to the upper right.

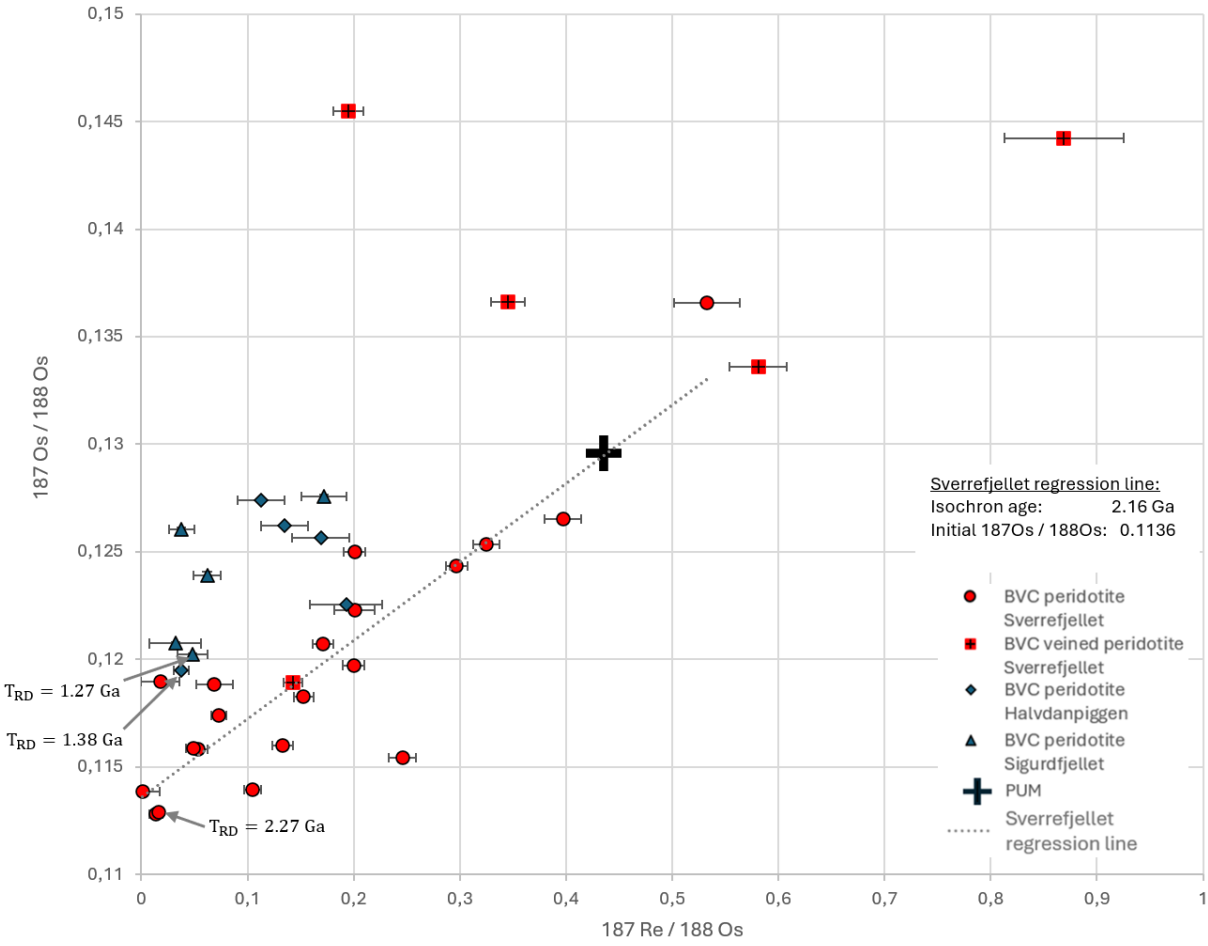

Figure 18: ^{187}Re-^{188}Os vs. ^{187}Os-^{188}Os isochron diagram for whole rock peridotites from all three sampling localities. Calculated T_{RD} model ages are linked to the sample which was used for calculations. The dashed line marks the regression line used for calculating the isochron age for Sverrefjellet.

Model ages are calculated from the least radiogenic sample of the three different sampling locations. Sverrefjellet gives a depletion age of 2.27 Ga while Halvdanpiggen and Sigurdfjellet give younger ages (1.38 and 1.27 Ga respectively). The Sverrefjellet samples trend towards the primitive upper mantle and the pyroxenitic veins, and an isochron age (2.16 Ga) is calculated based on a regression line from the Sverrefjellet peridotites and the primitive upper mantle value. The samples from Halvdanpiggen and Sigurdfjellet does not create a trend line.

Highly siderophile elements patterns show four different signatures (group 1-4) and are divided into the samples from Sverrefjellet and combined Halvdanpiggen and Sigurdfjellet (*Figure 19*). Group 1 (green color) consists of the composite veined rocks which mostly have some enrichment in the incompatible elements Pt and Pd of the palladium-group (PPGE) and Re, the most incompatible. The veined sample BVC23X-13 does not follow the trend of enrichment but is rather depleted in the incompatible elements. As discussed above, the pyroxenitic vein in this sample was likely not part of the highly siderophile elements analysis. BVC23X-05 and -06 are grouped together with the veined samples because their pattern is flat to slightly enriched in incompatible elements and are therefore behaving differently to the other regular peridotites which are depleted. Group 2 has a gentle depletion trend from compatible, Iridium-group (IPGE) to more incompatible elements and is the most common signature holding 11/35 samples. Group 3 is similar to the previous group, but the depletion has a steeper trend resulting in lower Re values. Group 4 is characterized by a decrease in Os in addition to a steep depletion in incompatible elements. Another feature regarding this group is that some of the samples have elevated Pd abundances. Samples from Sverrefjellet shows all types of highly siderophile elements signatures while Halvdanpiggen and Sigurdfjellet are dominated by group 4 though a few samples have patterns following group 2 and 3 as well.

Figure 19: Highly siderophile elements patterns of primitive upper mantle normalized values for the mantle xenoliths. The compatibility increases from left (Re and PPGE) to the right (IPGE). Group 1-4 (group 1; green, group 2; red, group 3; purple, group 4; yellow) reflects different characteristic trends and samples are presented according to which volcanic scenter they were sampled at. Sverrefjellet has the most samples, and all groups are present while Halvdanpiggen and Sigurdfjellet is dominated by group 4.

5 Discussion

5.1 What is the representative petrography and composition of mantle-derived xenoliths from Bockfjorden Volcanic Complex?

The fieldwork related to this project resulted in extensively sampling of mantle derived xenoliths from the volcanic center of Sverrefjellet, where all sides and elevations of the eroded volcano were incorporated in the sample collection. Halvdanpiggen and Sigurdfjellet have more limited sampling and may therefore not be as representative. There was no targeted sampling for any specific type of peridotite, where any suitable nodule for petrological and geochemical investigations were collected. Microscopy and SEM investigation revealed that the newly sampled xenolith selection contains only spinel bearing harzburgites, lherzolites and websterites and no garnet bearing rocks were documented. The fine-grained pockets which earlier are described as aggregates of carbonate, amphibole and silicate glass in addition to olivine, pyroxene and spinel (Ionov et al., 2002; Kim et al., 2016) were noted but not investigated in detail during this study.

The petrography of mantle-derived xenoliths from this research correlates to some degree with the earlier field observations from Bockfjorden volcanic complex (Amundsen and Choi). Choi analyzed samples from the Sverrefjellet volcano and concluded that they represent spinel bearing lherzolites and harzburgites, similar to this study. Amundsen compared the petrography of xenoliths from all three different volcanic centers. They reported spinel lherzolites and mafic granulites to be dominating at Sverrefjellet while Halvdanpiggen and Sigurdfjellet are rich in lherzolites and garnet pyroxenites. However, all types were found present at all three volcanic centers. The dominance of spinel lherzolites is supported by this study. Though, pyroxenites are spinel and not garnet bearing, in this study. In addition, this study only finds pyroxenites present at Sverrefjellet but that might be due to the limited xenolith collection from Halvdanpiggen and Sigurdfjellet.

The presence of garnet in the mantle-derived xenoliths from Bockfjorden Volcanic Complex is reported from several authors (Amundsen, Goncharov, Nikitina). From the pressure and temperature estimates the mineral assemblage correlates with plotting in the spinel stability field (*Figure 20*), though at the boundary of the transition. Therefore, it is not unlikely that some peridotite xenoliths from Bockfjorden Volcanic Complex may include garnet even though it was not observed in this study.

The findings from this study indicates that the mantle derived xenoliths from Sverrefjellet volcanic scenter is dominated by spinel bearing coarse granular to porphyroclastic lherzolites but with presence of harzburgites and olivine websterites, both spinel bearing. The presence of garnet bearing mantle xenoliths is possible. The volcanic scenters of Halvdanpiggen and Sigurdfjellet also have spinel bearing lherzolites and harzburgites of coarse granular and porphyroclastic textures.

5.2 At which depth is the lithosphere-asthenosphere boundary beneath northwestern Spitsbergen and from which depths do the xenoliths originate?

The existing petrological lithosphere-asthenosphere boundary of northwestern Spitsbergen at 60±5 km depth is based on the pressure and temperature estimates by Amundsen et al. (1987). They analyzed mostly garnet and spinel bearing websterites with thermobarometry based on garnet and orthopyroxene in addition to a few spinel lherzolites with temperatures based on olivine/orthopyroxene and spinel. Recent pressure and temperature estimates on peridotites and pyroxenites by Goncharov et al. (2015) were performed with orthopyroxene-clinopyroxene thermometer and garnet-orthopyroxene thermobarometer. They concluded that peridotites originate from 42.9-89.1 km and pyroxenites from 69.3-108.9 km depth. The estimates suggest a heat flow of 55mW/m^2, indicating a lithosphere-asthenosphere boundary at 120 km depth.

In this study both peridotites and pyroxenites were found to be spinel bearing and PT estimates were performed using new and recommended methods for such rocks, based on olivine, spinel and clinopyroxene in equilibrium. Pressure estimates for this study and Amundsen et al. (1987) are comparable (*Table 6* and *Figure 20*). Temperatures on the other hand do not correlate as well (except for BVC23X-38), where the olivine-spinel method results in ca. 100 degrees colder conditions than the samples analyzed by Amundsen et al. (1987). Estimates by Goncharov et al. (2015) have a much wider range for both pressure and temperature (*Table 6*) with samples originating from greater depths, plotting under the garnet-spinel transition (*Figure 20*).

Table 6: Comparison of estimated lithosphere-asthenosphere boundary for northwestern Spitsbergen from different studies. Garnet (grt), olivine (ol), spinel (spl), orthopyroxene (opx), clinopyroxene (cpx)

Study	Data set / samples analyzed	Methods	Pressure estimate (GPa)	Temperature estimate (°C)	LAB depth estimate (km)
This study	Spl lherzolites, harzburgites and ol websterites	Ol-spl thermometer, ol-cpx barometer	1.00-1.65	839-1065	80 ±10
Amundsen et al. (1987)	Grt websterites and one spl lherzolite	Grt-opx thermobarometer	1.19-1.49	978-1108	60 ±5
Goncharov et al. (2015)	spl lherzolites and grt pyroxenites	Opx-cpx thermometer, grt-opx themobarometer	1.3-3.3	730-1310	100
Klitske et al. (2015)	Seismic refraction, seismic reflection and seismology	Integrated geophysics	-	-	55

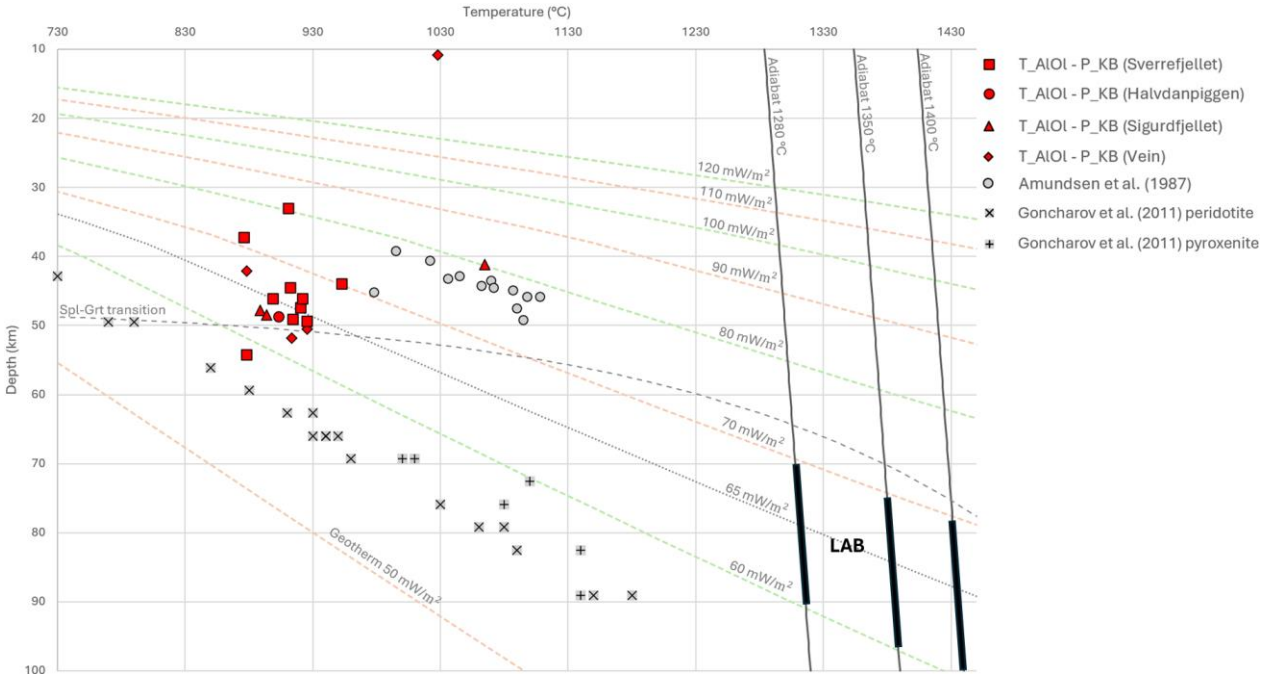

Figure 20: Temperature-depth diagram showing the pressure and temperature conditions for the mantle peridotite xenolith samples. Estimates from this study (red symbols) is compared to previous studies (grey symbols). Geothermal gradients and the spinel-garnet transition are adopted from Hasterok and Chapman (2011) and adiabats follow a 0.4 K/km temperature gradient (Katsura et al., 2010). Estimates from this study are divided into the three different sampling sites (Sverrefjellet, Halvdanpiggen and Sigurdfjellet) which do not create any distinct patterns, though the number of datapoints are limited. The peridotites including pyroxenitic veins also plot together with the regular peridotites. Except for some outliers, most of the data points cluster between the 60-70 mW/m^2 which therefore indicates lithosphere-asthenosphere boundary at 70-100 km depending on the adiabat. The lithosphere-asthenosphere boundary indicated by this study fall in between the previous estimations by Amundsen et al. (1987) and Goncharov et al. (2015).

The preferred thermobarometer of T_{AlOl} paired with P_{KB} from this study gives some spread in the P-T space and does not plot precisely along a geothermal gradient (*Figure 20*). Also, there is no systematic difference in pressure and temperature conditions from the three volcanic centers, and neither for composite veined samples. Most samples cluster around the geotherm corresponding to the surface heat flow of 65 ± 5 mW/m^2, which therefore can be used for a new suggestion for the petrological lithosphere-asthenosphere boundary. On *Figure 20*, three different adiabats typical for the upper convecting mantle are plotted: 1280 °C (which Amundsen et al. (1987) used in their estimates), 1350 °C (used by Goncharov et al. (2015)) and 1400 °C. The colder adiabat suggests a lithosphere-asthenosphere boundary at 70-90 km depth whereas the warmer adiabat suggests a maximum depth of about 100 km. This gives a deeper lithosphere-asthenosphere boundary than what Amundsen et al. (1987) suggested, but shallower than Goncharov et al. (2015). Even though the lithosphere-asthenosphere boundary estimated by this study differs from the previous, the geothermal gradient is still high and comparable to continental rift-tectonic settings (Foley et al., 2006).

The model of regional lithosphere-asthenosphere boundary depth is presented in *Figure 21*. The thickness of the lithosphere gradually increases from the spreading center at the Knipovich Ridge (~20-30 km) towards the southwest and the Barents Sea (>100 km). Most of Svalbard has a lithosphere-asthenosphere boundary at roughly 55-70 km depth and the Bockfjorden area is situated where the lithosphere-asthenosphere boundary is a its thinnest (Klitzke et al., 2015; Ritzmann et al., 2007). The estimated depth of sampled xenoliths from this study, in addition to Amundsen et al. (1987), are plotted onto the S-wave velocity cross section at the transition between Moho and the lithosphere-asthenosphere boundary (*Figure 21*).

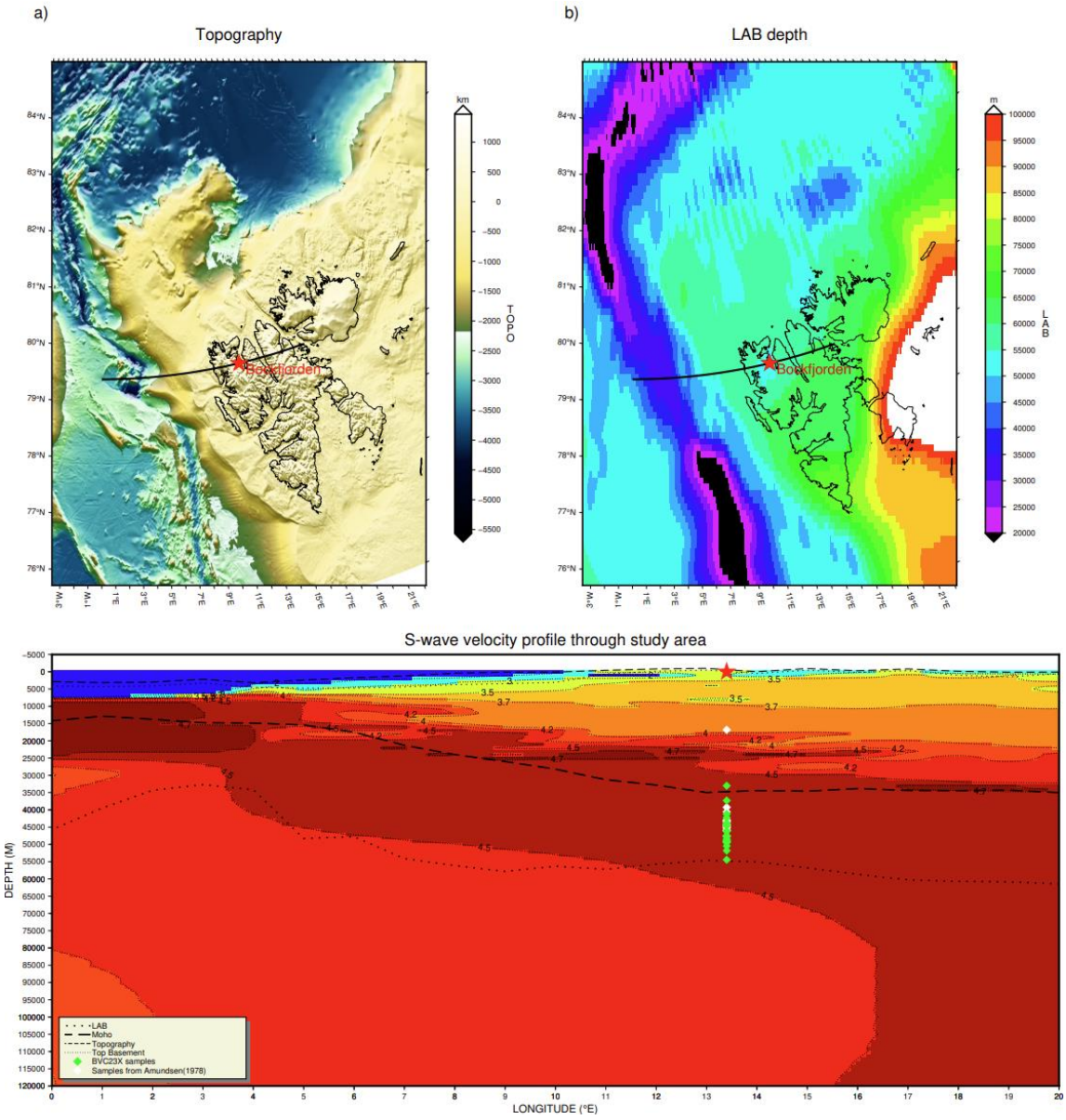

Figure 21: Regional integrated geophysical model for Svalbard highlighting the lithosphere-asthenosphere boundary depth. The study area of Bockfjorden Volcanic Complex is marked by the red star. Panel a) shows the topography of the area around Svalbard and panel b) the depth of lithosphere-asthenosphere boundary for the same area. The cross section runs through the study area and shows the increasing lithospheric thickness in addition to depth of Moho, top basement and topography. The contours separate areas based on s-wave velocities. Diamonds indicate estimated depth of sampled xenoliths from this study (green) and Amundsen et al. (1987) (white). Data from Klitzke et al. (2015); Ritzmann et al. (2007).

The regional integrated geophysical studies ((Klitzke et al., 2015); *Table 6*) indicate a lithosphere-asthenosphere boundary at 55 km depth (*Figure 21*) for northwestern Spitsbergen at present time. This should be similar to the lithosphere thickness at 1 Ma, during the time of the Bockfjorden volcanic eruptions. The geophysical-derived lithosphere-asthenosphere boundary of northwestern Spitsbergen is similar to the petrological lithosphere-asthenosphere boundary suggested by Amundsen et al. (1987) but shallower than suggested here as well as by

Goncharov et al. (2015) (*Table 6*). Compared to the geophysical data, depth estimates from both Amundsen et al. (1987) and this study indicate that the xenoliths from Bockfjorden Volcanic Complex were sampled within the rigid mantle lithosphere (*Figure 21*). While many of the samples from Goncharov et al. (2015) would suggest that the xenoliths originate from below the lithosphere-asthenosphere boundary, the convecting mantle. According to Ionov et al. (2002) the host alkali basalt, which transported the xenoliths to the surface during the volcanic eruptions, has $^{143}Nd/^{144}Nd$ values of about 0.5129. The ratio gives positive εNd values and reflects a convective mantle reservoir (DePaolo & Wasserburg, 1976) which likely is from below 80 ±10 km depth according to the petrological lithosphere-asthenosphere boundary estimated from this study.

The new geothermobarometry results of improved methodology from this study suggest comparable heatflow conditions as previous studies, though more diverse. The lithosphere-asthenosphere boundary is likely at 80 ±10 km depth with the Bockfjorden Volcanic Complex host basalt originating below. Mantle-derived xenoliths originate from the lithospheric mantle at 30-55 km depth, as presented in *Figure 22*.

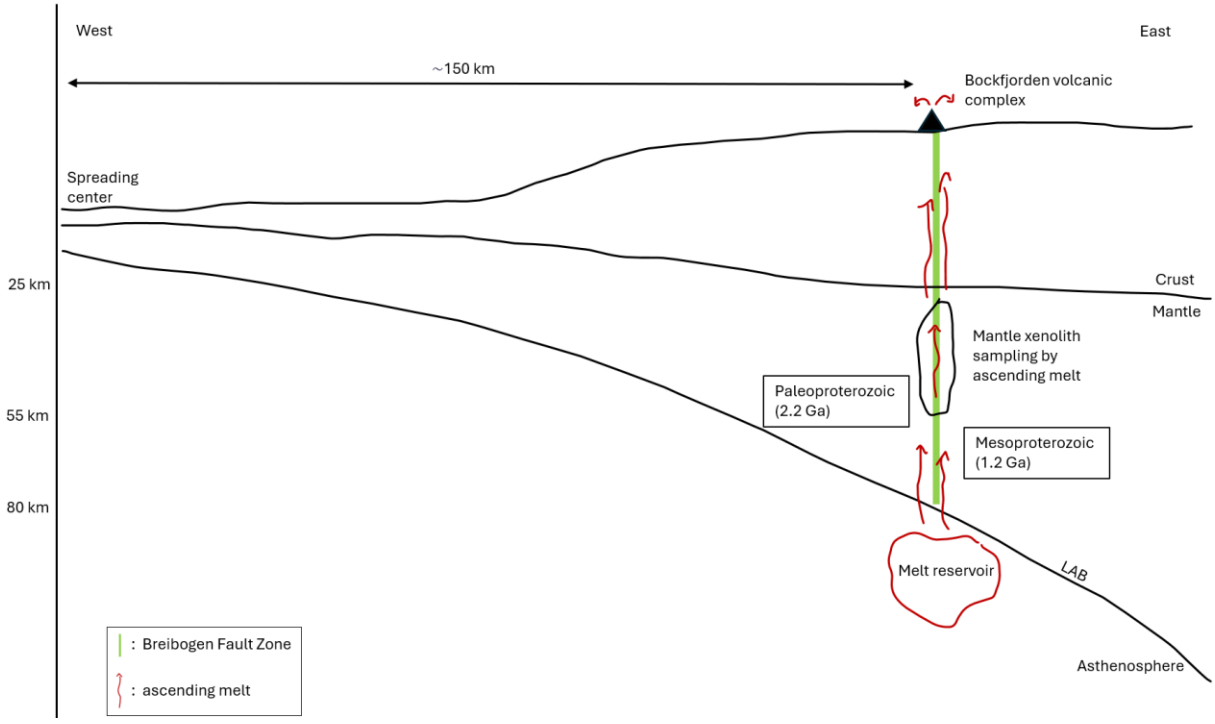

Figure 22: Cartoon of NW Spitsbergen at 1Ma during eruption of Bockfjorden volcanic complex. The alkali basaltic melt reservoir was in the asthenosphere somewhere below 80 km depth and mantle xenoliths were sampled between 55 and 30 km depth transported with the basalt to the surface. The lithosphere-asthenosphere boundary (LAB) is located at 80 km depth beneath Bockfjorden volcanic complex.

5.3 Did the pyroxene-rich veins form from passing basaltic melts, and can this hidden basaltic magmatic activity be related to any of the known igneous activity at surface?

Cross cutting harzburgitic veins and heterogeneous distribution of clinopyroxene are typical evidence for mantle refertilization (Bodinier et al., 2008; Le Roux et al., 2007). Such veins were found in xenoliths from Sverrefjellet (BVC23X-12, -13, -43, -44 & -45). There are also compositional and textural variations in the host peridotite (harzburgite to more clinopyroxene rich lherzolites and porphyroclastic to coarse granular textures). Clinopyroxene rich samples (up to 10%) exist at Halvdanpiggen and Sigurdfjellet too, but the websteritic veins are missing in these two locations. However, it is possible that this is due to limited sampling of these two localities as discussed earlier.

The highly siderophile element patterns for the regular peridotite samples show a trend of depletion with increasing incompatibility, as expected for melt depleted mantle rocks. The composite, veined samples (group 1; *Figure 19*) clearly display a different characteristic, they are enriched in incompatible elements. An exception from this trend is the most incompatible element, namely Re. Most of the veined samples are depleted in Re compared to Pt and Pd and do not follow the enrichment trend expected from a melt signature. Still, veined samples have the highest Re concentrations compared to the other peridotites and the enrichment or lack of depletion in incompatible elements likely result from a passing melt at some time.

As for the variation in the peridotite hosting the veins, there are some correlations between petrography and highly siderophile element patterns. For instance, the highly siderophile element patterns for group 2 have a gentle depletion trend and holds about 1/3 of the samples. These samples all have coarse granular textures with an olivine content of 50-60% and orthopyroxene of around 30%. Group 3 have the steepest depletion trends in the highly siderophile element patterns. Almost all samples belonging to group 3 have porphyroclastic olivine and have the highest olivine content and the least spinel content among the xenolith samples. The differences between group 2 and 3 may represent differences in the amount of depletion which results in compositional and textural variations, as there is no evidence that the clinopyroxene in regular peridotite samples results from a passing melt. As for highly siderophile element pattern group 4, the petrography of the samples is variable. They are grouped together based on the low concentrations of Os compared to Ir, which can be an effect of Os loss due to breakdown of sulfide (Handler et al., 1999). The highly siderophile elements tend to concentrate in the sulfides, but these can break down due to reactions with sulfur-

undersaturated melts during eruption or post-eruption weathering (Handler et al., 1999; Lorand, 1990; Reisberg et al., 2005). Most of the samples showing Os loss are from Halvdanpiggen and Sigurdfjellet volcanic centers where sampling was more limited, decreasing the availability of fresh samples for analysis.

Model ages for the Bockfjorden Volcanic Complex are constructed from the Re-Os isotope diagram (*Figure 18*) and indicate that there is a difference in the mantle depletion age from Sverrefjellet to Halvdanpiggen and Sigurdfjellet. All samples from Halvdanpiggen and Sigurdfjellet have higher radiogenic Os for relatively low Re compared with samples from Sverrefjellet, plotting further to the right (*Figure 18*). Because this is the case for all samples from these locations the likelihood that the shift is due to Re loss is small but instead represent a younger lithospheric mantle. No isochron age can be calculated for Halvdanpiggen and Sigurdfjellet because the samples cluster without forming any trend. Re depletion ages, on the other hand, suggest a mantle depletion age of 1.38 Ga for Halvdanpiggen and 1.27 Ga for Sigurdfjellet, 1.3 Ga in average. Sverrefjellet on the other hand gives Re depletion age of 2.27 Ga and an isochron age of 2.16, about 2.2 Ga combined. Compared to earlier isotope dating of these localities (Choi et al., 2010; Griffin et al., 2012; Kim et al., 2016) the new values correlate by giving Paleo- and Mesoproterozoic mantle depletion ages, though older Neoarchean ages are not supported by this study. Griffin et al. (2012) proposed that there are evolutional differences between west and east side of the Breibogen Fault Zone which Bockfjorden Volcanic Complex lies along, and that the two blocks were juxtaposed by transcurrent movement during the Caledonian Orogeny. Therefore, the different Re depletion ages may represent the two different blocks of lithospheric mantle separated by the Breibogen Fault Zone (*Figure 22*).

Timing for the formation of the websteritic veins can also be interpretated with the Re-Os diagram. The veined samples from Sverrefjellet mostly follow the trend line formed by the peridotites from this locality and representing the same initial $^{187}Os/^{188}Os$. Therefore, these data suggest that the formation of websteritic veins occurred temporally very close to the mantle depletion and peridotite residue formation. Such a process can be explained by refertilization directly after melt depletion, known as auto-refertilization (Rudnick & Walker, 2009), where the newly melt extracted harzburgite or dunnite gets disturbed by ascending melts formed deeper in the melt column. This process is known to produce a variety of bulk rock compositions and may therefore also explain the heterogeneity in peridotite texture and compositions from the Bockfjorden Volcanic Complex.

The pyroxene rich veins show evidence of formation though a metasomatic event by a passing melt, causing addition of highly siderophile elements. The event likely occurred directly after the initial melt depleting and peridotite formation as an auto-refertilization process in the Paleoproterozoic. Therefore, the webstericic veins are not related to any of the more recent igneous activity such as the High Arctic Large Igneous Province or the Miocene flood basalts.

5.4 How does the Svalbard lithospheric mantle compare to the North Atlantic and Arctic regions?

Os isotope concentrations for peridotites are reported from the regional North Atlantic lithospheric mantle (*Figure 23*); spinel harzburgites from the Greenlandic Archean craton (Hanghøj et al., 2001), abyssal peridotites (spinel lherzolites, plagioclase lherzolite and harzburgite) from the Gakkel Ridge (Liu et al., 2008) and the Lena Trough (Lassiter et al., 2014) in addition to the mantle xenoliths from the Bockfjorden Volcanic Complex (this study). The abyssal peridotites at both Gakkel Ridge and Lena Through show a heterogeneous mantle reservoir with melt depletion ages up to 2 Ga and 1.5 Ga, respectively. Earlier, based on basalt geochemistry, Goldstein et al. (2008) suggested that the old mantle signatures under the Gakkel Ridge originate from the Svalbard lithosphere, which was delaminated during the Caledonian Orogeny. T_{RD} model ages of sulfides from Sverrefjellet (Griffin et al., 2012) supported this theory by giving similar ages as the spreading center (Liu et al., 2008).

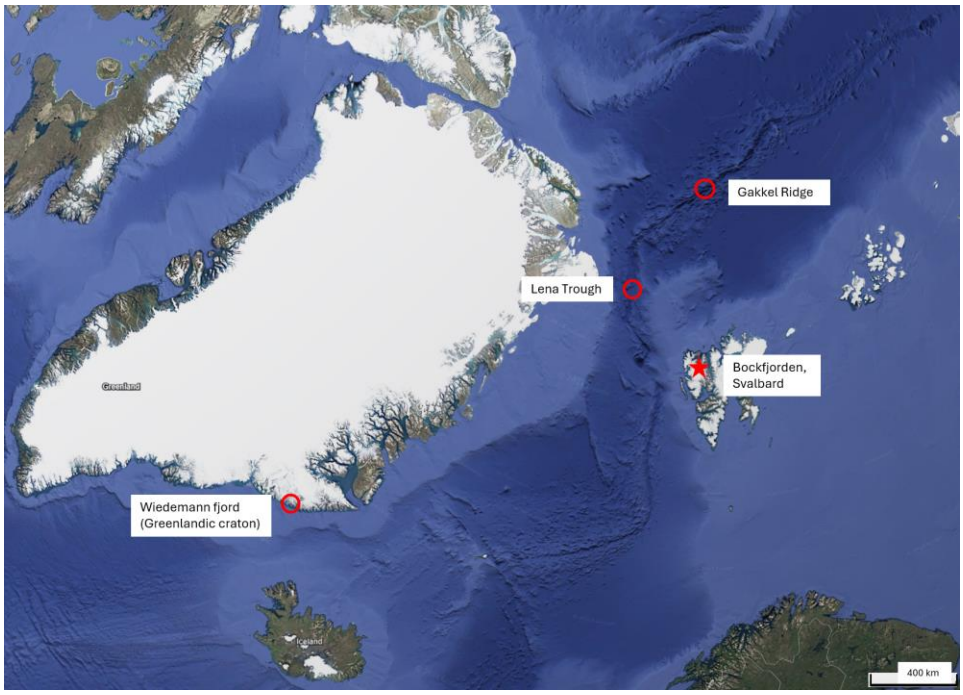

Figure 23: Map of the North Atlantic and Arctic regions. The sampling locations for the Greenlandic craton, Lena Trough and Gakkel Ridge are marked with red circles and Bockfjorden with the red star. Map from Google Earth https://earth.google.com/web/ last accessed 15.12.24.

Figure 24 compares the whole rock Os concentrations and radiogenic $^{187}Os/^{188}Os$ from the North Atlantic-Arctic region. The Greenlandic samples have both the lowest Os concentrations and radiogenic Os and stand out from the rest in the lower right corner of the diagram. The very low Os concentrations of the Greenlandic samples may be an artifact from their lab procedure where they perform ICPMS directly after digestion without any chemistry steps for concentrating the Os abundance. Still the $^{187}Os/^{188}Os$ ratio is low compared to the other peridotites in the North Atlantic and Arctic regions. The Lena Trough and Gakkel Ridge samples cluster with a $^{187}Os/^{188}Os$ ratio around 1.122-1.13 but Gakkel Ridge samples have higher Os content. The Lena Trough samples spread more where some samples have higher radiogenic Os than the primitive upper mantle, like the Bockfjorden Volcanic Complex composite peridotites, but lower total Os concentrations. The Bockfjorden Volcanic Complex peridotites also spread out on the chart, but most of the Sverrefjellet peridotites have lower radiogenic Os (0.112-0.12) than the abyssal peridotites from the two spreading scenters. On the other hand, the Halvdanpiggen and Sigurdfjellet samples have similar radiogenic Os as Lena Trough and Gakkel Ridge, though Os content tends to be lower.

Even though a few of the Svalbard peridotite xenoliths have Os concentrations overlapping with the abyssal peridotites, they generally give different signatures and therefore represent different lithospheric mantle. The Os data does not show any clear signs that the ancient lithosphere below the oceanic spreading centers originates from Svalbard.

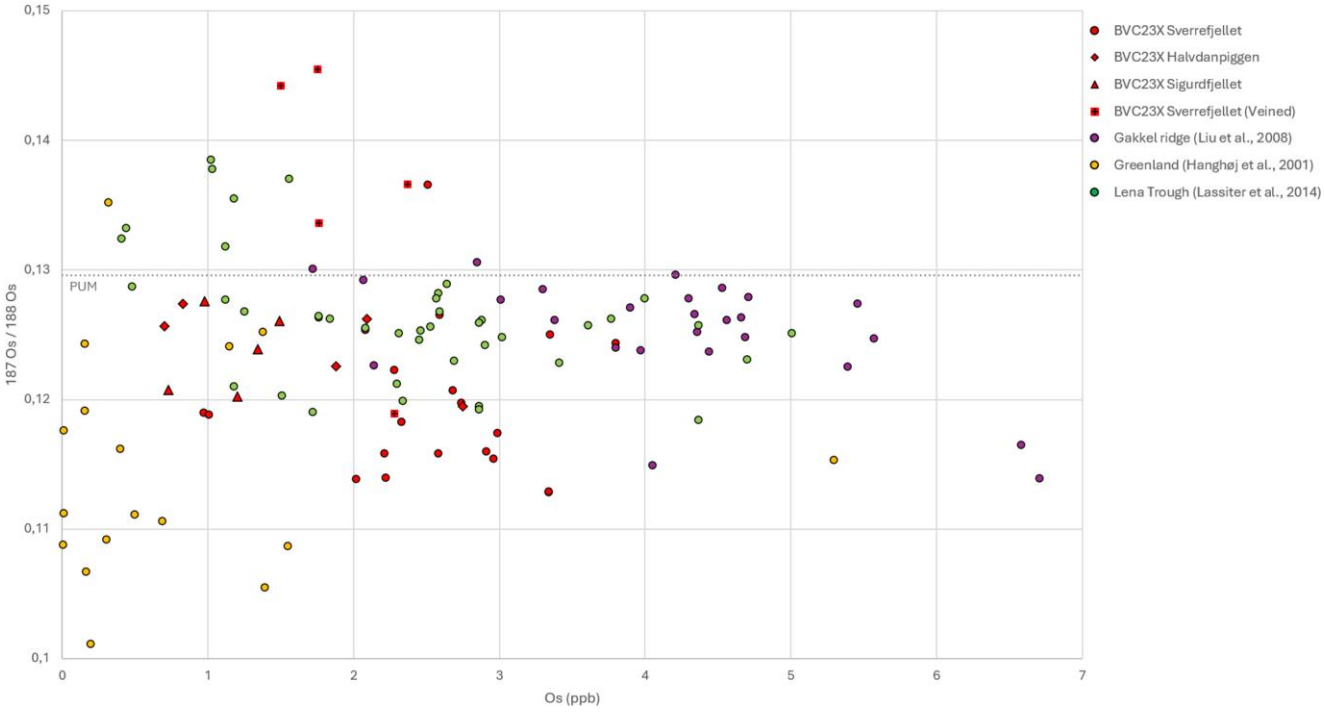

Figure 24: Total Os and radiogenic Os concentrations from the Noth Atlantic-Arctic region. There is some overlap between Svalbard peridotite xenoliths and the abyssal peridotites from Lena Trough and Gakkel Ridge, but the correlation is not clear and they seem to represent different mantle lithosphere.

5.5 Reflection on hypothesis

The working hypothesis of this thesis was that the compositional differences in the mantle-derived xenoliths represent metasomatic modifications of the mantle beneath northwestern Spitsbergen with formation of websteritic veins due to known regional magmatic activity, either the High Arctic Large Igneous Province or Miocene flood basalts. The obtained data do support that websteritic veins are an expression of metasomatic modification; though the timing of the event is likely related to the mantle melt depletion much earlier, likely during the Paleoproterozoic or Mesoproterozoic.

The estimate for the petrological lithosphere-asthenosphere boundary reveal that the lithosphere beneath northwestern Spitsbergen is thicker than suggested by regional geophysics and Amundsen et al. (1987). At the same time the lithosphere is thinner than estimated by (Goncharov et al., 2015). Though, the new data are more scattered and do not clearly follow any specific geothermal gradient, decreasing the precision. The new data show that the lithosphere beneath NW Spitsbergen is relatively thin and comparable to a continental rift tectonic setting.

6 Possible sources of error and further work

During the study there have been courses of errors and uncertainty. The first is related to the sampling of material during fieldwork in July 2023. A representative collection of samples from Sverrefjellet was achieved but the sample collection from Halvdanpiggen is more limited as the site could only be visited on two field days. The actual outcrops of Sigurdfjellet were not visited during the fieldwork, so not only is the material from there limited but there is also some degree of uncertainty about the origin of those samples. For more reliable studies on the difference between mantle xenoliths from the three volcanic centers, there is a need for a larger collection of material from Halvdanpiggen and Sigurdfjellet, the latter requiring helicopter-assisted fieldwork due to the access difficulty to the site.

Secondly, during the petrological analysis the modal mineral assemblages were obtained only by visual estimates. For more reliable estimates digital tools should be used; for example, mapping the different grains under the microscope and digitally calculate the modal percentages quantitatively.

Thirdly, the pressure and temperature calculations gave some spread in the temperature-depth plot resulting in uncertainty for the lithosphere-asthenosphere boundary estimation. One sample was clearly not representing the correct pressure, and another gave much warmer temperatures than the other samples. The source for this error can be the related to the chosen grains for EPMA and LA-ICP-MS analyses. Perhaps some grains were not in equilibrium with the neighboring mineral grains and that this was not picked up due to too few analyzed grains. For correction, more analyses are needed in order to cover a larger number of grains for each sample. In addition, smaller or medium sized grains should be analyzed, because they are more likely to have reached equilibrium during the process of diffusion that should take a shorter time than for the larger grains.

Fourthly, the interpretated timing for the creation of composite peridotites is based on the Re-Os isochron of the veined samples. Two out of five samples are deviating from the rest, leaving only three samples to define a trend. Even though about half of the composite samples match well with the regular peridotites there are too few data points for robust conclusions. Another possibility to support the interpretation is to perform an additional analysis of whole rock Al (i.e., major elements) to construct an alumina-chron where the radiogenic $^{178}Os/^{188}Os$ is plotted against Al_2O_3 concentration (Rudnick & Walker, 2009). Aluminum behaves similar to re during

melting and can therefore be used as a proxy and if the peridotites are related to the same single stage of melt depletion, the alumina-chron correlation should be linear. Similarly, performing petrological modeling, for example using MAGLAB (Massuyeau et al., 2021), of the modifying melt may give more answers regarding the metasomatic event.

Several knowledge gaps still remain in the wake of this study. Regarding the metasomatic event causing composite mantle rocks, the timing of the event may be quantified but whether the flow was channelized, creating only the websteritic veins, or if it was pervasive and perhaps the cause of clinopyroxene addition to the peridotites, is not easily answered. For examining the type of flow, detailed investigation in comparing the trace element compositions of the clinopyroxene in the pyroxenitic veins and host peridotite could help answering the question.

Finally, the major unanswered question about the Quaternary volcanism on Spitsbergen is related to the host magma origin. Although, this study has contributed to a better understanding of the lithospheric mantle conditions which the magma penetrated though, the principal reason for the rift associated volcanic eruptions on the otherwise passive continental margin is not fully understood and should be targeted by future research initiatives.

7 Conclusions

The results of this multidisciplinary thesis can be summarized as following:

- The mantle derived xenoliths from the Bockfjorden Volcanic Complex consist of spinel bearing harzburgites and lherzolites with crosscutting websteritic veins. The harzburgites have olivine contents of up to 80%, wheras the lherzolites can be pyroxene rich resulting in variable compositions. Highly siderophile element patterns also reflect compositional and textural variations among the xenoliths.
- The mantle xenoliths originate from 30-55 km depths, and new geobarometry correlates well with previous studies.
- New geothermobarometry results suggest a more diverse and on average colder conditions than earlier estimated implying heat flow conditions of 65±5 mW/m^2.
- The new petrological lithosphere-asthenosphere boundary is suggested to be at 80±10 km depth, which correlates well with the inferred origin of the host alkali basalt magma.
- New Re-Os isotope dating shows that the lithospheric mantle has a Proterozoic age. Mantle xenoliths sampled by Sverrefjellet volcano are 2.2 Ga while peridotite samples from Halvdanpiggen and Sigurdfjellet may be younger, at ca. 1.2 Ga.

- The websteritic veins present in some peridotite samples are indication of mantle metasomatism. The modifying event has a similar age as Sverrefjellet peridotites (ca. 2.2 Ga) and was likely related to the initial melt depletion event.
- Osmium concentrations show that the Svalbard mantle lithosphere is not the same as the mantle sampled below Gakkel Ridge, Lena Trough and the Greenlandic craton.

References

Amundsen, H. E. F., Griffin, W. L., & Oreilly, S. Y. (1987). The Lower Crust and Upper Mantle beneath Northwestern Spitsbergen - Evidence from Xenoliths and Geophysics. *Tectonophysics*, *139*(3-4), 169-185. https://doi.org/Doi 10.1016/0040-1951(87)90095-3

Artemieva, I. (2011). *The lithosphere: An interdisciplinary approach*. Cambridge University Press.

Ashikhmin, D., Skublov, S., Melnik, A., Sirotkin, A., & Alekseev, V. (2018). Geochemistry of Rock-Forming Minerals in Mantle Xenoliths from Basalts of Sverre Volcano, Spitsbergen Archipelago. *Geochemistry International*, *56*, 857-864.

Aulbach, S. (2012). Craton nucleation and formation of thick lithospheric roots. *Lithos*, *149*, 16-30.

Batanova, V. G., Thompson, J. M., Danyushevsky, L. V., Portnyagin, M. V., Garbe‐Schönberg, D., Hauri, E., Kimura, J. I., Chang, Q., Senda, R., & Goemann, K. (2019). New olivine reference material for in situ microanalysis. *Geostandards and Geoanalytical Research*, *43*(3), 453-473.

Bergh, S. G., Braathen, A., & Andresen, A. (1997). Interaction of basement-involved and thin-skinned tectonism in the Tertiary fold-thrust belt of central Spitsbergen, Svalbard. *AAPG bulletin*, *81*(4), 637-661.

Betlem, P., Rodés, N., Birchall, T., Dahlin, A., Smyrak-Sikora, A., & Senger, K. (2023). Svalbox Digital Model Database: A geoscientific window into the High Arctic. *Geosphere*, *19*(6), 1640-1666. https://doi.org/10.1130/ges02606.1

Birkenmajer, K. (1975). Caledonides of Svalbard and plate tectonics. *Bulletin of the Geological Society of Denmark*, *24*(1-2), 1-19.

Bodinier, J.-L., Garrido, C. J., Chanefo, I., Bruguier, O., & Gervilla, F. (2008). Origin of pyroxenite–peridotite veined mantle by refertilization reactions: evidence from the Ronda peridotite (Southern Spain). *Journal of Petrology*, *49*(5), 999-1025.

Bodinier, J.-L., & Godard, M. (2003). Orogenic, ophiolitic, and abyssal peridotites. *Treatise on geochemistry*, *2*, 568.

Borghini, G., Fumagalli, P., & Rampone, E. (2010). The stability of plagioclase in the upper mantle: subsolidus experiments on fertile and depleted lherzolite. *Journal of Petrology*, *51*(1-2), 229-254.

Bowring, S. A., & Williams, I. S. (1999). Priscoan (4.00–4.03 Ga) orthogneisses from northwestern Canada. *Contributions to Mineralogy and Petrology*, *134*(1), 3-16.

Brey, G. P., & Köhler, T. (1990). Geothermobarometry in four-phase lherzolites II. New thermobarometers, and practical assessment of existing thermobarometers. *Journal of Petrology*, *31*(6), 1353-1378.

Braathen, A., & Bergh, S. G. (1995). Kinematics of Tertiary deformation in the basement-involved fold-thrust complex, western Nordenskiøld Land, Svalbard: tectonic implications based on fault-slip data analysis. *Tectonophysics*, *249*(1-2), 1-29.

Buchan, K. L., Ernst, R., Hanski, E., Mertanen, S., Rämö, T., & Vuollo, J. (2006). Giant dyke swarms and the reconstruction of the Canadian Arctic islands, Greenland, Svalbard and Franz Josef Land. *Dyke swarms: time markers of crustal evolution*, 27-48.

Cammarano, F. (2013). A short note on the pressure‐depth conversion for geophysical interpretation. *Geophysical research letters*, *40*(18), 4834-4838.

Cawood, P. A., Hawkesworth, C., & Dhuime, B. (2013). The continental record and the generation of continental crust. *Bulletin*, *125*(1-2), 14-32.

Choi, S. H., Suzuki, K., Mukasa, S. B., Lee, J. I., & Jung, H. (2010). Lu-Hf and Re-Os systematics of peridotite xenoliths from Spitsbergen, western Svalbard: Implications for mantle-crust coupling. *Earth and Planetary Science Letters*, *297*(1-2), 121-132. https://doi.org/10.1016/j.epsl.2010.06.013

Christensen, N. I., & Mooney, W. D. (1995). Seismic velocity structure and composition of the continental crust: A global view. *Journal of Geophysical Research: Solid Earth*, *100*(B6), 9761-9788.

Cloos, M. (1993). Lithospheric buoyancy and collisional orogenesis: Subduction of oceanic plateaus, continental margins, island arcs, spreading ridges, and seamounts. *Geological Society of America Bulletin*, *105*(6), 715-737.

Coogan, L., Saunders, A., & Wilson, R. (2014). Aluminum-in-olivine thermometry of primitive basalts: Evidence of an anomalously hot mantle source for large igneous provinces. *Chemical Geology*, *368*, 1-10.

Cromwell, G., Tauxe, L., Staudigel, H., Constable, C., Koppers, A., & Pedersen, R. B. (2013). In search of long‐term hemispheric asymmetry in the geomagnetic field: Results from high northern latitudes. *Geochemistry, Geophysics, Geosystems*, *14*(8), 3234-3249.

D'Souza, R. J., Canil, D., & Coogan, L. A. (2020). Geobarometry for spinel peridotites using Ca and Al in olivine. *Contributions to Mineralogy and Petrology*, *175*(1). https://doi.org/ARTN 510.1007/s00410-019-1647-6

Dallmann, W. K. (1999). Lithostratigraphic lexicon of Svalbard: review and recommendations for nomenclature use: Upper Palaeozoic to Quaternary bedrock.

Dallmann, W. K. (2015). *Geoscience atlas of Svalbard*. Norsk Polarinstitutt.

DePaolo, D. J., & Wasserburg, G. (1976). Nd isotopic variations and petrogenetic models. *Geophysical research letters*, *3*(5), 249-252.

Dockman, D., Pearson, D., Heaman, L., Gibson, S., & Sarkar, C. (2018). Timing and origin of magmatism in the Sverdrup Basin, Northern Canada—Implications for lithospheric evolution in the High Arctic Large Igneous Province (HALIP). *Tectonophysics*, *742*, 50-65.

Dziewonski, A. M., & Anderson, D. L. (1981). Preliminary reference Earth model. *Physics of the Earth and Planetary Interiors*, *25*(4), 297-356.

Ehlers, B.-M., & Jokat, W. (2009). Subsidence and crustal roughness of ultra-slow spreading ridges in the northern North Atlantic and the Arctic Ocean. *Geophysical Journal International*, *177*(2), 451-462.

Engen, Ø., Faleide, J. I., & Dyreng, T. K. (2008). Opening of the Fram Strait gateway: A review of plate tectonic constraints. *Tectonophysics*, *450*(1-4), 51-69.

Ernst, R., & Bleeker, W. (2010). Large igneous provinces (LIPs), giant dyke swarms, and mantle plumes: significance for breakup events within Canada and adjacent regions from 2.5 Ga to the Present. *Canadian Journal of Earth Sciences*, *47*(5), 695-739.

Foley, S. F., Andronikov, A., Jacob, D. E., & Melzer, S. (2006). Evidence from Antarctic mantle peridotite xenoliths for changes in mineralogy, geochemistry and geothermal gradients beneath a developing rift. *Geochimica Et Cosmochimica Acta*, *70*(12), 3096-3120.

Fujita, R., Nakano, S., Yokoyama, T., & Ishikawa, A. (2024). Applicability of quartz tube digestion for the determination of highly siderophile and volatile chalcophile element abundances with Os isotopic compositions using ICP-MS/MS and N-TIMS. *Geochemical Journal*, *58*(1), 9-27.

Furnes, H., Pedersen, R. B., & Maaloe, S. (1986). Petrology and Geochemistry of Spinel Peridotite Nodules and Host Basalt, Vestspitsbergen. *Norsk Geologisk Tidsskrift*, *66*(1), 53-68. <Go to ISI>://WOS:A1986D309800004

Gee, D. G., Schouenborg, B., Peucat, J.-J., Abakumov, S. A., Krasil'Scikov, A., & Tebenkov, A. (1992). New evidence of basement in the Svalbard Caledonides: Early Proterozoic zircon ages from Ny Friesland granites. *Norsk Geologisk Tidsskrift*, *72*(2), 181-190.

Gee, D. G. & Hellman, F. J. 1996: Zircon Pb-evaporation agesfrom the Smutsbreen Formation, southern Ny Friesland:new evidence for Caledonian thrusting in Svalbard's East-ern Terrane. Z. Geol. Wiss. 24(3/4), 429–439.

Glebovitskii, V. A., Nikitina, L. P., Goncharov, A. G., Borovkov, N. V., & Sirotkin, A. N. (2011). Depleted and enriched matter in the upper mantle of Spitsbergen: Evidence from the study of mantle xenoliths. *Doklady Earth Sciences*, *439*(1), 1016-1020. https://doi.org/10.1134/S1028334x11060055

Goldstein, S. L., Soffer, G., Langmuir, C. H., Lehnert, K. A., Graham, D. W., & Michael, P. J. (2008). Origin of a 'Southern Hemisphere'geochemical signature in the Arctic upper mantle. *Nature*, *453*(7191), 89-93.

Goncharov, A. G., Nikitina, L. P., Borovkov, N. V., Babushkina, M. S., & Sirotkin, A. N. (2015). Thermal and redox equilibrium conditions of the upper-mantle xenoliths from the Quaternary volcanoes of NW Spitsbergen, Svalbard Archipelago. *Russian Geology and Geophysics*, *56*(11), 1578-1602. https://doi.org/10.1016/j.rgg.2015.10.006

Grégoire, M., Chevet, J., & Maaloe, S. (2010). Composite xenoliths from Spitsbergen: evidence of the circulation of MORB-related melts within the upper mantle. *Geological Society, London, Special Publications*, *337*(1), 71-86.

Griffin, W., Nikolic, N., O'Reilly, S. Y., & Pearson, N. (2012). Coupling, decoupling and metasomatism: Evolution of crust–mantle relationships beneath NW Spitsbergen. *Lithos*, *149*, 115-135.

Griffin, W., Begg, G., & O'reilly, S. Y. (2013). Continental-root control on the genesis of magmatic ore deposits. *Nature Geoscience*, *6*(11), 905-910.

Griffin, W., Graham, S., O'Reilly, S. Y., & Pearson, N. (2004). Lithosphere evolution beneath the Kaapvaal Craton: Re–Os systematics of sulfides in mantle-derived peridotites. *Chemical Geology*, *208*(1-4), 89-118.

Griffin, W., Natapov, L., O'Reilly, S. v., Van Achterbergh, E., Cherenkova, A., & Cherenkov, V. (2005). The Kharamai kimberlite field, Siberia: modification of the lithospheric mantle by the Siberian Trap event. *Lithos*, *81*(1-4), 167-187.

Griffin, W., O'Reilly, S. Y., Afonso, J. C., & Begg, G. (2009). The composition and evolution of lithospheric mantle: a re-evaluation and its tectonic implications. *Journal of Petrology*, *50*(7), 1185-1204.

Handler, M. R., Bennett, V. C., & Dreibus, G. (1999). Evidence from correlated Ir/Os and Cu/S for late-stage Os mobility in peridotite xenoliths: Implications for Re-Os systematics. *Geology*, *27*(1), 75-78.

Hanghøj, K., Kelemen, P., Bernstein, S., Blusztajn, J., & Frei, R. (2001). Osmium isotopes in the Wiedemann Fjord mantle xenoliths: a unique record of cratonic mantle formation by melt depletion in the Archaean. *Geochemistry, Geophysics, Geosystems*, *2*(1).

Harte, B. (1977). Rock nomenclature with particular relation to deformation and recrystallisation textures in olivine-bearing xenoliths. *The Journal of Geology*, *85*(3), 279-288.

Harte, B., Cox, K., & Gurney, J. (1975). Petrography and geological history of upper mantle xenoliths from the Matsoku kimberlite pipe. In *Physics and Chemistry of the Earth* (pp. 477-506). Elsevier.

Hasterok, D., & Chapman, D. (2011). Heat production and geotherms for the continental lithosphere. *Earth and Planetary Science Letters*, *307*(1-2), 59-70.

Hawkesworth, C. J., Cawood, P. A., Dhuime, B., & Kemp, T. I. (2017). Earth's continental lithosphere through time. *Annual Review of Earth and Planetary Sciences*, *45*(1), 169-198.

Hellman, F. J., Gee, D. G., & Witt-Nilsson, P. (2001). Late archean basement in the bangenhuken complex of the Nordbreen Nappe, western Ny-Friesland, Svalbard. *Polar Research*, *20*(1), 49-59.

Hirajima, T., Banno, S., Hiroi, Y., & Ohta, Y. (1988). Phase petrology of eclogites and related rocks from the Motalafjella high-pressure metamorphic complex in Spitsbergen (Arctic Ocean) and its significance. *Lithos*, *22*(2), 75-97.

Hoel, A., Holtedahl, O., (1911). Les nappes de lave, les volcans et les sources thermals dans les environs de la baie Wood au Spitsberg. Videnskapsselskapets skrifter (Christiania), Matematikk. Naturvidenskapelig klasse 8, 37 pp.

Horota, R. K., Senger, K., Smyrak-Sikora, A., Furze, M., Retelle, M., Vander Kloet, M. A., & Jonassen, M. O. (2024). VRSvalbard–a Photosphere-Based Atlas of a High Arctic Geo-Landscape. *First Break*, *42*(4), 35-42.

Ionov, D. A., Mukasa, S. B., & Bodinier, J.-L. (2002). Sr–Nd–Pb isotopic compositions of peridotite xenoliths from Spitsbergen: numerical modelling indicates Sr–Nd decoupling in the mantle by melt percolation metasomatism. *Journal of Petrology*, *43*(12), 2261-2278.

Ionov, D. A., (1998). Trace element composition of mantle-derived carbonates and coexisting phases in peridotite xenoliths from alkali basalts. *Journal of Petrology*, *39*(11-12), 1931-1941. https://doi.org/DOI 10.1093/petroj/39.11-12.1931

Ionov, D. A., Bodinier, J. L., Mukasa, S. B., & Zanetti, A. (2002). Mechanisms and sources of mantle metasomatism: Major and trace element compositions of peridotite xenoliths from Spitsbergen in the context of numerical modelling. *Journal of Petrology*, *43*(12), 2219-2259. https://doi.org/DOI 10.1093/petrology/43.12.2219

Ionov, D. A., Dupuy, C., Oreilly, S. Y., Kopylova, M. G., & Genshaft, Y. S. (1993). Carbonated Peridotite Xenoliths from Spitsbergen - Implications for Trace-Element Signature of Mantle Carbonate Metasomatism. *Earth and Planetary Science Letters*, *119*(3), 283-297. https://doi.org/Doi 10.1016/0012-821x(93)90139-Z

Ionov, D. A., OReilly, S. Y., Genshaft, Y. S., & Kopylova, M. G. (1996). Carbonate-bearing mantle peridotite xenoliths from Spitsbergen: Phase relationships, mineral compositions and trace-element residence. *Contributions to Mineralogy and Petrology*, *125*(4), 375-392. https://doi.org/DOI 10.1007/s004100050229

Irving, A. J. (1980). Petrology and geochemistry of composite ultramafic xenoliths in alkalic basalts and implications for magmatic processes within the mantle. *Amer. J. Sci.*, *280*, 389-426.

Ishikawa, A., Senda, R., Suzuki, K., Dale, C. W., & Meisel, T. (2014). Re-evaluating digestion methods for highly siderophile element and 187Os isotope analysis: Evidence from geological reference materials. *Chemical Geology*, *384*, 27-46.

Jamtveit, B., Hammer, O., Andersson, C., Dysthe, D. K., Heldmann, J., & Vogel, M. L. (2006). Travertines from the Troll thermal springs, Svalbard. *Norwegian Journal of Geology*, *86*(4), 387-395. <Go to ISI>://WOS:000244142500002

Jochum, K. P., Nohl, U., Herwig, K., Lammel, E., Stoll, B., & Hofmann, A. W. (2005). GeoReM: a new geochemical database for reference materials and isotopic standards. *Geostandards and Geoanalytical Research*, *29*(3), 333-338.

Johansson, Å., & Gee, D. G. (1999). The late Palaeoproterozoic Eskolabreen granitoids of southern Ny Friesland, Svalbard Caledonides-geochemistry, age, and origin. *Gff*, *121*(2), 113-126.

Johansson, Å., Larionov, A. N., Tebenkov, A. M., Gee, D. G., Whitehouse, M. J., & Vestin, J. (1999). Grenvillian magmatism of western and central Nordaustlandet, northeastern Svalbard. *Earth and Environmental Science Transactions of the Royal Society of Edinburgh*, *90*(3), 221-254.

Katsura, T., Yoneda, A., Yamazaki, D., Yoshino, T., & Ito, E. (2010). Adiabatic temperature profile in the mantle. *Physics of the Earth and Planetary Interiors*, *183*(1-2), 212-218.

Kearey, P., Klepeis, K. A., & Vine, F. J. (2009). *Global tectonics*. John Wiley & Sons.

Kim, N. K., Choi, S. H., & Dale, C. W. (2016). Sulfide-scale insights into platinum-group element behavior during carbonate mantle metasomatism and evolution of Spitsbergen lithospheric mantle. *Lithos*, *246*, 182-196.

Klemme, S., & O'Neill, H. S. (2000). The near-solidus transition from garnet lherzolite to spinel lherzolite. *Contributions to Mineralogy and Petrology*, *138*(3), 237-248.

Klitzke, P., Faleide, J., Scheck-Wenderoth, M., & Sippel, J. (2015). A lithosphere-scale structural model of the Barents Sea and Kara Sea region. *Solid Earth*, *6*(1), 153-172.

Koehl, J.-B., & Allaart, L. (2021). The Billefjorden Fault Zone north of Spitsbergen: a major terrane boundary? *Polar Research*, *40*.

Kopylova, M., Genshaft, Y. S., & Dashevskaya, D. (1996). Petrology of upper mantle and lower crustal xenoliths from the northwestern Spitsbergen. *Petrology*, *4*(5), 493-518.

Köhler, T., & Brey, G. (1990). Calcium exchange between olivine and clinopyroxene calibrated as a geothermobarometer for natural peridotites from 2 to 60 kb with applications. *Geochimica Et Cosmochimica Acta*, *54*(9), 2375-2388.

Lassiter, J., Byerly, B., Snow, J., & Hellebrand, E. (2014). Constraints from Os-isotope variations on the origin of Lena Trough abyssal peridotites and implications for the composition and evolution of the depleted upper mantle. *Earth and Planetary Science Letters*, *403*, 178-187.

Le Roux, V., Bodinier, J.-L., Tommasi, A., Alard, O., Dautria, J.-M., Vauchez, A., & Riches, A. (2007). The Lherz spinel lherzolite: refertilized rather than pristine mantle. *Earth and Planetary Science Letters*, *259*(3-4), 599-612.

Lee, C.-T. A., Luffi, P., & Chin, E. J. (2011). Building and destroying continental mantle. *Annual Review of Earth and Planetary Sciences*, *39*(1), 59-90.

Liu, C.-Z., Snow, J. E., Hellebrand, E., Brügmann, G., Von Der Handt, A., Büchl, A., & Hofmann, A. W. (2008). Ancient, highly heterogeneous mantle beneath Gakkel ridge, Arctic Ocean. *Nature*, *452*(7185), 311-316.

Lorand, J. (1990). Are spinel Iherzolite xenoliths representative of the abundance of sulfur in the upper mantle? *Geochimica Et Cosmochimica Acta*, *54*(5), 1487-1492.

Luck, J.-M., & Allègre, C. J. (1983). 187Re–187Os systematics in meteorites and cosmochemical consequences. *Nature*, *302*(5904), 130-132.

Maher, J., Harmon D. (2001). Manifestations of the Cretaceous High Arctic large igneous province in Svalbard. *The Journal of Geology*, *109*(1), 91-104.

Massuyeau, M., Gardes, E., Rogerie, G., Aulbach, S., Tappe, S., Le Trong, E., Sifre, D., & Gaillard, F. (2021). MAGLAB: A computing platform connecting geophysical signatures to melting processes in Earth's mantle. *Physics of the Earth and Planetary Interiors*, *314*. https://doi.org/ARTN 10663810.1016/j.pepi.2020.106638

McCann, A. J., & Dallmann, W. K. (1996). Reactivation history of the long-lived Billefjorden Fault Zone in north central Spitsbergen, Svalbard. *Geological Magazine*, *133*(1), 63-84.
McClay, Norton, M., Coney, P., & Davis, G. (1986). Collapse of the Caledonian orogen and the Old Red Sandstone. *Nature*, *323*(6084), 147-149.
McKenzie, D., & Priestley, K. (2008). The influence of lithospheric thickness variations on continental evolution. *Lithos*, *102*(1-2), 1-11.
Menzies, M. (1983). Mantle ultramafic xenoliths in alkaline magmas: evidence for mantle heterogeneity modified by magmatic activity. *Continental basalts and mantle xenoliths*, 92-110.
Menzies, M. A., & Dupuy, C. (1991). Orogenic massifs: protolith, process and provenance. *Journal of Petrology*(2), 1-16.
Minakov, A. (2018). Late Cenozoic lithosphere dynamics in Svalbard: Interplay of glaciation, seafloor spreading and mantle convection. *Journal of Geodynamics*, *122*, 1-16. https://doi.org/10.1016/j.jog.2018.09.009
Nier, A. O. (1937). The isotopic constitution of osmium. *Physical Review*, *52*(8), 885.
Nikitina, L., Marin, Y. B., Koreshkova, M. Y., Sergeev, S., Belyatsky, B., Krymsky, R. S., Bogomolov, E., Babushkina, M., & Tokusheva, A. (2022). Xenoliths of High-Alumina Pyroxenites in the Basalts of the Sigurd Volcano, Spitsbergen Island (Svalbard Archipelago), as Indicators of the Paleozoic Geodynamics of the Regional Lithosphere. *Russian Geology and Geophysics*, *63*(10), 1093-1110.
Ohta, Y., Dallmeyer, R., & Peucat, J. (1989). Caledonian terranes in Svalbard.
Ohta, Y., & Larionov, A. N. (1998). Grenvillian single-grain zircon Pb age of a granitic rock from the southern island of Hesteskoholmen, Liefdefjorden, northwestern Spitsbergen, Svalbard. *Polar Research*, *17*(2), 147-154.
Olaussen, S., Grundvåg, S.-A., Senger, K., Anell, I., Betlem, P., Birchall, T., Braathen, A., Dallmann, W., Jochmann, M., & Johannessen, E. P. (2025). Svalbard composite tectono-sedimentary element, Barents Sea. *Geological Society, London, Memoirs*, *57*(1), M57-2021-2036.
Olaussen, S., Larssen, G. B., Helland-Hansen, W., Johannessen, E. P., Nøttvedt, A., Riis, F., Rismyhr, B., Smelror, M., & Worsley, D. (2018). Mesozoic strata of Kong Karls Land, Svalbard, Norway; a link to the northern Barents Sea basins and platforms. *Norwegian Journal of Geology*, *98*(4).
Pearson, D., Irvine, G., Ionov, D., Boyd, F., & Dreibus, G. (2004). Re–Os isotope systematics and platinum group element fractionation during mantle melt extraction: a study of massif and xenolith peridotite suites. *Chemical Geology*, *208*(1-4), 29-59.
Pearson, D., & Nowell, G. (2002). The continental lithospheric mantle: characteristics and significance as a mantle reservoir. *Philosophical Transactions of the Royal Society of London. Series A: Mathematical, Physical and Engineering Sciences*, *360*(1800), 2383-2410.
Pearson, D., & Wittig, N. (2014). The formation and evolution of cratonic mantle lithosphere–evidence from mantle xenoliths.
Pearson, D. G., Scott, J. M., Liu, J., Schaeffer, A., Wang, L. H., van Hunen, J., Szilas, K., Chacko, T., & Kelemen, P. B. (2021). Deep continental roots and cratons. *Nature*, *596*(7871), 199-210.
Pettersson, C. H., Tebenkov, A., Larionov, A., Andresen, A., & Pease, V. (2009). Timing of migmatization and granite genesis in the Northwestern Terrane of Svalbard, Norway: implications for regional correlations in the Arctic Caledonides. *Journal of the Geological Society*, *166*(1), 147-158.

Piepjohn, K., von Gosen, W., & Tessensohn, F. (2016). The Eurekan deformation in the Arctic: an outline. *Journal of the Geological Society, 173*(6), 1007-1024.
Prestvik, T. (1977). Cenozoic plateau lavas of Spitsbergen-a geochemical study. *Arbok. Norsk Polarinstituitt*, 129-143.
Reimink, J., Davies, J., Chacko, T., Stern, R., Heaman, L., Sarkar, C., Schaltegger, U., Creaser, R., & Pearson, D. (2016). No evidence for Hadean continental crust within Earth's oldest evolved rock unit. *Nature Geoscience, 9*(10), 777-780.
Reisberg, L., Zhi, X., Lorand, J.-P., Wagner, C., Peng, Z., & Zimmermann, C. (2005). Re–Os and S systematics of spinel peridotite xenoliths from east central China: evidence for contrasting effects of melt percolation. *Earth and Planetary Science Letters, 239*(3-4), 286-308.
Ritzmann, O., & Jokat, W. (2003). Crustal structure of northwestern Svalbard and the adjacent Yermak Plateau: evidence for Oligocene detachment tectonics and non-volcanic breakup. *Geophysical Journal International, 152*(1), 139-159. https://doi.org/DOI 10.1046/j.1365-246X.2003.01836.x
Ritzmann, O., Jokat, W., Czuba, W., Guterch, A., Mjelde, R., & Nishimura, Y. (2004). A deep seismic transect from Hovgård Ridge to northwestern Svalbard across the continental-ocean transition: A sheared margin study. *Geophysical Journal International, 157*(2), 683-702. https://doi.org/10.1111/j.1365-246X.2004.02204.x
Ritzmann, O., Maercklin, N., Faleide, I. J., Bungum, H., Mooney, W. D., & Detweiler, S. T. (2007). A three-dimensional geophysical model of the crust in the Barents Sea region: model construction and basement characterization. *Geophysical Journal International, 170*(1), 417-435.
Rudnick, R. L., & Walker, R. J. (2009). Interpreting ages from Re–Os isotopes in peridotites. *Lithos, 112*, 1083-1095.
Saunders, J. E., Pearson, N. J., O'Reilly, S. Y., & Griffin, W. L. (2016). Gold in the mantle: the role of pyroxenites. *Lithos, 244*, 205-217.
Selway, K., Smirnov, M. Y., Beka, T., O'Donnell, J. P., Minakov, A., Senger, K., Faleide, J. I., & Kalscheuer, T. (2020). Magnetotelluric Constraints on the Temperature, Composition, Partial Melt Content, and Viscosity of the Upper Mantle Beneath Svalbard. *Geochemistry Geophysics Geosystems, 21*(5). https://doi.org/ARTN e2020GC00898510.1029/2020GC008985
Senger, K., Betlem, P., Helland-Hansen, A., Horota, R. K., Kämpf, H., Kontny, A. M., Minakov, A., Planke, S., Tappe, S., & Telmon, M. (2024). Multi-disciplinary geoscientific expedition to Woodfjorden, NW Svalbard: Field sites, methods, and preliminary results. *Czech Polar Reports, 13*(2), 142-161.
Senger, K., Tveranger, J., Ogata, K., Braathen, A., & Planke, S. (2014). Late Mesozoic magmatism in Svalbard: A review. *Earth-science reviews, 139*, 123-144.
Shirey, S. B., & Walker, R. J. (1998). The Re-Os isotope system in cosmochemistry and high-temperature geochemistry. *Annual Review of Earth and Planetary Sciences, 26*(1), 423-500.
Skjelkvale, B. L., Amundsen, H. E. F., Oreilly, S. Y., Griffin, W. L., & Gjelsvik, T. (1989). A Primitive Alkali Basaltic Stratovolcano and Associated Eruptive Centers, Northwestern Spitsbergen - Volcanology and Tectonic Significance. *Journal of Volcanology and Geothermal Research, 37*(1), 1-19. https://doi.org/Doi 10.1016/0377-0273(89)90110-8
Smelror, M., Olaussen, S., Dumais, M.-A., Grundvåg, S.-A., & Abay, T. B. (2025). Northern Svalbard composite tectono-sedimentary element. *Geological Society, London, Memoirs, 57*(1), M57-2023-2022.

Smoliar, M. I., Walker, R. J., & Morgan, J. W. (1996). Re-Os ages of group IIA, IIIA, IVA, and IVB iron meteorites. *Science*, *271*(5252), 1099-1102.
Smyrak-Sikora, A., Braathen, A., Terje Osmundsen, P., & Senger, K. (2024). Sequential reactivation of the Billefjorden Fault Zone during evolvement of the West Spitsbergen Fold and Thrust Belt, Svalbard. EGU General Assembly Conference Abstracts,
Streckeisen, A. (1976). To each plutonic rock its proper name. *Earth-science reviews*, *12*(1), 1-33.
Tappe, S., Foley, S. F., Stracke, A., Romer, R. L., Kjarsgaard, B. A., Heaman, L. M., & Joyce, N. (2007). Craton reactivation on the Labrador Sea margins: 40Ar/39Ar age and Sr–Nd–Hf–Pb isotope constraints from alkaline and carbonatite intrusives. *Earth and Planetary Science Letters*, *256*(3-4), 433-454.
Tappe, S., Massuyeau, M., Smart, K. A., Woodland, A. B., Gussone, N., Milne, S., & Stracke, A. (2021). Sheared peridotite and megacryst formation beneath the Kaapvaal craton: a snapshot of tectonomagmatic processes across the lithosphere–asthenosphere transition. *Journal of Petrology*, *62*(8), egab046.
Thurber, C., & Ritsema, J. (2007). Theory and observations-seismic tomography and inverse methods. *Seismology and the Structure of the Earth*, *1*, 323-360.
Treiman, A. H. (2012). Eruption age of the Sverrefjellet volcano, Spitsbergen island, Norway. *Polar Research*, *31*(1), 17320.
Vagnes, E., & Amundsen, H. E. F. (1993). Late Cenozoic Uplift and Volcanism on Spitsbergen - Caused by Mantle Convection. *Geology*, *21*(3), 251-254. https://doi.org/Doi 10.1130/0091-7613(1993)021<0251:Lcuavo>2.3.Co;2
Walker, R., Carlson, R., Shirey, S., & Boyd, F. (1989). Os, Sr, Nd, and Pb isotope systematics of southern African peridotite xenoliths: implications for the chemical evolution of subcontinental mantle. *Geochimica Et Cosmochimica Acta*, *53*(7), 1583-1595.
Wang, H., van Hunen, J., & Pearson, D. G. (2015). The thinning of subcontinental lithosphere: The roles of plume impact and metasomatic weakening. *Geochemistry, Geophysics, Geosystems*, *16*(4), 1156-1171.
Wessel, P., Luis, J. F., Uieda, L. a., Scharroo, R., Wobbe, F., Smith, W. H., & Tian, D. (2019). The generic mapping tools version 6. *Geochemistry, Geophysics, Geosystems*, *20*(11), 5556-5564.

Appendix

Thin section scans & modal mineral assemblage

Below are scanned images of all samples included in the study. Rough scale: 2x3 cm.

BVC-01
Coarse granular
ol: 55%
opx: 33%
cpx: 10%
spl: 2%

BVC-02
Coarse granular
ol: 50%
opx: 40%
cpx: 8%
spl: 2%

BVC-03
Type: Coarse granular with olivine and opx porphyroclasts
ol: 70%
opx: 24%
cpx: 5%
spl: 1%

BVC-04
Coarse granular
ol: 66%
opx: 25%
cpx: 7%
spl: 2%

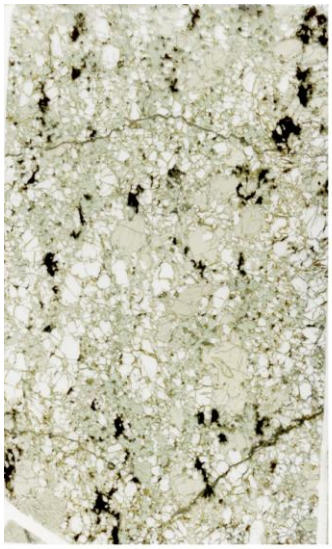

BVC-05
Type: Coarse granular
ol: 45%
opx: 40%
cpx:12%
spl: 3%

BVC-06
Type: Coarse with opx porphyroclasts
ol: 56%
opx: 31%
cpx: 11%
spl: 2%

BVC-07
Type: Coarse granular
ol: 65%
opx: 24%
cpx: 10%
spl: 1%

BVC-08
Type: Coarse granular
ol: 65%
opx: 24%
Cpx: 10%
spl: 1%

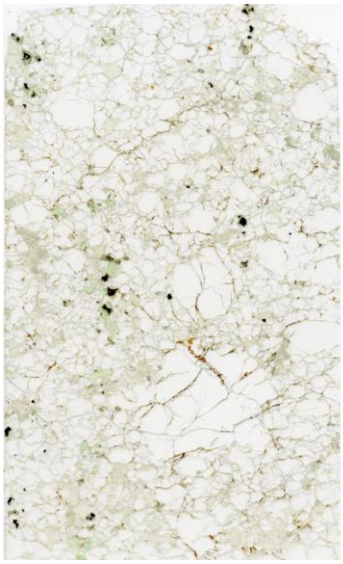

BVC-09
Type: Coarse with olivine porphyroclasts
ol: 80%
opx: 15%
cpx: 4.5%
spl: 0.5%

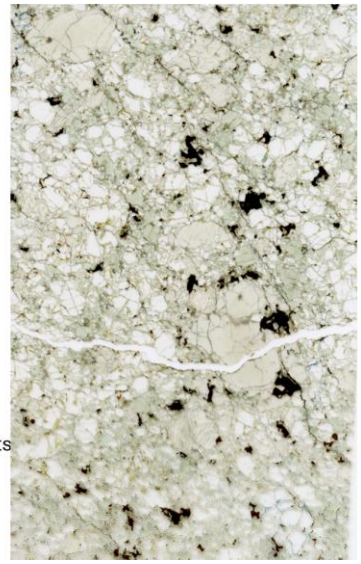

BVC-10
Type: Coarse with opx porphyroclasts
ol: 55%
opx: 35%
cpx: 10%
spl: 2%

BVC-11
Type: Coarse granular
ol: 65%
opx: 24%
cpx: 4%
spl: 2%

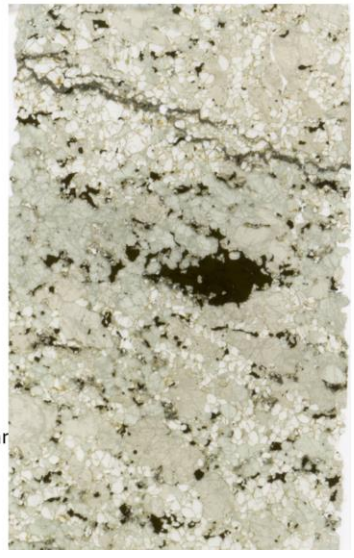

BVC-12A
Type: Composite veined

<u>Peridotite</u>
ol: 49%
opx: 45%
cpx: 5%
spl: 1%

<u>Vein</u>
ol: 15%
opx: 44%
cpx: 35%
spl: 6%

BVC-12B
Type: Composite veined

Peridotite
ol: 49%
opx: 45%
cpx: 5%
spl: 1%

Vein
ol: 15%
opx: 44%
cpx: 35%
spl: 6%

BVC-13A
Type: Composite veined

Peridotite
ol: 70%
opx: 25%
cpx: 4.5%
spl: 0.5%

Vein
ol: 27%
opx: 30%
cpx: 40%
spl: 3%

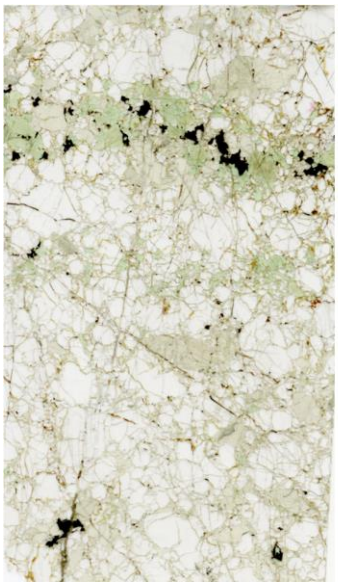

BVC-13B
Type: Composite veined

Peridotite
ol: 70%
opx: 25%
cpx: 4.5%
spl: 0.5%

Vein
ol: 27%
opx: 30%
cpx: 40%
spl: 3%

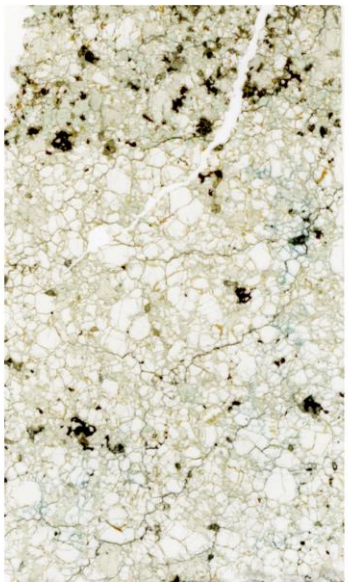

BVC-14A
Type: Coarse granular with vague veining
ol: 65%
opx: 28%
cpx: 5%
spl: 2%

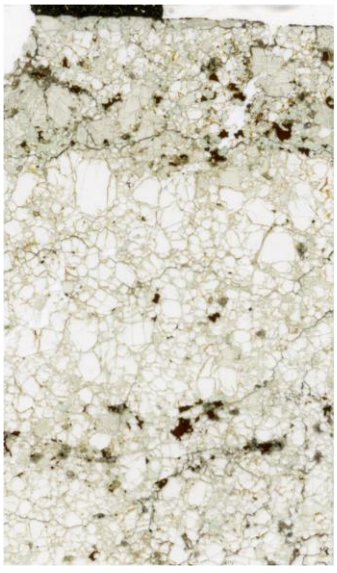

BVC-14B
Type: Coarse granular with vague veining
ol: 65%
opx: 28%
cpx: 5%
spl: 2%

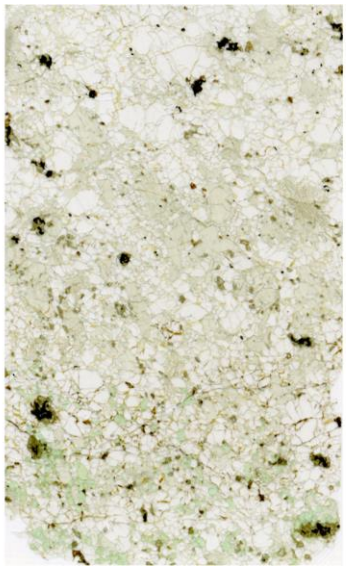

BVC-15
Type: Coarse granular with vague composite veining
ol: 50%
opx: 40%
cpx: 8%
spl: 2%

BVC-17
Type: Granular with olivine porphyroclasts
ol: 65%
opx: 25%
cpx: 18% ??
spl: 2%

BVC-19
Type: Coarse granular with olivine and opx porphyroclasts
ol: 61%
opx: 30%
cpx: 7%
spl: 2%

BVC-20
Type: Coarse granular
ol: 51%
opx: 35%
cpx: 10%
spl: 4%

BVC-21
Type: Coarse granular with olivine porphyroclasts
ol: 65%
opx: 25%
cpx: 9%
spl: 1%

BVC-22
Type: Coarse granular
ol: 55%
opx: 39%
cpx: 4%
spl: 2%

BVC-23
Type: Granular
ol: 45%
opx: 37%
cpx: 16%
spl: 2%

BVC-24
Type: Coarse granular with olivine and opx porphyroclasts
ol: 78%
opx: 17%
cpx: 4.8%
spl: 0.2%

BVC-25
Type: Coarse granular
ol: 55%
opx: 40%
cpx: 4.8%
spl: 0.2%

BVC-26
Type: Coarse granular
ol: 60%
opx: 34%
cpx: 4%
spl: 2%

BVC-27A
Type: Coarse granular
ol: 75%
opx: 19%
cpx: 4%
spl: 2%

BVC-27B
Type: Coarse granular
ol: 75%
opx: 20%
cpx: 4%
spl: 1%

BVC-28
Type: Coarse granular
ol: 55%
opx: 34%
cpx: 19%
spl: 2%

BVC-29
Type: Coarse granular
ol: 55%
opx: 35%
cpx: 9%
spl: 1%

BVC-30
Type: Coarse granular
ol: 57%
opx: 35%
cpx: 7%
spl: 1%

BVC-31
Type: Coarse granular
ol: 85%
opx: 10%
cpx: 4.8%
spl: 0.2%

BVC-32
Type: Coarse granular with olivine and opx porphyroclasts
ol: 65%
opx: 30%
cpx: 2.9%
spl: 0.1%

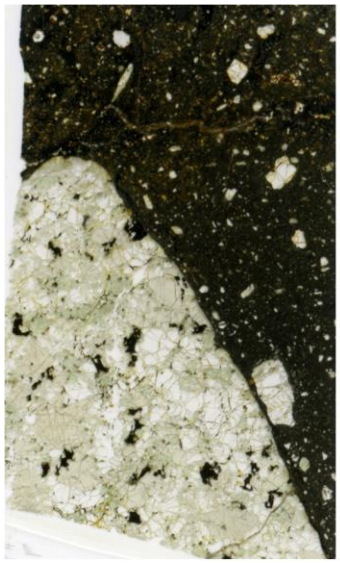

BVC-33
Type: Coarse granular
ol: 46%
opx: 42%
cpx: 10%
spl: 2%

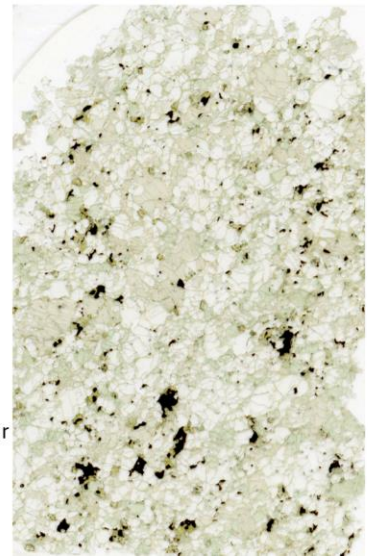

BVC-34
Type: Coarse granular
ol: 55%
opx: 35%
cpx: 7%
spl: 3%

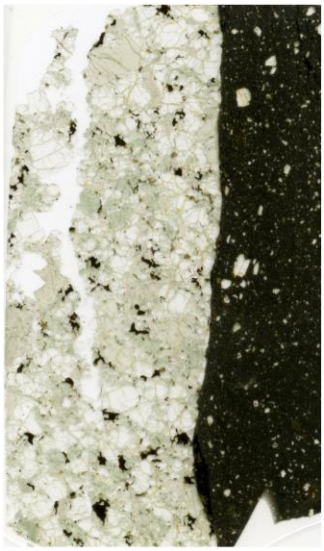

BVC-35
Type: Coarse granular
ol: 50%
opx: 40%
cpx: 8%
spl: 2%

BVC-38
Type: Coarse granular
ol: 60%
opx: 30%
cpx: 9.5%
spl: 0.5%

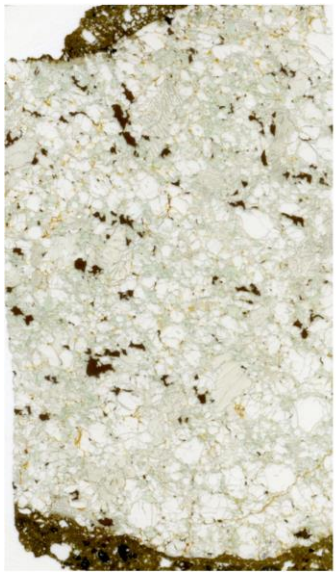

BVC-39
Type: Coarse granular
ol: 57%
opx: 31%
cpx: 10%
spl: 2%

BVC-40
Type: Coarse granular with olivine porphyroclasts
ol: 45%
opx: 38%
cpx: 15%
spl: 2%

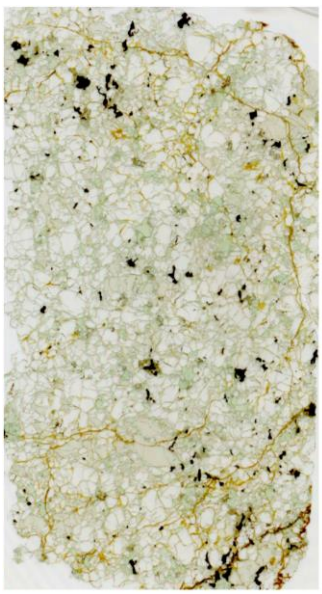

BVC-41
Type: Coarse granular
ol: 60%
opx: 30%
cpx: 8.5%
spl: 1.5%

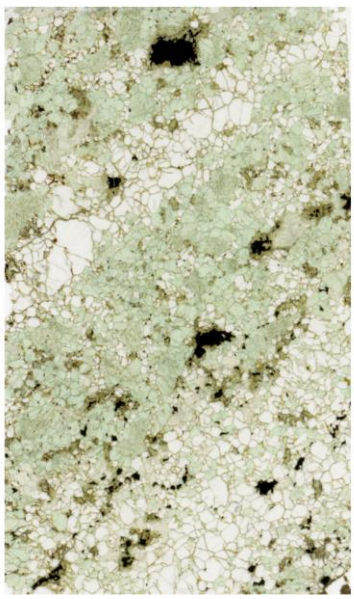

BVC-43
Type: Composite veined

Peridotite:
ol: 80%
opx: 10%
cpx:9%
spl: 1%
Vein:
ol: 13%
opx: 10%
cpx: 75%
spl: 2%

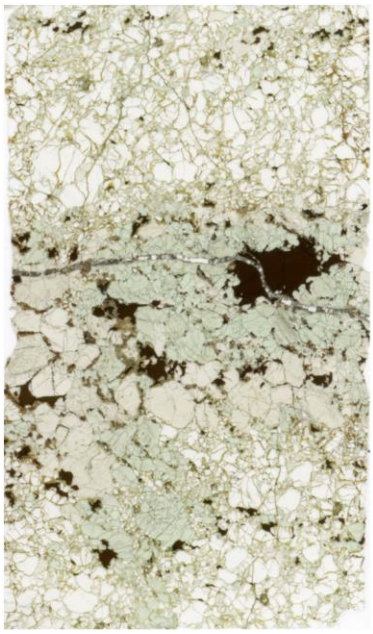

BVC-44A
Type: Composite veined

Peridotite:
ol: 80%
opx: 12%
cpx: 7%
spl: 1%
Vein:
ol: 10%
opx: 42%
cpx: 44%
spl: 4%

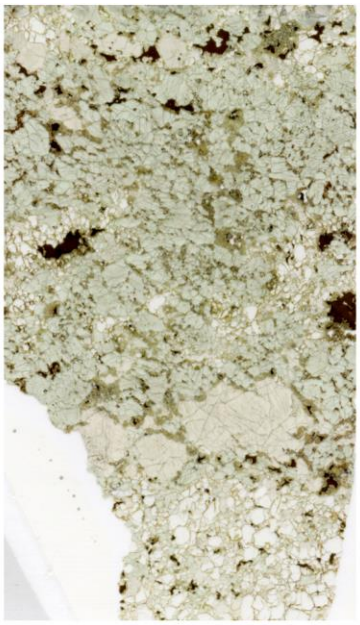

BVC-44B
Type: Composite veined

Peridotite:
ol: 80%
opx: 12%
cpx: 7%
spl: 1%
Vein:
ol: 10%
opx: 42%
cpx: 44%
spl: 4%

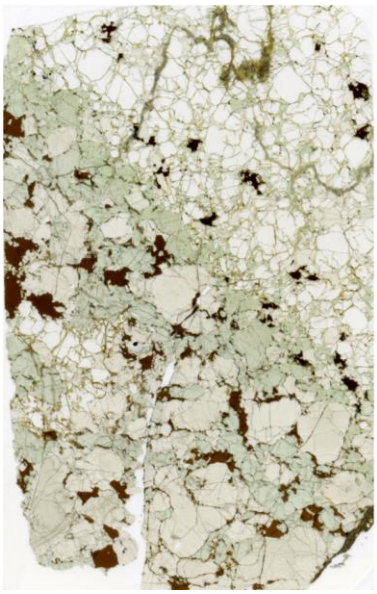

BVC-45
Type: Composite veined

Peridotite:
ol: 80%
opx: 14%
cpx: 5%
spl: 1%
Vein:
ol: 10%
opx: 45%
cpx: 39%
spl: 6%

Script

```
#!/usr/bin/env bash
#                   Topography & LAB of Svalbard + profile through Bockfjorden
gmt begin Svalbard_crossection_vs
        #creating mean surface for LAB and extracting cross section from 3D datasets
        gmt set MAP_ANNOT_OBLIQUE separate
      # gmt blockmean LAB_svalbard_new.xyz -R-44/112/62/90 -I0.5 > mean.xyz
        # gmt surface mean.xyz -I0.1 -Gdata.nc
        #Setting coordinates for cross section
        gmt project -C20/79.4 -E-0/79.4 -G1 -N > track
        gmt grdtrack track -Gbath1.nc > Topo
        gmt grdtrack track -Gdata.nc  > LAB
        gmt grdtrack track -GArcCRUST-Moho-to67.nc  > Moho
        gmt grdtrack track -GArcCRUST-SedimentThickness-to67.nc  > Sed_thickness

        #Creating contours of Vs for cross section
        gmt grdinterpolate Barents50.nc -E0/79.4/20/79.4+i.1d+g+p -T0/150/1 -Gb50slice.nc
        gmt grdedit b50slice.nc -R0/20/0/150000 -A -Gb50m.nc
        gmt grdclip -Sa4.75/4.75 -Sb1.0/1.0 b50m.nc -Gb50m_clip.nc
        gmt makecpt -Cjet -T1,2,3,3.5,3.7,4,4.2,4.5,4.7,4.8 -N
        gmt grdimage -R0/20/-5000/120000 -JX35c/-15c b50m_clip.nc
        gmt grdcontour b50m_clip.nc -A1,2,3,3.5,3.7,4,4.2,4.5,4.7,4.8 -
C1,2,3,3.5,3.7,4,4.2,4.5,4.7,4.8 -W0.5p,black,.

        #Plotting LAB, Topography, Top basement and Moho on cross section. Data
adjustments converting to km and change +/- numbers. Plotting title for graph.
        gmt plot -R0/20/-5000/120000 -JX35c/-15c LAB -W1.5p,. -Bx1 -By5000 -i0,3 -B+t"S-
wave velocity profile through study area"
        awk '{print $1, -$4}' Topo | gmt plot -W1p,-
        gmt math Topo Sed_thickness SUB = Top_basement
        awk '{print $1, -$4}' Top_basement | gmt plot -W1p,.
        gmt plot Moho -W1.5p,- -i0,3 -By+l"DEPTH (M)" -Bx+l"LONGITUDE (@~\260@~E)"
        gmt plot Cordinates_Bockfjorden.txt -Sa0.7c -Gred -i0,2
        gmt plot Xenoliths_HAM_2.txt -Sd0.3c -Gwhite -i4,3
        gmt plot Xenoliths_BVC23.txt -Sd0.3c -Ggreen -i4,3

        #plotting legend for cross section
        gmt legend -DjLB+w6.5c+o0.25c -F+p1p+gbeige+s <<- EOF
        S 0.5c - 0.9c - 1.5p,. 1c LAB
        S 0.5c - 0.9c - 1.5p,- 1c Moho
        S 0.5c - 0.9c - 0.5p,- 1c Topography
        S 0.5c - 0.9c - 0.5p,. 1c Top Basement
        S 0.5c d 0.3c green - 1c BVC23X samples
        S 0.5c d 0.3c white - 1c Samples from Amundsen(1978)
        EOF
```

```
	#Plotting 2 maps showing topography and LAB surface
	gmt subplot begin 1x2 -A+JTL -Fs16c/9c -M1 -R-100/-1600/650/-550r+uk -
Js0/90/1:5000000 -B1 -T"Svalbard Topo and LAB" -Yh+1c
		#Plotting topography of area
		gmt subplot set 0,0 -Ce3c
		gmt grd2cpt bath1.nc -Crelief -Z
		gmt grdimage bath1.nc -I+a0 -B+t"Topography"
		gmt colorbar -DJRM+o1c/0+e+mc -Bx500+lTOPO -By+lkm
		gmt pscoast -Dh -W0.75p,black
		gmt plot track -W2p,0/0/0
		gmt plot Cordinates_Bockfjorden.txt -Sa0.7c -Gred
		awk '{print $1, $2, $4}' Cordinates_Bockfjorden.txt | gmt text -D7p/0 -
F+f14p,red+jTL -N

		#Plotting dept of LAB surface in area
		gmt subplot set 0,1 -Ce3c
		gmt makecpt -Crainbow -T20000/100000/5000
		gmt grdimage data.nc -B+t"LAB depth"
		gmt colorbar -DJRM+o1c/0+e+mc -Bx5000+lLAB -By+lm
		gmt pscoast -Dh -W0.75p,black
		gmt plot track -W2p,0/0/0
		gmt plot Cordinates_Bockfjorden.txt -Sa0.7c -Gred
		awk '{print $1, $2, $4}' Cordinates_Bockfjorden.txt | gmt text -D7p/0 -
F+f14p,red+jTL -N
	gmt subplot end
gmt end show
```

Geochemical data

See the attached Excell file “Appendix-geochemical data”.